TITLE

Analysis of CDPK1 targets identifies a trafficking adaptor complex that regulates microneme exocytosis in *Toxoplasma*

AUTHORS

Alex W Chan[1,2], Malgorzata Broncel[3], Nicole Haseley[1], Sundeep Chakladar[1], Elena Andree[1], Alice L Herneisen[1,2], Emily Shortt[1], Moritz Treeck[3], Sebastian Lourido[1,2]*

[1] Whitehead Institute for Biomedical Research, Cambridge, MA, USA
[2] Biology Department, Massachusetts Institute of Technology, Cambridge, MA, USA
[3] Signaling in Apicomplexan Parasites Laboratory, The Francis Crick Institute, London, UK
* Correspondence: lourido@wi.mit.edu

ABSTRACT

Apicomplexan parasites use Ca^{2+}-regulated exocytosis to secrete essential virulence factors from specialized organelles called micronemes. Ca^{2+}-dependent protein kinases (CDPKs) are required for microneme exocytosis; however, the molecular events that regulate trafficking and fusion of micronemes with the plasma membrane remain unresolved. Here, we combine sub-minute resolution phosphoproteomics and bio-orthogonal labeling of kinase substrates in *Toxoplasma gondii* to identify 163 proteins phosphorylated in a CDPK1-dependent manner. In addition to known regulators of secretion, we identify uncharacterized targets with predicted functions across signaling, gene expression, trafficking, metabolism, and ion homeostasis. One of the CDPK1 targets is a putative HOOK activating adaptor. In other eukaryotes, HOOK homologs form the FHF complex with FTS and FHIP to activate dynein-mediated trafficking of endosomes along microtubules. We show the FHF complex is partially conserved in *T. gondii*, consisting of HOOK, an FTS homolog, and two parasite-specific proteins (TGGT1_306920 and TGGT1_316650). CDPK1 kinase activity and HOOK are required for the rapid apical trafficking of micronemes as parasites initiate motility. Moreover, parasites lacking HOOK or FTS display impaired microneme protein secretion, leading to a block in the invasion of host cells. Taken together, our work provides a comprehensive catalog of CDPK1 targets and reveals how vesicular trafficking has been tuned to support a parasitic lifestyle.

INTRODUCTION

Ca^{2+}-regulated exocytosis is ubiquitous among eukaryotes. This signaling paradigm regulates an array of processes such as neurotransmitter release in neurons, hormone secretion in endocrine cells, and histamine secretion in mast cells (Pang and Südhof, 2010). Ca^{2+}-regulated exocytosis is also critical for apicomplexan parasites that are the causative agents of rampant, life-threatening diseases including malaria, toxoplasmosis, and cryptosporidiosis (Havelaar et al., 2015). Central to their pathogenesis is their ability to transition from intracellular replicative

stages to extracellular motile stages, which involves a unique form of cellular movement called gliding, egress from the primary host cell, and invasion into a new host. These processes are driven by the Ca^{2+}-regulated exocytosis of apicomplexan-specific membrane-bound organelles called micronemes and rhoptries.

The sequential exocytosis of micronemes and rhoptries is required to promote extracellular motile stages of the parasite (Blader et al., 2016; Carruthers and Sibley, 1997). Micronemes are localized to the parasite apex and their positioning is dependent on cortical microtubules, ultrastable filaments that polymerize down the length of the parasite (Chen et al., 2015; Leung et al., 2017; Wang et al., 2021). Exocytosis of microneme cargo enables host cell rupture by releasing perforin-like proteins during egress and translocation of exposed adhesins required for gliding and attachment to new host cells (Carruthers and Sibley, 1997; Carruthers and Tomley, 2008; Kafsack et al., 2009). Multiple microneme proteins, including the associated cysteine repeat modular proteins (CRMP) complex, are also required to trigger the exocytosis of rhoptries upon host cell contact (Kessler et al., 2008; Sidik et al., n.d.; Singer et al., 2022; Sparvoli et al., 2022). Rhoptry proteins include effectors that modulate host responses and transmembrane proteins that are embedded into the host plasma membrane to enable active invasion (Bradley and Sibley, 2007; Lamarque et al., 2011, 2014; Ong et al., 2010; Tyler and Boothroyd, 2011). Intracellular Ca^{2+} release is necessary and sufficient to trigger the rapid trafficking and exocytosis of micronemes (Carruthers et al., 1999a, 1999b; Endo et al., 1982; Sidik et al., 2016b). While Ca^{2+} is also necessary for rhoptry discharge, exocytosis relies on additional cellular processes such as microneme exocytosis (Coleman et al., 2018; Segev-Zarko et al., 2022). While the exocytosis of micronemes and rhoptries is known to be critical for parasite motility, the mechanisms linking Ca^{2+} signaling to their trafficking and fusion to the plasma membrane are still unclear.

Ca^{2+} signals in apicomplexans are primarily transduced by Ca^{2+}-dependent protein kinases (CDPKs) (Billker et al., 2009; Farrell et al., 2012; Garrison et al., 2012; Kumar et al., 2017; Lourido et al., 2012, 2010; Lourido and Moreno, 2015; Luo et al., 2005; Márquez-Nogueras et al., 2021; McCoy et al., 2012; Sebastian et al., 2012). CDPKs are serine/threonine protein kinases that are unique to apicomplexans and plants. CDPKs are activated by directly binding to Ca^{2+}, in contrast to Ca^{2+}/calmodulin-dependent protein kinases (CaMKs) found in animals, which are indirectly regulated by Ca^{2+}-bound calmodulin (CaM) (Ojo et al., 2010; Wernimont et al., 2010). CDPKs are crucial for apicomplexan infection—yet are absent from mammals—making them attractive drug targets; however, their mechanisms of action are still not well understood at a cellular and molecular level. In *T. gondii*, Ca^{2+}-dependent protein kinase 1 (CDPK1) is required for the Ca^{2+}-regulated exocytosis of micronemes, impacting all steps of parasite motility including egress, gliding, and invasion (Lourido et al., 2010). Small-molecule competitive inhibitors against CDPK1 have been identified and have shown some activity against *T. gondii* (Doggett et al., 2014; Johnson et al., 2012; Lourido et al., 2013b, 2010; Winzer et al., 2015). Identifying the signaling pathways regulated by CDPK1 could reveal the pathways controlling microneme and rhoptry exocytosis.

The Ca^{2+} that activates CDPK1 and other cellular processes is released from intracellular stores following cyclic nucleotide–mediated activation of protein kinase G (PKG) (Bisio and Soldati-Favre, 2019; Brown et al., 2017; Sidik et al., 2016a). This process can be artificially induced by treating parasites with cGMP specific phosphodiesterase (PDE) inhibitors zaprinast or BIPPO that indirectly activate PKG (**Figure 1A**)(Lourido et al., 2012; Nofal et al., 2022; Sidik et al., 2016a; Yuasa et al., 2005). PDE inhibition activates PKG within seconds and triggers the Ca^{2+} and lipid signaling nodes controlling parasite motility, including the exocytosis of micronemes (**Figure 1A**)(Lourido et al., 2012; Yuasa et al., 2005). The identity of the CDPK1 substrates that contribute to the regulation of microneme exocytosis remains unknown. Determining CDPK1-dependent phosphorylation is challenging because the signaling pathways controlling parasite motility are rapid and integrate signals from multiple kinases.

Global phosphoproteomic studies found that Ca^{2+}-dependent phosphorylation included proteins involved in signal transduction, motility, exocytosis, cytoskeleton, in addition to many proteins with unknown functions; however, the functional relevance and organization of these proteins—especially CDPK1—in regulating exocytosis remain unclear (Herneisen et al., 2022; Invergo et al., 2017; McCoy et al., 2012; Nofal et al., 2022; Treeck et al., 2014, 2011). Here, we utilized time-resolved phosphoproteomics and chemical genetics to identify 163 proteins phosphorylated by CDPK1. Our comprehensive analysis of CDPK1 not only identified phosphoregulation of known factors involved in parasite motility, but also revealed new regulators of exocytosis. We identified a conserved HOOK complex that is phosphorylated by CDPK1 and is required for microneme exocytosis by mediating the rapid trafficking of micronemes during parasite motility.

RESULTS

Identifying CDPK1-dependent phosphorylation with sub-minute resolution

We examined the effect of CDPK1 on the phosphoproteome. To control the expression of CDPK1, we endogenously tagged the kinase with a C-terminal auxin-inducible degron (AID) for rapid conditional knockdown upon treating parasites with auxin (**Figure 1A**)(Brown et al., 2018; Shortt et al., 2022; Smith et al., 2022). CDPK1 was robustly depleted from extracellular parasites following auxin treatment for 3.5 hrs (**Figure 1B**). We compared vehicle- and auxin-treated parasites at four timepoints in the 5 min following zaprinast stimulation (0, 9, 30, and 300 s) to capture the earliest changes following Ca^{2+} flux (**Figure 1C**). We used TMTpro labeling to multiplex 16 samples enabling analysis of a complete time course comparing vehicle- and auxin-treated parasites in biological duplicate in a single LC-MS/MS experiment (Li et al., 2020). Samples treated with DMSO instead of zaprinast served as a control. We enriched for phosphopeptides using sequential metal-oxide affinity chromatography (SMOAC) (Tsai et al., 2014). In total, we generated four datasets: an enriched zaprinast phosphoproteome [1], a zaprinast proteome (unenriched) [2], an enriched DMSO phosphoproteome [3], and a DMSO proteome (unenriched) [4]. Of the 4,255 parasite proteins quantified in the zaprinast proteome by LC-MS/MS, CDPK1 was the only protein with a greater than two-fold depletion in parasites

121 treated with auxin (**Figure 1D**). The remainder of the proteome was largely stable (median log_2-
122 fold change = -0.002 ± 0.089 M.A.D).
123
124 We first quantified peptide abundances across time relative to the 0 sec vehicle-treated time
125 point to identify CDPK1-dependent phosphorylation, which yielded kinetic profiles of individual
126 phosphopeptides in vehicle and auxin conditions (**Figure 1C**). The zaprinast phosphoproteome
127 included 2,570 phosphorylated proteins, represented by 10,594 unique phosphopeptides
128 quantified across both biological replicates (**Figure 1E**). We calculated the area under the curve
129 (AUC) of individual phosphopeptide profiles for vehicle ($AUC_{vehicle}$) and auxin (AUC_{auxin}) conditions.
130 To identify the subset of phosphopeptides exhibiting CDPK1-dependent phosphorylation, we
131 calculated the difference between AUC values ($AUC_{difference}$) by comparing the distribution of
132 $AUC_{difference}$ values in the zaprinast phosphoproteome to a null distribution derived from the
133 DMSO phosphoproteome (**Figure 1—figure supplement 1**). This approach allowed us to
134 account for the variability among AUCs under conditions that did not exhibit dynamic changes.
135 We identified 74 unique CDPK1-dependent phosphopeptides across both biological replicates
136 (Group A), belonging to 69 proteins (**Figure 1E–F**). Additionally, we identified peptides that were
137 zaprinast responsive—despite being CDPK1 independent—by comparing the distribution of
138 $AUC_{vehicle}$ values in the zaprinast phosphoproteome to a null distribution derived from the DMSO
139 phosphoproteome, resulting in 809 unique phosphopeptides representing 501 proteins. We
140 utilized projection-based clustering to sort kinetic profiles of CDPK1-independent peptides into
141 three groups, in which Group B and Group C contained phosphopeptides that increased in
142 abundance and Group D contained phosphopeptides that decreased in abundance (Thrun and
143 Ultsch, 2021)(**Figure 1G**, **Figure 1—figure supplement 1**) (Thrun and Ultsch, 2021). Significant
144 changes at the peptide level are attributed to altering levels of phosphorylation as opposed to
145 protein levels. Of the 543 proteins exhibiting zaprinast-dependent phosphorylation, 484 were
146 quantified at the proteome level. When comparing the 300 to 0 sec time points, zaprinast-
147 dependent proteins displayed no significant changes (median log_2-fold change = 0 ± 0.074
148 M.A.D). This was consistent with the rapid time scale of these experiments and the overall
149 stability of the 4,255 proteins quantified in the proteome (median log_2-fold change = 0.01 ± 0.089
150 M.A.D).
151
152 Gene ontology analysis identified several classes of genes that may be relevant to the regulation
153 of zaprinast responses within the different groups (**Figure 1H**). CDPK1-independent
154 phosphorylation and dephosphorylation was prevalent amongst proteins regulating cyclic
155 nucleotide signaling (ACβ, GC, UGO, PDE1, PDE2, PDE7, PDE9, PDE10, and PKG), lipid
156 signaling (PI4K, PI4P5K, PI-PLC, DGK1, and PAP1), and Ca^{2+} signaling (CDPK2A and CDPK3).
157 CDPK1-independent phosphorylation was also observed on downstream proteins regulating
158 microneme exocytosis (APH and DOC2.1), rhoptry exocytosis (ARO, AIP, PL3, and NdP2), gliding
159 motility (AKMT and MyoA), and homeostasis/biogenesis (NHE3, VHA1, NST2, and ERK7). MyoA
160 phosphorylation was observed at S20 and S21, which was previously shown to be
161 phosphorylated by CDPK3 and required for gliding motility (Gaji et al., 2015). SCE1
162 phosphorylation was observed at S225, which was previously shown to be phosphorylated by

CDPK3 and required to relieve inhibition during Ca^{2+}-stimulated egress (McCoy et al., 2017). Our analysis highlights temporally-resolved changes in the phosphoproteome in response to zaprinast stimulation. We identify a subset of proteins phosphorylated by CDPK1 that likely represent factors involved in motility-related exocytosis, which we discuss in further detail below.

Myristoylation modulates CDPK1 activity and alters its interacting partners

CDPK1 was found to be myristoylated on Gly2 (Broncel et al., 2020). Myristoylation results in lipid modifications on proteins that can impact membrane targeting and protein-protein interactions (Martin et al., 2011; Wright et al., 2014). The myristoylated proteome of *T. gondii* was recently characterized using metabolic tagging and enrichment (Broncel et al., 2020). In this approach, parasites were grown in the presence of a myristic acid analogue containing a terminal alkyne group (YnMyr) that allowed enrichment of labeled proteins through click chemistry (Heal et al., 2011). We assessed whether myristoylation of CDPK1 affects the kinase's function. We validated myristoylation of CDPK1 using myristoylation-dependent pull downs followed by immunoblot detection and MS analysis (**Figure 2—figure supplement 1**). To investigate the role of myristoylation on CDPK1 function, an inducible knock-down strain (iKD) was generated by introducing a mAID-Myc tag at its C terminus (**Figure 2—figure supplement 1**). Auxin-dependent depletion was confirmed using immunoblot (**Figure 2—figure supplement 1**). Depletion of CDPK1 abolished ionophore-induced egress, as expected from previous results (**Figure 2—figure supplement 1**)(Lourido et al., 2010). Next, we complemented the iKD parasites by introducing HA-tagged WT (cWT) or myristoylation defective (cMut, G2A) copies of *CDPK1* into the *UPRT* locus (**Figure 2A**). We verified correct integration of both complementation constructs (**Figure 2—figure supplement 1**), and confirmed their equivalent and constitutive expression, as well as the auxin sensitivity of the endogenous mAID-tagged CDPK1 (**Figure 2B**). As predicted, the cMut allele was not myristoylated, based on acylation-dependent pull downs and immunoblotting (**Figure 2C**).

Given that myristoylation is frequently reported to facilitate membrane association, we examined the localization of cWT and cMut CDPK1 by immunofluorescence (**Figure 2D**). No clear differences were detected between the punctate cytosolic patterns of cWT and cMut. We explored possible effects of myristoylation on the subcellular fractionation of CDPK1 resolved using differential centrifugation (**Figure 2E**). First, we evaluated the fractionation pattern of the endogenous, myristoylated CDPK1. YFP-expressing parasites were metabolically labeled with Myr or YnMyr and lysed in a hypotonic buffer to preserve intact membrane structures. Next, lysates were fractionated to generate a low-speed pellet and supernatant at 16,000 x *g*. The low-speed supernatant was fractionated further into a high-speed pellet and supernatant at 100,000 x *g*. Click reaction based pull down and immunoblotting were used to resolve myristoylation-dependent partitioning. In contrast to the doubly acylated GAP45, which was present exclusively in the low-speed pellet, myristoylated CDPK1 was observed in the low-speed pellet and supernatant, and the high-speed pellet (**Figure 2E**), suggesting a potential association with membranous structures or higher molecular weight complexes. We next used both the cWT and cMut lines to elucidate any myristoylation-dependent changes to CDPK1 localization. While cWT

205 could be found predominantly in the high-speed pellet, loss of myristoylation released cMut into
206 the high-speed supernatant confirming an association with membranous structures or large
207 protein complexes (**Figure 2F**).
208
209 To evaluate the role of CDPK1 myristoylation in parasite fitness, we performed plaque assays
210 comparing the various strains (**Figure 2G**). In the presence of the endogenous copy of CDPK1,
211 both complemented lines developed normally. However, upon auxin-mediated depletion of
212 endogenous CDPK1, cMut plaque size substantially decreased. This finding demonstrates that
213 one or more steps of the *T. gondii* lytic cycle are negatively affected by the loss of CDPK1
214 myristoylation. In light of CDPK1's known function, we next explored whether CDPK1
215 myristoylation might impact the parasite's ability to egress from host cells. In the absence of
216 auxin, cWT, cMut, and the parental line (iKD) egressed within two min of ionophore stimulation
217 (**Figure 2—figure supplement 1**). While cWT parasites maintained similar egress kinetics
218 following auxin treatment, cMut parasites showed a significant delay after two min of treatment
219 (**Figure 2H**). This egress delay was overcome by six min, suggesting that CDPK1 myristoylation
220 is important for ionophore-induced egress, but not essential.
221
222 Finally, we wanted to examine whether myristoylation of CDPK1 affects its interactions with other
223 proteins, which may occur by direct binding to the kinase or by indirect association with a shared
224 membrane structure. We performed immunoprecipitation mass spectrometry (IP-MS) on HA-
225 tagged CDPK1 from cWT, cMut, and untagged TIR1 parasites after hypotonic lysis. CDPK1 was
226 the most significantly enriched protein across both cWT and cMut pulldowns when compared
227 to untagged controls (**Figure 2I**). Two additional proteins were significantly enriched along with
228 CDPK1: NUP134 (TGGT1_240510) and SRS36D (TGGT1_292280). Comparing the cWT and
229 cMut pulldowns, we found two proteins preferentially associated with cWT: NUDIX hydroxylase
230 (TGGT1_227450) and a 14-3-3 protein (TGGT1_269960) (**Figure 2J**). Loss of myristoylation
231 appears to enhance interactions with three different proteins: ROM4 (TGGT1_268590), a putative
232 T complex protein 1 alpha subunit (TGGT1_229990), and IMP dehydrogenase (TGGT1_233110).
233 Genome-wide knockout screen data suggest that NUP134 and the putative T complex protein
234 1 are the only putative interacting partners required for parasite fitness (Sidik et al., 2016b).
235 NUP134 binds and co-localizes with the nuclear pore complex, whereas the putative T complex
236 protein 1 may function as an ATP-dependent chaperone (Courjol et al., 2017). CDPK1 is localized
237 primarily to the cytoplasm of the parasite and partially in the nucleus, which could explain its
238 interactions with NUP134 (Lourido et al., 2010; Ojo et al., 2010). ROM4 is an integral membrane
239 protease required to shed secreted microneme proteins through proteolysis, and its knockdown
240 impaired gliding motility and invasion of host cells (Buguliskis et al., 2010). ROM4 localizes to
241 the plasma membrane of parasites but was enriched with cytosolic CDPK1 and was not
242 observed in our sub-minute resolution phosphoproteomics. Our pulldowns did not reveal a
243 membrane compartment association for myristoylated CDPK1 but did identify interacting
244 proteins enriched in cytosolic and myristoylated CDPK1. Given the annotated functions of these
245 interacting proteins, the factors are unlikely to participate in the motility-related functions of

CDPK1. Additional studies will be required to understand how myristoylation influences CDPK1 activity.

Identification of direct CDPK1 targets through thiophosphorylation

Our phosphoproteomic time course experiment identified proteins exhibiting CDPK1-dependent phosphorylation in live parasites, which includes direct and indirect substrates of the kinase. CDPK1 is unusual among apicomplexan and metazoan kinases in that it contains a glycine at its gatekeeper residue, resulting in an expanded ATP-binding pocket that can accommodate bulky ATP analogues. CDPK1 can use bulky analogues like *N*6-furfuryladenosine (kinetin)-5′-*O*-[3-thiotriphosphate] (KTPγS) to thiophosphorylate its substrates in parasite lysates (Lourido et al., 2013a). Thiophosphorylated substrates can subsequently be enriched with an iodoacetyl resin (Blethrow et al., 2008). Specificity can be assessed by comparison to mutant parasites harboring a G128M gatekeeper mutation in CDPK1 ($CDPK1^{M}$) that retains kinase activity but prevents it from using KTPγS. Previous studies using lysates identified a small set of six putative CDPK1-dependent substrates; however, these studies lost the target specificity conferred by the subcellular context and lacked the accuracy and sensitivity of quantitative proteomic approaches (Lourido et al., 2013a).

We implemented several modifications to the thiophosphorylation procedure that improved identification of CDPK1 targets (**Figure 3A**)(Rothenberg et al., 2016). First, we used stable isotope labeling of amino acids in cell culture (SILAC) to directly compare thiophosphorylation in WT ($CDPK1^{G}$) and mutant ($CDPK1^{M}$) parasites. Second, we used parasites semi-permeabilized with the bacterial toxin aerolysin—as opposed to the preparations of detergent-lysed parasites used in prior methods. Aerolysin forms 3-nm pores in the plasma membrane which permit the diffusion of small molecules but not proteins, enabling us to perform labeling reactions without drastically disrupting the concentration or localization of proteins (Iacovache et al., 2006). Lastly, we prevented non-specific extracellular substrate labeling due to premature lysis by treating semi-permeabilized parasites with 1B7, a nanobody that allosterically inhibits CDPK1 but does not enter the cytosol of semi-permeabilized parasites (**Figure 3B**)(Ingram et al., 2015).

Thiophosphorylation experiments were performed in biological triplicate comparing $CDPK1^{G}$ and $CDPK1^{M}$ parasites. We assessed thiophosphorylation labeling by immunoblot, identifying an array of proteins specifically labeled in $CDPK1^{G}$, but not $CDPK1^{M}$ parasites (**Figure 3C**). MS analyses quantified the abundance of peptides in $CDPK1^{G}$ relative to $CDPK1^{M}$ parasites, identifying 734 unique peptides across three biological replicates (**Figure 3D**). Samples from $CDPK1^{G}$ parasites were significantly enriched in phosphorylated peptides, consistent with CDPK1-mediated thiophosphorylation of targets (**Figure 3E**). 123 peptides across 104 proteins were likely direct substrates of CDPK1. GO enrichment analysis did not reveal any pathways relevant to the function of CDPK1 in exocytosis (**Figure 3F**). While our approach largely maintains kinases in their subcellular context, aerolysin treatment disrupts native ion concentrations and detaches the plasma membrane from the inner membrane complex (IMC) (Wichroski et al., 2002).

287 We therefore proceeded to consider the thiophosphorylated substrates in the context of the
288 time-resolved phosphoproteomics.
289
290 **CDPK1 targets participate in pathways controlling parasite motility**

291 Considering the thiophosphorylation and time-resolved phosphoproteomics, we arrived at a
292 prioritization scheme to identify 163 proteins phosphorylated in a CDPK1-dependent manner
293 (**Figure 3G**). Proteins were divided into five classes based on the overlap of phosphorylated sites
294 between both approaches. Class 1 contains five proteins for which the same phosphorylated
295 site was identified in both the time course and thiophosphorylation experiments. Class 2 contains
296 four proteins for which phosphorylated sites identified across both approaches were within 50
297 amino acid residues of one another. Class 3 contains two proteins that were enriched by
298 thiophosphorylation and were also CDPK1-dependent in the time course, but the identified sites
299 were more than 50 residues apart. Class 4 contains 93 proteins that were exclusively enriched
300 by thiophosphorylation. Lastly, Class 5 contains 59 proteins that were CDPK1-dependent
301 exclusively in the time course and are likely indirect targets of the kinase. Proteins within each
302 class were further stratified by fitness scores reported from genome-wide knockout screens,
303 with lower scores representing genes more essential for parasite fitness in cell culture (Sidik et
304 al., 2016b). Of the 163 targets of CDPK1, 72 proteins across all classes also displayed changes
305 in zaprinast-dependent phosphorylation at distinct sites that were independent of CDPK1. This
306 overlap suggests that some proteins modified by CDPK1 are also regulated by additional kinases
307 and phosphatases.
308
309 We hypothesized that regulators of exocytosis would be found among the targets of CDPK1. Of
310 the 163 protein targets, 38 have been previously localized and/or functionally characterized
311 (indicated with asterisks; **Figure 3G**). Of these 38 proteins, 13 have been implicated in regulating
312 motile stages of the parasite (**Figure 3H, Figure 3—figure supplement 1**). Among the
313 candidates associated with microneme exocytosis, centrin 2 (CEN2) and RNG2 have previously
314 been localized to tubulin-based structures in the apical complex of the parasite, and their
315 knockdown is sufficient to inhibit secretion of microneme proteins and block host cell invasion
316 (Katris et al., 2014; Lentini et al., 2019; Leung et al., 2019). Candidates associated with rhoptry
317 exocytosis include the armadillo repeats only protein (ARO), ARO-interacting protein (AIP),
318 palmitoyl acyltransferase DHHC7, and patatin-like phospholipase (PL3) (Beck et al., 2013;
319 Mueller et al., 2016, 2013; Wilson et al., 2020). ARO and DHHC7 both localize to the cytosolic
320 face of rhoptries, where they influence the recruitment of AIP and ACβ. Knockdown of either
321 DHHC7 or ARO disrupts the localization of mature rhoptries, inhibiting the secretion of rhoptry
322 proteins required for invasion. Another potential CDPK1 target, the apical complex lysine
323 methyltransferase (AKMT), rapidly relocalizes from the apical complex to the parasite body
324 during Ca^{2+}-regulated motility, and its knockdown impairs the gliding motility of parasites
325 required for invasion and egress (Heaslip et al., 2011). Other putative CDPK1 targets participate
326 in homeostasis and biogenesis of secretory organelles, such as the vacuolar type Na^+/H^+
327 exchanger (NHE3), dynamin-related protein B (DrpB), V-ATPase a1 (VHA1), and GDP-fucose
328 transporter (NST2). NHE3-knockout parasites exhibit sensitivity to osmotic shock and

329 dysregulated cytosolic Ca^{2+}, resulting in reduced secretion of microneme proteins and an
330 inhibition of invasion (Francia et al., 2011). DrpB was previously identified as a CDPK1 target,
331 and its depletion results in severe defects in the biogenesis of micronemes and rhoptries
332 (Breinich et al., 2009; Lourido et al., 2013a). VHA1 and NST2 participate in the maturation of
333 microneme and rhoptry proteins (Bandini et al., 2019; Stasic et al., 2019). Lastly, signaling
334 proteins regulating intracellular cGMP levels, such as the guanylate cyclase (GC) and the unique
335 GC organizer (UGO), were also phosphorylated in a CDPK1-dependent manner (Bisio et al.,
336 2019; Brown and Sibley, 2018; Yang et al., 2019). CDPK1 acts downstream of GC-mediated
337 production of cGMP, which may suggest regulatory feedback on Ca^{2+} release, as has been
338 suggested for CDPK3 (Nofal et al., 2022). These data demonstrate that identification of CDPK1
339 targets can uncover proteins involved in Ca^{2+}-regulated exocytosis.
340
341 To identify new factors involved in Ca^{2+}-regulated secretion, we prioritized Class 1 and Class 2
342 candidates. Seven candidates in this category lack functional annotation or have been
343 associated with apical structures: TGGT1_227610, TGGT1_221470, TGGT1_235160,
344 TGGT1_254870, KinesinB (TGGT1_273560), a small nuclease (TGGT1_310060), and
345 TGGT1_289100 (MIC18). TGGT1_221470 was previously identified as a CDPK1 substrate after
346 a pull down from parasite lysates but remained functionally uncharacterized (Lourido et al.,
347 2013a). KinesinB localizes to cortical microtubules, TGGT1_254870 localizes to the apical
348 complex, and TGGT1_289100 co-localizes with micronemes, each of which are parasite
349 structures relevant to exocytosis (Butler et al., 2014; Leung et al., 2017; Long et al., 2017). Of
350 these candidates, only TGGT1_227610 and TGGT1_289100 appear to be required for parasite
351 fitness (Long et al., 2017; Sidik et al., 2016b). Despite prior annotation as a microneme protein,
352 TGGT1_289100 lacks a signal peptide and is localized to the cytosol by spatial proteomics
353 (Barylyuk et al., 2020; Butler et al., 2014). Instead, TGGT1_289100 is predicted to have an N-
354 terminal Hook domain and extensive coiled-coil domains (Simm et al., 2015; Söding et al., 2005)
355 with homology to activating adaptors that bind to endosomes and activate super-processive
356 dynein-mediated trafficking towards the minus end of microtubules (**Figure 4A**) (Bielska et al.,
357 2014; Guo et al., 2016; Zhang et al., 2014). The predicted polarity of cortical microtubules and
358 their association with micronemes support a model where the vesicles are trafficked by dyneins
359 towards the apical end of the parasite (Chen et al., 2015; Leung et al., 2017; Wang et al., 2021).
360 We observed extensive CDPK1-dependent phosphorylation between the Hook and coiled-coil
361 domains of TGGT1_289100 (S167, S177, and S189–191), consistent with potential regulation of
362 the putative adaptor. These data motivated functional characterization of this factor—henceforth
363 referred to as HOOK.
364
365 **A Hook domain protein phosphorylated by CDPK1 regulates parasite invasion**

366 To study the role of HOOK during the acute stages of the parasite, we generated a conditional
367 knockdown by fusing an HA-mAID tag to its N terminus (AID-HOOK; **Figure 4—Figure**
368 **supplement 1**). HOOK was depleted from parasites following 24–40 hrs of auxin treatment, as
369 determined by immunoblotting or immunofluorescence microscopy (**Figure 4B–C**). In contrast
370 to previous observations that localized HOOK to micronemes, we observed only partial co-

371 localization with micronemes with a majority of HOOK localized to the cytosol (**Figure 4C**).
372 Plaque formation was impaired when AID-HOOK parasites were grown in the presence of auxin,
373 consistent with the strong effect on parasite fitness reported from genome-wide knockout
374 screens (**Figure 4D**)(Sidik et al., 2016b). These results indicate that HOOK is required during the
375 acute stages of *T. gondii*. Parasite replication was not affected following 24 hrs of auxin
376 treatment (**Figure 4E**). Microneme and rhoptry biogenesis were also unaffected following 24 hrs
377 of auxin treatment immunofluorescence analysis (**Figure 4C**, **Figure 4—figure supplement 1**).
378 These data suggest HOOK functions during stages associated with parasite motility, such as
379 parasite invasion and egress. Parasites depleted of HOOK displayed reduced invasion efficiency,
380 consistent with that of CDPK1-depleted parasites (**Figure 4F**). We noted that even in the absence
381 of auxin treatment AID-HOOK parasites required longer incubations to reach comparable levels
382 of invasion to wildtype, suggesting that manipulation of the N terminus partially affects HOOK
383 function.
384
385 HOOK depletion only partially recapitulates the effects of CDPK1 loss. Parasites depleted of
386 CDPK1 were unable to egress—as documented previously (Lourido et al., 2012, 2010)—whereas
387 depletion of HOOK had no effect on parasite egress (**Figure 4G**). Finally, we also examined
388 whether the stability of CDPK1 affected HOOK expression by tagging the C terminus of HOOK
389 with a 3xHA tag in CDPK1 cKD parasites (HOOK-3xHA). HOOK localization and abundance was
390 unaffected by depleting parasites of CDPK1 for 24 hrs as determined by immunofluorescence
391 (**Figure 4H**). Taken together, our results indicate that HOOK is required for invasion of host cells,
392 but dispensable for egress.
393
394 **HOOK forms a complex that regulates parasite invasion**

395 Opisthokont HOOK proteins function in complexes to activate dynein-mediated trafficking of
396 vesicular cargo along microtubules (Bielska et al., 2014; Christensen et al., 2021; Gillingham et
397 al., 2014; Guo et al., 2016; Xu et al., 2008; Yao et al., 2014). In *D. melanogaster* and mammals,
398 HOOK proteins have been shown to form dimers and bind FTS and FHIP via a C-terminal region
399 that interacts with vesicular cargo (Christensen et al., 2021; Krämer and Phistry, 1996; Lee et al.,
400 2018; Xu et al., 2008). To identify analogous binding partners of HOOK in *T. gondii*, we performed
401 IP-MS on lysates from HOOK-3xHA parasites and an untagged control (**Figure 5A**). Three
402 proteins showed comparable enrichment to HOOK-3xHA: TGGT1_264050, TGGT1_316650, and
403 TGGT1_306920. Like FTS, TGGT1_264050 bears homology to E2 ubiquitin-conjugating
404 enzymes, but lacks the catalytic cysteine required for enzymatic activity at position 162. Because
405 of these shared features and their homology, we designated TGGT1_264050 as FTS.
406
407 To confirm that FTS forms a complex with HOOK, we investigated its localization and performed
408 reciprocal IPs. We fused a 3xHA tag to the C terminus of FTS and observed a similar localization
409 to HOOK by immunofluorescence: primarily cytosolic with partial overlap with micronemes
410 (**Figure 5B**). To identify binding partners of FTS, we performed IP-MS on FTS-3xHA parasite
411 lysates and compared protein enrichment to the HOOK-3xHA IP (**Figure 5C**). Four proteins were

412 significantly enriched in the reciprocal IP experiments—HOOK, FTS, TGGT1_316650, and
413 TGGT1_306920—confirming the four-member complex.
414
415 To determine whether FTS functions in the same pathway as HOOK, we generated a conditional
416 knockdown by fusing an AID-HA tag to the C terminus of FTS (FTS-AID; **Figure 5—Figure**
417 **supplement 1**). FTS was readily depleted from parasites following 40 hrs of auxin treatment
418 (**Figure 5D**). FTS depletion completely blocked plaque formation (**Figure 5E**). Similar to HOOK,
419 depletion of FTS had no observable effect on parasite replication or microneme biogenesis
420 (**Figure 5—figure supplement 1**, **Figure 5F**). During the motile stages of the parasite, FTS
421 depletion resulted in a block in invasion efficiency but had no effect on egress, phenocopying
422 the effects of HOOK depletion (**Figure 5G**, **Figure 5H**). FTS appeared to tolerate tagging better
423 than HOOK, since the FTS-AID parasites behaved normally in the absence of auxin. These data
424 suggest that HOOK and FTS form a functional complex required for parasite invasion.
425
426 We pursued enzyme-catalyzed proximity labeling to complement IP-MS studies and capture
427 transient protein interactions (Branon et al., 2018). In this approach, cells express a protein of
428 interest tagged with the promiscuous biotin ligase TurboID. Addition of a biotin substrate to live
429 cells results in biotinylation within a few nanometers of the TurboID-tagged protein, in a matter
430 of minutes. Biotinylated proteins can be enriched from cellular lysates using streptavidin-affinity
431 purification and identified using MS. Proximity labeling was recently used to characterize the
432 cargo diversity of distinct human FHF complexes in human cells (Christensen et al., 2021). To
433 identify additional proteins that interact with the *T. gondii* HOOK complex, we performed
434 proximity labeling after fusing TurboID to the C terminus of FTS, which was more amenable to
435 tagging compared to HOOK (**Figure 5I**, **Figure 5—figure supplement 1**). As a control, we used
436 parasites expressing a cytosolic mNeonGreen-TurboID that would broadly label cytosolic
437 proteins and identify non-specific interactions (**Figure 5—figure supplement 1**).
438
439 Of the 14 proteins significantly enriched in FTS-TurboID parasites, members of the HOOK
440 complex (HOOK, FTS, TGGT1_306920, and TGGT1_316650) were the top four most enriched
441 proteins. In humans, proximity labeling studies suggest FTS and FHIP bind at the C terminus of
442 the HOOK dimer to mediate FHIP binding to RAB5 endosomes (Christensen et al., 2021). Our
443 FTS proximity labeling results suggest that TGGT1_306920 and TGGT1_316650 may also bind
444 in this manner. Among the other significantly-enriched proteins, PC and ACC1 encode
445 carboxylases known to be covalently modified by biotin and likely represent non-specific
446 enrichment. DHFR enrichment is likely due to its use as a selectable marker when generating the
447 FTS-TurboID strain. TGGT1_294610 and TGGT1_280770 are a putative histone lysine
448 methyltransferase and regulator of chromosome condensation (RCC1)-repeat containing
449 protein, respectively, and have no characterized functions. Of the remaining enriched proteins
450 that lack annotations, TGGT1_221180 was previously localized to micronemes by spatial
451 proteomics and contains a transmembrane domain, suggesting a molecular link between the
452 HOOK complex and micronemes (Barylyuk et al., 2020).
453

454 **The HOOK complex promotes invasion by regulating microneme exocytosis**

455 To determine whether the HOOK complex is required for microneme exocytosis, we directly
456 measured secretion of the microneme protein MIC2. Microneme exocytosis exposes integral
457 membrane proteins like MIC2 that function as adhesins during gliding motility. These adhesins
458 subsequently undergo proteolytic cleavage and are released into the supernatant, which can be
459 analyzed by immunoblot (Carruthers et al., 2000). Quantification of the proportion of secreted
460 MIC2 was performed by generating a standard curve from unstimulated lysates. Strikingly,
461 parasites depleted of either member of the HOOK complex were severely impaired in their ability
462 to secrete microneme proteins (**Figure 5J**). Inhibition of the complex led to a similar degree of
463 secretion impairment as CDPK1 depletion. Together, these data suggest that HOOK and FTS
464 form a functional complex that is required for microneme exocytosis.
465
466 **Microneme trafficking depends on CDPK1 activity and HOOK**

467 We hypothesized that if the HOOK complex is required for sustained microneme exocytosis,
468 then depletion of HOOK would inhibit trafficking of micronemes during parasite motility. Dynamic
469 relocalization of micronemes can be visualized using live microscopy of parasites expressing the
470 integral microneme protein CLAMP fused to mNeonGreen (CLAMP-mNG) (**Figure 6A**)(Sidik et
471 al., 2016b). To trigger microneme exocytosis, parasites are treated with zaprinast to stimulate a
472 rise in intracellular Ca^{2+} and activate CDPK1. Dynamic relocalization of micronemes is defined
473 as the CLAMP-mNG signal that concentrates at the apical end of the parasite over time. To
474 quantify microneme relocalization, mNG signal is measured, over time, along the apical-basal
475 axis of individual parasites within a vacuole. We scored microneme relocalization by calculating
476 the difference in maximum apical intensity comparing the instant of zaprinast addition to the time
477 point just prior to parasite egress of the uninhibited zaprinast-stimulated controls (**Figure 6A**).
478
479 We first assessed whether CDPK1 kinase activity is required for microneme relocalization using
480 the specific inhibitor 3-MB-PP1 (Lourido et al., 2010). We incubated parasites with 3-MB-PP1
481 for 30 min, imaged for 1 min to establish a baseline, and then stimulated with zaprinast. Parasites
482 pre-treated with DMSO relocalized micronemes as expected; however, microneme relocalization
483 was blocked when CDPK1 was inhibited by 3-MB-PP1 (**Figure 6B-D**). These results indicate
484 microneme relocalization depends on CDPK1 kinase activity.
485
486 We next assessed whether HOOK is also required for microneme relocalization. We fused an
487 mNG reporter to the C terminus of CLAMP in AID-HOOK parasites and TIR1 parasites as a
488 control (**Figure 6—Figure supplement 1**). We treated parasites with auxin for 24 hrs prior to
489 stimulation with zaprinast. Microneme relocalization was unaffected in TIR1/CLAMP-mNG
490 parasites treated with auxin (**Figure 6E–F**). By contrast, microneme relocalization did not occur
491 in intracellular AID-HOOK parasites regardless of auxin treatment (**Figure 6G–H**). We attributed
492 the lack of relocalization in vehicle-treated parasites to the hypomorphism resulting from N-
493 terminal tagging, which is consistent with the delayed invasion and reduced plaque size
494 documented for this strain. To determine whether vehicle-treated AID-HOOK parasites
495 relocalized micronemes over longer periods, we examined CLAMP-mNG localization in

496 extracellular parasites after egress. While vehicle-treated AID-HOOK parasites were able to
497 relocalize micronemes, parasites depleted of HOOK exhibited a striking microneme localization
498 dispersed throughout the cytosol (**Figure 6I–J**). As expected, TIR1/CLAMP-mNG parasites
499 maintained the apical relocalization of micronemes regardless of auxin treatment in extracellular
500 parasites. We used an alternative metric for microneme relocalization to account for the
501 disorganized localization of micronemes in parasites depleted of HOOK. We quantified the
502 percent of the total CLAMP-mNG signal localized to the apical end versus the remaining body
503 of the parasite (**Figure 6K**). The apical region cutoffs were experimentally derived from vehicle-
504 treated TIR1/CLAMP-mNG parasites and defined as the apical 12.5% of the parasite. While a
505 majority of CLAMP-mNG signal was localized to the apical region of TIR1/CLAMP-mNG
506 parasites, most of the CLAMP-mNG signal observed in parasites depleted of HOOK was found
507 in the parasite body. Micronemes rapidly adopt an aberrant localization in the absence of HOOK
508 during parasite motility. These results indicate that CDPK1 kinase activity and HOOK are
509 required for microneme trafficking during parasite motility.
510
511 **DISCUSSION**

512 In this study, we sought to identify new regulators of Ca^{2+}-mediated exocytosis in *T. gondii* by
513 studying the targets of a key regulator, the kinase CDPK1. We identified 163 proteins
514 phosphorylated in a CDPK1-dependent manner using sub-minute resolution
515 phosphoproteomics and thiophosphorylation for direct substrate capture. We determined that
516 myristoylation of CDPK1 contributes to the kinase's function during the lytic cycle. 13 of the
517 identified CDPK1 targets have previously described functions in parasite motility, revealing
518 possible points of regulation within relevant signaling pathways. Furthermore, we characterized
519 a new regulator of microneme exocytosis called HOOK, which forms a stable complex with FTS
520 and two other proteins. Homologs of HOOK and FTS participate in dynein-mediated vesicular
521 trafficking in other organisms. In *T. gondii*, knockdown of HOOK or FTS blocked invasion of host
522 cells and altered rapid microneme trafficking during Ca^{2+}-regulated motility. Overall, we show
523 how studying parasite signaling pathways can illuminate the cellular adaptations that support
524 parasitism.
525
526 Over the past decade, several efforts have sought to characterize phosphorylation within
527 apicomplexans. Improvements in phosphopeptide enrichment and mass spectrometry have
528 enabled global characterization of the phosphoproteomes from *T. gondii* tachyzoites and
529 *P. falciparum* schizonts, trophozoites, and ring-stages(Lasonder et al., 2012; Pease et al., 2013;
530 Solyakov et al., 2011; Treeck et al., 2011). Coupling such approaches with genetic and
531 pharmacological tools has enabled the deconvolution of kinase-specific effects from the vast
532 global phosphorylation program(Blomqvist et al., 2020; Fang et al., 2017; Invergo et al., 2017;
533 Nofal et al., 2022; Pease et al., 2018; Treeck et al., 2014), revealing the activation of MyoA-
534 mediated gliding by *Tg*CDPK3, the roles of *Pb*CDPK4 and *Pb*SRPK1 during male
535 gametogenesis, and the erythrocytic-stage effects of *Pf*CDPK1, *Pf*PK7, and *Pf*CDPK5(Blomqvist
536 et al., 2020; Fang et al., 2017; Gaji et al., 2015; Invergo et al., 2017; Pease et al., 2018; Tang et
537 al., 2014). Attributing individual phosphorylation events to specific kinases can be complicated

538 by cumulative changes or adaptation of the signaling networks in knockouts. Chemical-genetic
539 approaches can more precisely inhibit the activity of a given kinase at the time of the assay,
540 while controlling for off-target effects, and have been used to characterize *Pf*PKG-dependent
541 phosphorylation (Alam et al., 2015; Brochet et al., 2014). Kinetically-resolved
542 phosphoproteomics has enabled a more nuanced understanding of signaling cascades during
543 parasite motility(Herneisen et al., 2022; Invergo et al., 2017; Nofal et al., 2022). While such
544 technical advances have led to more in-depth phosphoproteome mapping, identifying the direct
545 targets of a given kinase remains a key challenge to structuring the observed changes into
546 signaling pathways.
547
548 To resolve direct and indirect effects on the phosphoproteome for *T. gondii* CDPK1, we
549 combined two complementary approaches: temporally-resolved phosphoproteomics and bio-
550 orthogonal labeling of direct substrates. We implemented several methodological advances.
551 Rapid conditional knockdown using the auxin-inducible degron system resulted in rapid and
552 specific depletion of the kinase of interest for the phosphoproteomic studies(Brown et al., 2018).
553 Additionally, quantification and coverage by mass spectrometry were improved through TMTpro
554 multiplexing and ion mobility spectrometry (FAIMS)(Bekker-Jensen et al., 2020; Van Vranken et
555 al., n.d.). We also improved on the low coverage observed in previous thiophosphorylation
556 experiments with parasite lysates(Fang et al., 2017; Lourido et al., 2013a) by maintaining a more
557 native signaling environment using aerolysin semi-permeabilization, SILAC-based peptide
558 quantification, and shortened labeling times(Rothenberg et al., 2016). These approaches
559 characterize proteome-wide phosphorylation kinetics in live parasites and reveal direct kinase-
560 substrate relationships for CDPK1.
561
562 Myristoylation of CDPK1 contributes to its function. Contrary to previous reports describing the
563 kinase as cytosolic or nuclear(Ojo et al., 2010; Pomel et al., 2008), we demonstrate that
564 myristoylated CDPK1 is at least partially associated with structures that can be fractionated from
565 the cytoplasm by differential centrifugation. Loss of myristoylation led to CDPK1 release from
566 the insoluble fraction. The ortholog of CDPK1 in *P. berghei*, *Pb*CDPK4, also displays
567 myristoylation-specific functions during male gametogenesis: myristoylated *Pb*CDPK4 is critical
568 for the first genome replication, whereas the non-myristoylated *Pb*CDPK4 is important for the
569 completion of gametogenesis(Fang et al., 2017). Myristoylation could impact CDPK1's ability to
570 access certain targets efficiently. However, such interactions appear to be too weak or transient
571 to be captured by immunoprecipitation. Mutating the myristoylation site of CDPK1 only modestly
572 affected ionophore-induced egress. However, minor effects in these key transitions may be
573 magnified over repeated lytic cycles, which may explain the more substantial impact of losing
574 CDPK1 myristoylation on plaque formation. Alternatively, other kinases may compensate for
575 decreased CDPK1 activity, particularly under hyperactivated conditions like stimulated egress.
576 A plausible candidate for compensation is CDPK2A, which also appears to be myristoylated,
577 despite lacking an N-terminal MG motif, and was recently shown to display epistatic interactions
578 with CDPK1(Broncel et al., 2020; Shortt et al., 2022).
579

580 CDPK1 plays a critical role in the transition from the replicative intracellular stages to motile
581 extracellular stages (Lourido et al., 2010; Shortt et al., 2022). During this transition parasites must
582 execute rapid cellular changes that involve the exocytosis of micronemes and rhoptries,
583 reorganization of the cytoskeleton, gliding motility, and maintenance of ion homeostasis(Blader
584 et al., 2015). CDPK1 has also been suggested to control the actomyosin system and extrusion
585 of the conoid(Tosetti et al., 2019). Our detailed target analysis suggests CDPK1 regulates—and
586 possibly helps coordinate—multiple pathways. We revealed over a hundred CDPK1 targets with
587 diverse predicted functions, including many relevant to phenotypes dependent on CDPK1. In
588 addition to the effects on microneme trafficking examined in this study, our results point to a
589 direct link between CDPK1 and rhoptry exocytosis. Ca^{2+} has been implicated in rhoptry
590 discharge, as the rhoptry-localized Ca^{2+}-binding FER2 is required for rhoptry
591 exocytosis(Coleman et al., 2018). We observed a preponderance of CDPK1-dependent
592 phosphorylation on proteins regulating rhoptry exocytosis, including DHHC7, ARO, and AIP.
593 Phosphorylation on ARO was observed near the N-terminal acylation sites required for rhoptry
594 targeting and may regulate the bundling and positioning of mature rhoptries during motile
595 stages(Mueller et al., 2016). However, formally demonstrating the relationship between
596 Ca^{2+}/CDPK1 and rhoptry discharge is complicated by the dependency of the latter on the
597 secretion of certain microneme proteins (Ben Chaabene et al., 2021; Carruthers and Sibley,
598 1997). *T. gondii* tachyzoites have several rhoptries, yet only two are docked for exocytosis at a
599 given time (Aquilini et al., 2021; Mageswaran et al., 2021; Segev-Zarko et al., 2022). Regulating
600 the activity of ARO during motile stages may influence the ability to mobilize and re-dock
601 rhoptries in preparation for invasion. Considering how different CDPK1 substrates function, we
602 expect the various phenotypes associated with CDPK1 will depend on distinct sets of
603 substrates.
604
605 Although CDPK1 is known to mediate microneme exocytosis (Lourido et al., 2010), the precise
606 molecular events controlling this process have remained elusive. In this study, we determined
607 that CDPK1 activity is required for the Ca^{2+}-stimulated trafficking of micronemes to the apical
608 end. This phenotype depends on HOOK, one of the CDPK1 targets uncovered by both global
609 phosphoproteomics and thiophosphorylation studies. Despite prior annotation as a microneme
610 protein(Butler et al., 2014), HOOK likely functions as an activating adaptor in *T. gondii* based on
611 homology to other Hook proteins and the functional characterization we have performed. In
612 particular, immunoprecipitation of HOOK identified three interacting proteins: FTS,
613 TGGT_316650, and TGGT1_306920. In *H. sapiens*, *A. nidulans*, and *D. melanogaster*, Hook
614 proteins complex with FTS and FHIP (the FHF complex), to link cargo to the dynein machinery
615 for trafficking along microtubules(Bielska et al., 2014; Gillingham et al., 2014; Guo et al., 2016;
616 Xu et al., 2008; Yao et al., 2014). FHF complexes have been shown to recognize early endosomes
617 via FHIP binding to RAB5(Bielska et al., 2014; Guo et al., 2016; Zhang et al., 2014). Homology to
618 FHIP was lacking in TGGT1_316650 and TGGT1_306920. However, genome-wide knockout
619 screens indicate TGGT1_306920 is critical for parasite fitness, leading us to speculate that it may
620 mediate cargo binding in a manner structurally distinct from known adaptors. Additional work
621 will be needed to elucidate the function of the HOOK complex and to understand how it mediates
622 trafficking of apicomplexan-specific organelles.

623
624 Our results place the HOOK complex downstream of CDPK1, regulating the stimulated
625 relocalization of micronemes to the apical end of parasites. However, the HOOK complex only
626 partially explains CDPK1's role during egress. Whereas CDPK1 depletion blocks egress entirely,
627 parasites depleted of HOOK or FTS exit host cells, despite subsequent defects in microneme
628 secretion and invasion. Microneme discharge is required for egress, supplying adhesins for
629 gliding motility and the perforin PLP1 to rupture the parasitophorous vacuole membrane(Kafsack
630 et al., 2009). It therefore appears that the initial round of microneme discharge during egress
631 depends on CDPK1, and only subsequent rounds require the HOOK complex. Indeed, a fraction
632 of micronemes are already found docked at the apical complex prior to the transition from the
633 replicative to the motile stages, and may constitute the first round of microneme
634 exocytosis(Mageswaran et al., 2021; Sun et al., 2022). Dynein-mediated trafficking might
635 become important immediately following egress when continuous microneme discharge is
636 necessary, as is the case during gliding motility and invasion. Consistent with this hypothesis,
637 depletion of the dynein light chain 8a (DLC8a) yielded similar phenotypes to HOOK and FTS
638 knockdown: intact egress but dysfunctional microneme protein secretion, gliding motility, and
639 invasion(Lentini et al., 2019). Loss of DLC8a also led to defects in rhoptry positioning, which
640 were not observed in HOOK knockdowns(Lentini et al., 2019), so other activating adaptors may
641 be involved in rhoptry trafficking. Our results suggest that the HOOK complex has been
642 specifically adapted for microneme trafficking in *T. gondii*.
643
644 Several aspects of microneme trafficking remain to be determined. The precise nature of the
645 dynein complex is poorly understood. Eukaryotes typically express a single cytoplasmic dynein
646 heavy chain. In *T. gondii*, TGGT1_294550 is the top candidate for the cytoplasmic dynein heavy
647 chain (DHC) as it contains the necessary domains, is conserved among apicomplexans, and is
648 required for parasite fitness (Lentini et al., 2019; Sidik et al., 2016b). Other putative DHCs in the
649 *T. gondii* genome are likely axonemal dyneins required for flagellar function in sexual-stage
650 parasites. It also remains unknown how the HOOK complex binds to micronemes. In *H. sapiens*
651 and *D. melanogaster*, RAB5 on vesicles interacts with FHIP in the HOOK complex(Bielska et al.,
652 2014; Gillingham et al., 2014; Guo et al., 2016; Xu et al., 2008; Yao et al., 2014). We speculate
653 that TGGT1_306920 may serve the role of FHIP within the HOOK complex but its binding partner
654 on micronemes remains unknown. RAB5A and RAB5C have been implicated in the biogenesis
655 of micronemes, but their roles during exocytosis have not been explored(Kremer et al., 2013).
656 Understanding how micronemes are recognized may elucidate how cargo specificity is achieved
657 and regulated.
658
659 Ca^{2+} signaling has been tuned to support apicomplexan-specific cellular processes but
660 identifying and integrating effectors within the pathway has remained a major bottleneck.
661 Signaling effectors conserved amongst eukaryotes are often integrated into apicomplexan
662 cellular pathways in novel or unusual ways. Here, we identified candidate downstream effectors
663 of the Ca^{2+}-regulated kinase CDPK1 by monitoring proteome-wide protein phosphorylation. In
664 addition to creating a catalog of candidates for future characterization, we identified,
665 characterized, and integrated the HOOK complex downstream of CDPK1 within the Ca^{2+}

signaling network controlling microneme exocytosis. Lastly, our results are the first to implicate activating adaptors as critical factors for the pathogenesis of an apicomplexan organism by promoting exocytic trafficking.

MATERIALS & METHODS

Key resources table

Reagent type (species) or resource	Designation	Source or reference	Identifiers	Additional information
Strain, strain background (*T. gondii*)	TIR1	PMID: 28465425		RH/TIR1/ΔKU80/ΔHXGPRT
Strain, strain background (*T. gondii*)	CDPK1-AID	doi: https://doi.org/10.1101/2022.07.19.500742		RH/TIR1/ΔKU80/ΔHXGPRT/CDPK1-V5-mNeonGreen-mAID-Ty
Strain, strain background (*T. gondii*)	iKD CDPK1	This paper	TGGT1_301440	RH/TIR1/ΔKU80/ΔHXGPRT/CDPK1-mAID-Myc/HXGPRT
Strain, strain background (*T. gondii*)	cWT CDPK1	This paper	TGGT1_301440	RH/TIR1/ΔKU80/ΔHXGPRT/CDPK1-mAID-Myc/HXGPRT/CDPK1-HA-T2A-GFP
Strain, strain background (*T. gondii*)	cMut CDPK1	This paper	TGGT1_301440	RH/TIR1/ΔKU80/ΔHXGPRT/CDPK1-mAID-Myc/HXGPRT/CDPK1(G2A)-HA-T2A-mCherry
Strain, strain background (*T. gondii*)	Δku80Δhxgprt YFP			RH/ΔKU80/ΔHXGPRT/YFP
Strain, strain background (*T. gondii*)	CDPK1G	PMID: 19218426		RH/ΔKU80/ΔHXGPRT
Strain, strain background (*T. gondii*)	CDPK1M	PMID: 23149386	TGGT1_301440	RH/ΔKU80/ΔHXGPRT/CDPK1(G128M)-Myc

Strain, strain background (*T. gondii*)	AID-HOOK	This paper	TGGT1_289100	RH/TIR1/ΔKU80/ΔHXGPRT/HA-mAID-HOOK
Strain, strain background (*T. gondii*)	CDPK1-AID/HOOK-3xHA	This paper	TGGT1_289100	RH/TIR1/ΔKU80/ΔHXGPRT/CDPK1-V5-mNeonGreen-mAID-Ty/HOOK-V5-3HA/HXGPRT
Strain, strain background (*T. gondii*)	FTS-AID	This paper	TGGT1_264050	RH/TIR1/ΔKU80/ΔHXGPRT/FTS-V5-mAID-HA/HXGPRT
Strain, strain background (*T. gondii*)	FTS-3xHA	This paper	TGGT1_264050	RH/TIR1/ΔKU80/ΔHXGPRT/FTS-V5-3HA/HXGPRT
Strain, strain background (*T. gondii*)	FTS-TurboID	This paper	TGGT1_264050	RH/TIR1/ΔKU80/ΔHXGPRT/FTS-TurboID-Ty/DHFR
Strain, strain background (*T. gondii*)	cytosolic mNG-TurboID	This paper		RH/TIR1/ΔKU80/ΔHXGPRT/pMIC2-mNeonGreen-TurboID-Ty
Strain, strain background (*T. gondii*)	CLAMP-mNG	PMID: 27594426	TGGT1_265790	RH/ΔKU80/ΔHXGPRT/CLAMP-mNeonGreen
Strain, strain background (*T. gondii*)	TIR1/CLAMP-mNG	This paper	TGGT1_265790	RH/TIR1/ΔKU80/ΔHXGPRT/CLAMP-mNeonGreen
Strain, strain background (*T. gondii*)	TIR1/CLAMP-mNG/AID-HOOK	This paper	TGGT1_265790	RH/TIR1/ΔKU80/ΔHXGPRT/HA-mAID-HOOK/CLAMP-mNeonGreen
Cell line (*Homo sapiens*)	Human Foreskin Fibroblasts (HFFs)	ATCC	SCRC-1041	
Antibody	Mouse polyclonal anti-CDPK1	other		Provided by Matthew Child and Matt Bogyo. WB

				(1:3000). Only used in Figure 2.
Antibody	Mouse monoclonal clone 4A6 anti-Myc	Millipore	Cat# 05-724, RRID:AB_11211891	WB (1:1000)
Antibody	Rat monoclonal clone 3F10 anti-HA	Roche	Cat# 11867423001, RRID:AB_390919	WB (1:1000); IFA (1:1000). Only used in Figure 2.
Antibody	Mouse monoclonal clone TP3 anti-*Toxoplasma*	Abcam	Cat# ab8313, RRID:AB_306466	WB (1:1000)
Antibody	Rabbit polyclonal anti-GAP45	other		Provided by Peter Bradley Lab. WB (1:1000). Only used in Figure 2.
Antibody	Mouse monoclonal anti-GFP	Roche	Cat# 11814460001, RRID:AB_390913	WB (1:1000)
Antibody	Rabbit polyclonal anti-mCherry	Abcam	Cat# ab167453, RRID:AB_2571870	WB (1:1000)
Antibody	Rabbit monoclonal anti-SAG1	other		Provided by John Boothroyd Lab; WB (1:10,000). Only used in Figure 2.
Antibody	Rabbit monoclonal clone 51-8 anti-thiophosphate ester	Abcam	Cat# ab92570, RRID:AB_10562142	WB (1:5000)

Antibody	Mouse monoclonal clone 12G10 anti-tubulin	Developmental Studies Hybridoma Bank at the University of Iowa	RRID: AB_1157911	Provided by Marc-Jan Gubbels Lab. WB (1:2000)
Antibody	Guinea pig monoclonal anti-CDPK1	Covance	Custom antibody	WB (1/50,000)
Antibody	Rabbit monoclonal (C29F4) anti-HA	Cell Signaling Technology	Cat# 3724, RRID:AB_1549585	WB (1:1000); IFA (1:1600)
Antibody	Mouse monoclonal clone 6D10 anti-MIC2	PMID: 10799515		Provided by L. David Sibley Lab. WB (1:5000); IFA (1:2000)
Antibody	Mouse anti-ROP1	other		Provied by Peter Bradley Lab. IFA (1:2000)
Antibody	Mouse polyclonal anti-SAG1	PMID: 3183382		Provided by L. David Sibley Lab. IFA (1:500). Used for invasion assays.
Antibody	Rabbit polyclonal anti-GAP45	Lampire Biological Laboratory		Provided by R. Drew Etheridge Lab. IFA (1:1000). Used for invasion assays.
Antibody	Mouse monoclonal (16B12) anti-HA	BioLegend	Cat# 901533, RRID: AB_2565005	WB (1:1000)
Antibody	Rabbit polyclonal clone WU1614 anti-ALD	PMID: 16923803		Provided by L. David Sibley Lab. WB (1:10,000)
Antibody	Rabbit polyclonal anti-GAP45	other		Provided by Dominique Soldati-Favre Lab. WB (1:5000); IFA (1:5000)

Antibody	Peroxidase-AffiniPure polyclonal Goat Anti-Rabbit IgG (H+L)	Jackson ImmunoResearch Laboratories	Cat# 111-035-003, RRID:AB_2313567	WB (1/5000)
Antibody	Alexa Fluor 594 anti-rabbit	Life Technologies		IFA (1:1000)
Antibody	Alexa Fluor 488 anti-mouse	Life Technologies		IFA (1:1000)
Antibody	Alexa Fluor 488 anti-rabbit	Life Technologies		IFA (1:1000)
Antibody	Alexa Fluor 594 anti-mouse	Life Technologies		IFA (1:1000)
Antibody	IRDye 800CW Donkey anti-Guinea Pig IgG Secondary Antibody	LICOR	LICOR:926-32411	WB (1:10,000)
Antibody	IRDye 680RD Donkey anti-Guinea Pig IgG Secondary Antibody	LICOR	LICOR:926-68077	WB (1:10,000)
Antibody	IRDye 800CW Goat anti-Mouse IgG1-Specific Secondary Antibody	LICOR	LICOR:926-32350	WB (1:10,000)

Antibody	IRDye 680LT Goat anti-Mouse IgG Secondary Antibody	LICOR	LICOR:926-68020	WB (1:10,000)
Antibody	IRDye 800CW Goat anti-Rabbit IgG Secondary Antibody	LICOR	LICOR:926-32211	WB (1:10,000)
Antibody	IRDye 680LT Goat anti-Rabbit IgG Secondary Antibody	LICOR	LICOR:926-68021	WB (1:10,000)
Antibody	Alpaca clone 1B7 anti-CDPK1	PMID: 26305940	n/a	
Peptide, recombinant protein	IRDye 680RD Streptavidin	LICOR	LICOR:926-68079	WB (1:3,000)
Peptide, recombinant protein	Aerolysin	PMID: 26584919	n/a	
Peptide, recombinant protein	Sequencing Grade Modified Trypsin	Promega	Promega:V5113	
Chemical compound, drug	3-Indoleacetic acid (auxin)	Sigma Aldrich	Sigma Aldrich:I2886-5G	
Chemical compound, drug	Compound 1	PMID: 12455981	n/a	
Chemical compound, drug	Hoechst 33258	Santa Cruz	Santa Cruz:sc-394039	Egress assay (1:4000)
Chemical compound, drug	Hoechst 33342	Invitrogen	Invitrogen: H3570	IFA (1:20,000)

Chemical compound, drug	DAPI (4',6-Diamidino-2-Phenylindole, Dihydrochloride)	Invitrogen	Invitrogen: D1306	
Chemical compound, drug	Prolong Diamond	Thermo Fisher	Thermo Fisher:P36965	
Chemical compound, drug	zaprinast	Calbiochem	Calbiochem: 684500	
Chemical compound, drug	A23187	Calbiochem	Calbiochem: 100105	
Chemical compound, drug	Myristic acid	Tokyo Chemical Industry	Cat# M0476	
Chemical compound, drug	Alkyne-myristic acid (YnMyr)	Iris Biotech	Cat# RL-2055	
Chemical compound, drug	Trypsin cleavable capture reagent	PMID: 25807930; PMID: 32618271		This reagent was first reported as RTB in PMID: 25807930.
Chemical compound, drug	L-Proline for SILAC	Thermo Fisher Scientific	Thermo Fisher Scientific:88211	
Chemical compound, drug	Fetal Bovine Serum, dialyzed, US origin, One Shot™ format	Thermo Fisher Scientific	Thermo Fisher Scientific:A3382001	
Chemical compound, drug	DMEM for SILAC	Thermo Fisher Scientific	Thermo Fisher	

			Scientific:88364	
Chemical compound, drug	L-Arginine-HCl for SILAC	Thermo Fisher Scientific	Thermo Fisher Scientific:89989	
Chemical compound, drug	L-Lysine-2HCl for SILAC	Thermo Fisher Scientific	Thermo Fisher Scientific:89987	
Chemical compound, drug	L-Arginine-HCl, 13C6, 15N4 for SILAC	Thermo Fisher Scientific	Thermo Fisher Scientific:89990	
Chemical compound, drug	L-Lysine-2HCl, 13C6, 15N2 for SILAC	Thermo Fisher Scientific	Thermo Fisher Scientific:88209	
Chemical compound, drug	p-nitrobenzyl mesylate (PNBM)	Epitomics	Epitomics # 3700-1	
Chemical compound, drug	OXONE®, monopersulfate compound	Sigma Aldrich	Sigma Aldrich: 228036-5G	
Chemical compound, drug	N6-furfuryladenosine (kinetin)-5′-O-[3-thiotriphosphate] sodium salt (KTPγS)	Axxora	Axxora:BLG-F008-05	
Chemical compound, drug	Adenosine 5′-triphosphate disodium	Sigma Aldrich	Sigma Aldrich:A6419-1G	

	salt hydrate (ATP)			
Chemical compound, drug	Guanosine 5′-Triphosphate, Disodium Salt (GTP)	Calbiochem	Millipore:371701	
Chemical compound, drug	β-Casein from bovine milk	Sigma Aldrich	Sigma Aldrich:C6905	
Chemical compound, drug	Biotin	Sigma Aldrich	Sigma Aldrich: B4501-1G	
Chemical compound, drug	PP1 Analog III, 3-MB-PP1	Calbiochem	Sigma Aldrich:529582	
Commercial assay or kit	S-trap micro	Protifi	Protific:C02-micro-80	
Commercial assay or kit	Pierce Quantitative Fluorometric Peptide Assay	Thermo Fisher Scientific	Thermo Fisher Scientific:23290	
Commercial assay or kit	TMTpro™ 16plex Label Reagent Set	Thermo Fisher Scientific	Thermo Fisher Scientific:A44522	
Commercial assay or kit	EasyPep™ MS Sample Prep Kits - Maxi	Thermo Fisher Scientific	Thermo Fisher Scientific:A45734	
Commercial assay or kit	High-Select TiO2 Phosphopeptide Enrichment Kit	Thermo Fisher Scientific	Thermo Fisher Scientific:A32993	

Commercial assay or kit	High-Select™ Fe-NTA Phosphopeptide Enrichment Kit	Thermo Fisher Scientific	Thermo Fisher Scientific:A32992	
Commercial assay or kit	Pierce High pH Reversed-Phase Peptide Fractionation Kit	Thermo Fisher Scientific	Thermo Fisher Scientific:84868	
Commercial assay or kit	Dynabeads ® MyOne™ Streptavidin C1	Invitrogen	Cat# 65001	
Commercial assay or kit	Bio-Rad DC assay	Bio-Rad	Bio-Rad:5000116	
Commercial assay or kit	Sep-Pak C18 Plus Short Cartridge, 360 mg Sorbent per Cartridge, 55-105 µm	Waters	Waters:WAT020515	
Commercial assay or kit	SulfoLink™ Coupling Resin	Thermo Fisher Scientific	Thermo Fisher Scientific:20401	
Commercial assay or kit	Radiance Plus	Azure Biosystems	VWR:10147-298	

	Chemiluminescent Substrate			
Commercial assay or kit	Pierce™ Anti-HA Magnetic Beads	Thermo Scientific	Thermo Scientific:88836	
Commercial assay or kit	Pierce™ Streptavidin Magnetic Beads	Thermo Scientific	Thermo Scientific:88817	
Recombinant DNA reagent	All plasmids used in this study are listed in Supplementary file 10			
Sequence-based reagent	All primers and oligonucleotides used in this study are listed in Supplementary file 10			
Software, algorithm	Proteome Discoverer 4.2	Thermo Fisher		
Software, algorithm	MaxQuant (version 1.5.0.25 and 1.5.2.8)	PMID: 19029910	RRID:SCR_014485	Free software for searching of mass spectrometry acquisition files
Software, algorithm	Perseus (version 1.5.0.9)	PMID: 27348712	RRID:SCR_015753	Free software for processing of MaxQuant output files

Software, algorithm	Scaffold DIA	Proteome Software		
Software, algorithm	R version 4.0	R Foundation for Statistical Computing		
Software, algorithm	Prism 8	GraphPad		
Software, algorithm	Fiji	PMID: 22743772		
Software, algorithm	ilastik	PMID: 31570887	ilastik.org	
Software, algorithm	HHPRED	PMID: 29258817		
Software, algorithm	SnapGene	other	https://www.snapgene.com/	
Software, algorithm	ToxoDB	PMID: 18003657	ToxoDB.org	
other	DMEM, high glucose (media)	Life Technologies	Life Technologies:11965118	
other	HALT protease inhibitor	Thermo Fisher	Thermo Fisher:87786	Materials and Methods: lysis buffer
other	HALT protease and phosphatase inhibitor	Thermo Fisher	Thermo Fisher:PI78440	Materials and Methods: lysis buffer
other	Benzonase	Sigma Aldrich	Sigma Aldrich:E1014	Materials and Methods: lysis buffer

673

674 **Cell culture**

675 *T. gondii* parasites were grown in human foreskin fibroblasts (HFFs, ATCC SRC-1041)
676 maintained in DMEM (GIBCO 11965118) supplemented with 3% inactivated fetal calf serum and

677 10 µg/mL gentamicin (Thermo Fisher Scientific), referred to as media. When noted, DMEM was
678 supplemented with 10% inactivated fetal bovine serum (IFS) and 10 µg/mL gentamicin, referred
679 to as 10% IFS media. Parasites and HFFs were grown at 37°C/5% CO_2 unless indicated
680 otherwise.
681
682 **Parasite transfection and strain construction**

683 *Genetic background of parasite strains*
684 *T. gondii* RH strains were used as genetic backgrounds for this study. All strains contain the
685 *Δku80Δhxgprt* mutations to facilitate homologous recombination (Huynh and Carruthers, 2009).
686 TIR1 expresses the TIR1-FLAG ubiquitin ligase and the CAT enzyme conferring chloramphenicol
687 resistance (Brown et al., 2017).
688
689 *Transfection*
690 Parasites were pelleted at 1000 x *g* for 5 to 10 min and resuspended with Cytomix (10 mM KPO_4,
691 120 mM KCl, 0.15 mM $CaCl_2$, 5 mM $MgCl_2$, 25 mM HEPES, 2 mM EDTA, 2 mM ATP, and 5 mM
692 glutathione) and combined with DNA to a final volume of 400 µL. Parasites were electroporated
693 using an ECM 830 Square Wave electroporator (BTX) in 4 mm cuvettes with the following setting:
694 1.7 kV, 2 pulses, 176 µs pulse length, and 100 msec interval.
695
696 *Endogenous tagging of CDPK1 (CDPK1-AID)*
697 CDPK1-AID was generated in the study (Shortt et al., 2022). Briefly, *V5-mNG-mAID-Ty* was PCR
698 amplified from pBM050 (V5-TEV-mNG-mAID-Ty; GenBank: OM640006) to attach homology
699 arms to *TGGT1_301440* (*CDPK1*). DNA was co-transfected with a Cas9 expression plasmid
700 targeting *CDPK1* in TIR1 parasites. mNG-expressing parasites were isolated using FACS and
701 subcloned by limiting dilution. Tagging was confirmed by PCR, flow cytometry, and
702 immunoblotting.
703
704 *Endogenous tagging of CDPK1 (iKD) and complementation (cWT and cMut)*
705 Generating the inducible CDPK1 knock-down strain (iKD CDPK1). The pTUB1_YFP_mAID_3HA
706 vector was amplified by inverse PCR using primer pair P1/P2 to substitute the 3xHA tag
707 sequence for a Myc tag encoding sequence(Brown et al., 2017). A Cas9 expression plasmid
708 targeting the 3'UTR of *CDPK1* was generated by inverse PCR on pSag1_Cas9-U6_sgUPRT
709 using primers P3/P4(Shen et al., 2014). The sequence encoding *mAID-Myc-HXGPRT* was PCR
710 amplified using primer pair P5/P6 and co-transfected into TIR1 parasites with the Cas9 expression
711 plasmid. Recombinant parasites were selected 24 hrs post transfection by addition of
712 mycophenolic acid (MPA; 25 µg/mL) and xanthine (XAN; 50 µg/mL) to culture medium. Lines
713 were cloned, and successful 5' and 3' integration of the *mAID-Myc-HXGPRT* cassette was
714 confirmed using primer pairs P30/P31 and P32/P33. Absence of WT was confirmed using primers
715 P34/P35.
716
717 Generating the cWT and cMut CDPK1 complementation strain. To generate the
718 complementation construct, pUPRT_CDPK1_ HA_T2A_GFP (GenBank: Pending), the *CDPK1*

719 5'UTR was amplified from genomic DNA using primer pair P7/P8. Recodonized *CDPK1* cDNA-
720 HA sequence was synthesized (GeneArt strings, Life Technologies) and amplified with
721 appropriate overhangs using primers P9/P10. Sequence encoding T2A-GFP was amplified from
722 an in-house unpublished plasmid using primer pair P11/P12. The three resulting fragments were
723 Gibson cloned into the PacI-linearized pUPRT_HA vector(Reese et al., 2011). To generate the
724 complementation construct, pUPRT_CDPK1(G2A)_HA_T2A_mCherry (GenBank: Pending), the
725 CDPK1 5'UTR was amplified from genomic DNA using primer pair P13/P8. Recodonized *CDPK1-*
726 *HA* was amplified from pUPRT_CDPK1_ HA_T2A_GFP with appropriate overhangs using
727 primers P14/P15. Primers P13/P15 were used to introduce a G2A point mutation within *CDPK1*.
728 Sequence encoding *T2A-mCherry* was amplified from an in-house unpublished plasmid using
729 primer pair P11/P16. The three resulting PCR amplicons were Gibson cloned into the PacI-
730 linearized pUPRT_HA vector. Complementation plasmids were linearized with AclI and
731 individually co-transfected with the Cas9 expression plasmid targeting the *UPRT* locus.
732 Transgenic parasites were subjected to 5'-fluo-2'-deoxyuridine (FUDR) selection (5 μM) 24 hrs
733 post transfection. Resistant parasites were cloned, and successful 5' and 3' integration was
734 confirmed using primer pairs P36/P37 and P38/P39, respectively. Disruption of the endogenous
735 *UPRT* locus was confirmed using primer pair P40/P41.
736
737 *Endogenous tagging of genes*
738 Genes were endogenously tagged using the previously described high-throughput tagging (HiT)
739 strategy (Smith et al., 2022). Cutting units specific to each gene were purchased as gene
740 fragments (IDT gBlocks; P22 and P23) and integrated with the following empty HiT vector
741 backbones via Gibson assembly: pALH086 (V5-mAID-HA; GenBank: ON312869), pALH047 (V5-
742 3HA; GenBank: ON312868), and pALH173 (TurboID-Ty; GenBank: Pending).
743
744 Between 30 and 50 μg of each vector was linearized with BsaI and co-transfected with 50 μg of
745 the pSS014 Cas9 expression plasmid (GenBank: OM640002). Vectors targeting *TGGT1_289100*
746 (*HOOK*) were transfected into TIR1 or CDPK1-AID. Vectors targeting *TGGT1_264050* (*FTS*) were
747 transfected into TIR1. Parasites underwent drug selection for approximately 1 week in 10% IFS
748 media with 3 μM pyrimethamine or 25 μg/mL mycophenolic acid and 50 μg/mL xanthine,
749 followed by subcloning into 96-well plates. Single clones were screened for tag expression by
750 PCR, immunofluorescence, or immunoblot. PCR validation was performed using the primers
751 P44/P45 (FTS-AID) and P46/P47 (FTS-TurboID).
752
753 *Endogenous tagging of HOOK N terminus*
754 AID-HOOK N-terminal tagging was generated by PCR amplifying the gene fragment encoding
755 the *HA-mAID* with homology arms to *HOOK* (IDT gBlock; P17) using the primers P18/19. A
756 sgRNA targeting *HOOK* was assembled into the pSS013 Cas9 expression plasmid (GenBank:
757 OM640003) using the primers P20/P21. 10 μg of the PCR product was transfected with 50 μg of
758 the Cas9 expression plasmid. Parasites were subcloned into 96-well plates. Single clones were
759 screened using PCR primers P42/P43 and validated by immunofluorescence and immunoblot.
760
761 *TIR1/pMIC2-mNeonGreen-TurboID-Ty*

762 *pMIC2-mNG-TurboID-Ty* was amplified with primers P24/P25 from pALH184 (pMIC2-mNG-
763 TurboID-Ty-3'DHFR; GenBank: Pending) with homology arms to the 5′ and 3′ ends of a defined,
764 neutral genomic locus (Markus et al., 2019). Amplified DNA was co-transfected with the Cas9
765 expression plasmid targeting the neutral locus (pBM041; GenBank: MN019116). mNeonGreen-
766 expressing parasites were isolated by FACS and subcloned in 96-well plates. Expression was
767 confirmed by fluorescence.
768
769 *Endogenous tagging of CLAMP*
770 *mNeonGreen* DNA was amplified using PCR from pGL015 (V5-mNG-mAID-Ty; GenBank:
771 OM640005) with homology arms targeting the C terminus of *TGGT1_265790* (*CLAMP*) using the
772 primers P26/P27. A sgRNA targeting *CLAMP* was assembled into the pSS013 Cas9 expression
773 plasmid (GenBank: OM640003) using the primers P28/P29. Between 5 and 10 µg of
774 *mNeonGreen* DNA was co-transfected with 50 µg of the Cas9 expression plasmid targeting
775 *CLAMP* into TIR1 and AID-HOOK. Parasites were grown in 10% IFS media until lysing the HFF
776 monolayer, followed by FACS-mediated isolation of mNeonGreen expressing parasites and
777 subcloning into 96-well plates. Single clones were screened for mNeonGreen expression by PCR
778 using primers P48/P49 and live microscopy.
779
780 **Sub-minute phosphoproteomics**
781 *Parasite harvest and treatment*
782 *T. gondii* tachyzoites from the RH strain CDPK1-AID were used to infect nine 15 cm dishes. 3.75
783 x 10^7 parasites were used to infect each dish in 20 mL of media. Approximately 24 hrs later, the
784 media of eight dishes was replaced with 15 mL of media containing 1 µM of compound 1 to
785 block egress and synchronize parasites by inhibiting PKG (Donald et al., 2006; Hopp et al., 2012;
786 Taylor et al., 2010). The media of the ninth dish was replaced with media containing DMSO. On
787 day 2, parasites were harvested when the monolayer of HFFs in the DMSO dish were
788 approximately 80% lysed. The eight dishes treated with compound 1 were washed once with 10
789 mL of warm 1X PBS, once with 30 mL of warm 1X PBS, and incubated with 10 mL of warm
790 FluoroBrite (Fluorobrite DMEM A1896701, 4 mM glutamine, 10 µg/mL gentamicin) for 10 min at
791 37°C. Infected HFFs were scraped and passed through a 27G needle to mechanically liberate
792 parasites and passed through a 5 µm filter. Parasites were pelleted at 1000 x *g* at 4°C for 10 min,
793 resuspended in 10 mL of FluoroBrite and a 1:250 dilution was used to count parasites
794 (approximately 2.25 x 10^9 total parasites). Parasites were pelleted at 1000 x *g* at 4°C for 7 min
795 and resuspended in 2 mL of FluoroBrite. 1 mL of parasites were diluted into a total volume of 40
796 mL of FluoroBrite containing either 500 µM of auxin or vehicle of 1X PBS and incubated at 37°C
797 for 3.5 hrs. 50 µL of auxin- or vehicle-treated parasites and untagged TIR1 parasites were
798 analyzed by flow cytometry (Miltenyi MACSQuant VYB) to detect mNeonGreen fluorescence.
799 After confirming depletion of CDPK1, parasites were pelleted at 1000 x *g* for 10 min at room
800 temperature and resuspended in 210 µL of 500 µM auxin or vehicle of PBS diluted in FluoroBrite.
801 To obtain a time course, the 0 sec time point was first collected by mixing 16 µL of parasites
802 with 4 µL of 5X DMSO (0.5% DMSO in FluoroBrite) and immediately lysed with 20 µL of 2X Lysis
803 Buffer (10% SDS, 100 mM TEAB pH 7.5, 2 mM $MgCl_2$, and 2X HALT protease and phosphatase

804 inhibitors). To obtain the 9, 30, and 300 sec time points, 80 µL of parasites in 1.5 mL tubes were
805 incubated in a ThermoMixer (Eppendorf) set to 37°C. The parasites were stimulated by adding
806 20 µL of warmed 5X zaprinast (500 µM zaprinast in FluoroBrite) or a vehicle of 5X DMSO. At each
807 time point, 20 µL of stimulated parasites were transferred directly into 20 µL of 2X Lysis Buffer
808 to quench the reaction. Complete time courses were collected sequentially in the following order:
809 auxin-treated stimulated with zaprinast, vehicle-treated stimulated with zaprinast, auxin-treated
810 stimulated with DMSO, and vehicle-treated stimulated with DMSO. Lysates were treated with
811 benzonase at a final concentration of 5 units/µL to remove DNA and were immediately subjected
812 to protein cleanup and digestion.
813
814 *Protein cleanup and digestion*
815 Proteins were prepared for mass spectrometry using a modified version of the S-trap protocol
816 (Protifi). Proteins in lysates were reduced with 5 mM TCEP for 10 min at 55°C and alkylated with
817 15 mM MMTS for 10 min at room temperature. The lysates were acidified to a final concentration
818 of 1.2% v/v phosphoric acid. A 6X volume of S-trap binding buffer (90% methanol, 100 mM
819 TEAB, pH 7.55) was mixed to each sample to precipitate proteins. The solution was loaded onto
820 S-trap micro columns (Protifi) and spun at 4,000 x *g* for 1 min until all the solution had passed
821 through the column. The columns were washed four times with 150 µL of S-trap binding buffer
822 and centrifuged at 4,000 x *g* for 1 min between each wash. Proteins were digested on-column
823 with 0.75 µg of trypsin (Promega) in 50 mM TEAB pH 8.5 overnight at 37°C in a humidified
824 incubator. Digested peptides were eluted in three steps at 4,000 x *g* for 1 min: 40 µL of 50 mM
825 TEAB, 40 µL of 0.2% formic acid, and 35 µL of 50% acetonitrile/0.2% formic acid. The peptide
826 concentrations of eluted peptides were quantified using the Pierce Fluorometric Peptide Assay
827 (Thermo Fisher Scientific) according to manufacturer's instructions. The remaining samples were
828 frozen in liquid nitrogen and lyophilized.
829
830 *TMTpro labeling*
831 Lyophilized peptides were resuspended in 100 mM TEAB pH 8.5 to peptide concentrations of
832 1.6 µg/µL. TMTpro reagents (Thermo Fisher Scientific; A44522 LOT# VI306829) were
833 resuspended in acetonitrile to 25 µg/µL. 80 µg of peptides in 50 µL were combined with 250 µg
834 of TMTpro reagent in 10 µL to achieve approximately a 3:1 label:peptide weight/weight ratio
835 (Zecha et al., 2019). The TMTpro labels were assigned to minimize reporter ion interference and
836 inter batch variability in the following scheme: Replicate 1 auxin: 0, 9, 30, 300 sec (126, 128C
837 130C, 132C); Replicate 1 vehicle: 0, 9, 30, 300 sec (127N, 129N, 131N, 133N); Replicate 2 auxin:
838 0, 9, 30, 300 sec (127C, 129C, 131C, 133C); Replicate 2 vehicle: 0, 9, 30, 300 sec (128N, 130N,
839 132N, 134) (Brenes et al., 2019). The zaprinast and DMSO samples were incubated for 1 hr at
840 room temperature shaking at 400 rpm. Unreacted TMTpro reagent was quenched with
841 hydroxylamine at a final concentration of 0.2%. The samples were pooled, acidified to 3% with
842 formic acid, and were processed using the EasyPep Maxi Sample Prep column (Thermo Fisher
843 Scientific) according to the manufacturer's instructions. 5% of the eluate volume was reserved
844 as the unenriched proteome sample. The remaining eluted peptides were frozen in liquid nitrogen
845 and lyophilized.
846

847 *Phosphopeptide enrichment*
848 Phosphopeptides were enriched using the Sequential enrichment from Metal Oxide Affinity
849 Chromatography (SMOAC) protocol according to manufacturer instructions (Tsai et al., 2014).
850 First, the High-Select TiO_2 Phosphopeptide Enrichment Kit (Thermo Fisher Scientific) was used
851 to enrich phosphopeptides from lyophilized TMTpro-labeled samples. The flow-through and
852 contents of the first wash were pooled, frozen in liquid nitrogen, and lyophilized, along with the
853 eluate. Second, the High-Select Fe-NTA Phosphopeptide Enrichment Kit (Thermo Fisher
854 Scientific) was used to enrich phosphopeptides from the pooled flow-through and first wash
855 from the previous enrichment. The eluted phosphopeptides were frozen in liquid nitrogen and
856 lyophilized.
857
858 *Fractionation*
859 The enriched and unenriched samples were fractionated with the Pierce High pH Reversed-
860 Phase Peptide Fractionation Kit (Thermo Fisher Scientific) according to manufacturer
861 instructions for TMT-labeled peptides. The acetonitrile wash was omitted for enriched samples
862 to prevent loss of phosphopeptides. The eluted peptides from the High-Select TiO_2
863 Phosphopeptide Enrichment and High-Select Fe-NTA Phosphopeptide Enrichment were pooled
864 prior to fractionation. 100 µg of unenriched samples were fractionated. 8 fractions were collected
865 for each TMTpro set: zaprinast phosphoproteome (enriched) [1], zaprinast proteome
866 (unenriched) [2], DMSO phosphoproteome (enriched) [3], and DMSO proteome (unenriched) [4].
867 The fractions were frozen in liquid nitrogen and lyophilized.
868
869 *MS data acquisition*
870 Lyophilized peptides were resuspended in approximately 15 µL (enriched) or 50 µL (unenriched)
871 of 0.1% formic acid and were analyzed on an Exploris 480 Orbitrap mass spectrometer equipped
872 with a FAIMS Pro source (Bekker-Jensen et al., 2020) connected to an EASY-nLC 1200
873 chromatography system using 0.1% formic acid as Buffer A and 80% acetonitrile/0.1% formic
874 acid as Buffer B. Peptides were loaded onto a heated analytical column (ES900, Thermo,
875 PepMap RSLC C18 3 µm, 100 Å, 75 µm x 15 cm, 40°C) via trap column (164946, Thermo,
876 Acclaim PepMap C18 3 µm, 100 Å, 75 µm x 20 mm nanoViper). Peptides were separated at 300
877 nL/min. Enriched samples were separated on a gradient of 5–20% B for 110 min, 20–28% B for
878 10 min, 28–95% B for 10 min, 95% B for 10 min, 95–2% B for 2 min, 2% B for 2 min, 2–98% B
879 for 2 min, 98% B for 2 min, 98–2% B for 2 min, and 2% B for 2 min. Unenriched samples were
880 separated on a gradient of 5–25% B for 110 min, 25–40% B for 10 min, 40–95% B for 10 min,
881 95% B for 10 min, 95–2% B for 2 min, 2% B for 2 min, 2–98% B for 2 min, 98% B for 2 min, 98–
882 2% B for 2 min, and 2% B for 2 min. The orbitrap and FAIMS were operated in positive ion mode
883 with a positive ion voltage of 1800V; with an ion transfer tube temperature of 270°C; using a
884 standard FAIMS resolution and compensation voltage of -50 and -65V, an inner electrode
885 temperature of 100°C and outer electrode temperature 80°C with 4.5 mL/min carrier gas. DDA
886 analysis was performed with a cycle time of 1.5 sec. Full scan spectra were acquired in profile
887 mode at a resolution of 60,000, with a scan range of 400–1400 m/z, 300% AGC target, maximum
888 injection time of 50 msec, intensity threshold of 5×10^4, 2–5 charge state, dynamic exclusion of
889 30 sec, mass tolerance of 10 ppm, purity threshold of 70%, and purity window of 0.7. MS2

890 spectra were generated with a HCD collision energy of 32 at a resolution of 45,000 using
891 TurboTMT settings with a first mass at 110 m/z, an isolation window of 0.7 m/z, 200% AGC
892 target, and maximum injection time of 120 msec.
893
894 *Phosphoproteomic time course analysis*
895 Raw files were analyzed in Proteome Discoverer 2.4 (Thermo Fisher Scientific) to generate peak
896 lists and protein and peptide IDs using Sequest HT (Thermo Fisher Scientific) and the ToxoDB
897 release 49 GT1 protein database. The maximum missed cleavage sites for trypsin was limited to
898 2. Precursor and fragment mass tolerances were 10 ppm and 0.02 Da, respectively. The
899 following modifications were included in the search: dynamic oxidation (+15.995 Da; M), dynamic
900 phosphorylation (+79.966 Da; S,T,Y), dynamic acetylation (+42.011 Da; N-terminus), static
901 TMTpro (+304.207 Da; any N-terminus), static TMTpro (+304.207 Da; K), and static methylthio
902 (+45.988 Da; C). TMTpro 16plex isotope correction values were accounted for (Thermo Fisher
903 Scientific; A44522 LOT# VI306829). Peptides identified in each sample were filtered by
904 Percolator to achieve a maximum FDR of 0.01 (Käll et al., 2008a, 2008b, 2007). Site localization
905 scores were generated using ptmRS, with phosphoRS and use of diagnostic ions set to true
906 (Taus et al., 2011). Reporter ion quantification used an integration tolerance of 20 ppm on the
907 most confident centroid. For reporter ion quantification, unique peptides were quantified using
908 a co-isolation threshold of 50, and average reporter signal-to-noise ratio of 10. Abundances were
909 normalized on the total protein amount. Protein level and peptide level ratios were generated for
910 each time point relative to 0 sec vehicle-treated parasites stimulated with DMSO.
911
912 Exported peptide and protein abundance files from Proteome Discoverer 2.4 were loaded into R
913 (version 4.1.1). To determine CDPK1-dependent phosphorylation, $\log_2$ ratios for peptide
914 abundances in DMSO and zaprinast-treated samples derived from Proteome Discoverer were
915 used. Only phosphorylated peptides quantified across all time points were used for analysis.
916 Area under the curve (AUC) values were calculated for individual peptides undergoing vehicle
917 (AUC_{veh}) and auxin (AUC_{auxin}) treatment using trapezoidal integration. AUC differences (AUC_{diff})
918 were calculated by taking the difference between AUC_{veh} and AUC_{auxin} values. The distribution of
919 zaprinast AUC_{diff} values were tested against a null distribution derived from the DMSO AUC_{diff}
920 values to calculate *z*-scores and *p*-values using a two-tailed *t*-test. Replicates 1 and 2 were
921 analyzed independently and phosphopeptides with p-values < 0.05 across both replicates were
922 determined to be CDPK1-dependent (Group A). Peptides exhibiting phosphorylation
923 independent of CDPK1 (Group B, C, and D) were determined similarly, but compared the
924 distribution of zaprinast $AUC_{vehicle}$ values to a null distribution of DMSO $AUC_{vehicle}$ values and
925 excluded phosphopeptides already determined to be CDPK1-dependent. CDPK1-independent
926 phosphopeptides were clustered into Groups B, C, and D using projection-based clustering
927 (Thrun and Ultsch, 2021).
928
929 **Gene ontology enrichment**
930 Gene ontology terms were obtained for all genes present in the enriched zaprinast
931 phosphoproteome from ToxoDB.org (Computed GO function and GO function IDs). Gene

932 ontology IDs within each group of zaprinast-dependent genes (Groups A-D) were tested for
933 enrichment against the entire enriched zaprinast phosphoproteome. Enrichment p values were
934 generated using a hypergeometric test. Enrichment ratios were calculated by dividing the gene
935 ratio (overlap/signatures) by the relative frequency of gene sets (gene sets/background). Only
936 GO IDs with significant enrichment and an overlap of 2 were plotted. Thiophosphorylation
937 enrichment was performed similarly.
938
939 **Metabolic tagging, click reaction, pull down, and Western blotting**

940 *Metabolic tagging and cell lysis*
941 Upon infection of HFF monolayers the medium was removed and replaced by fresh culture media
942 supplemented with 25 μM YnMyr (Iris Biotech) or Myr (Tokyo Chemical Industry). The parasites
943 were then incubated for 16 hrs, washed with PBS (2x) and lysed on ice using a lysis buffer (PBS,
944 0.1% SDS, 1% Triton X-100, EDTA-free complete protease inhibitor (Roche Diagnostics)).
945 Lysates were kept on ice for 20 min and centrifuged at 17,000 × *g* for 20 min to remove insoluble
946 material. Supernatants were collected and protein concentration was determined using a BCA
947 protein assay kit (Pierce).
948
949 *Click reaction and pull down*
950 Lysates were thawed on ice. Proteins (100–300 μg) were taken and diluted to 1 mg/mL using the
951 lysis buffer. A click mixture was prepared by adding reagents in the following order and by
952 vortexing between the addition of each reagent: a capture reagent (stock solution 10 mM in
953 water, final concentration 0.1 mM), $CuSO_4$ (stock solution 50 mM in water, final concentration 1
954 mM), TCEP (stock solution 50 mM in water, final concentration 1 mM), TBTA (stock solution 10
955 mM in DMSO, final concentration 0.1 mM) (Heal et al., 2011). Capture reagent used herein was
956 the Trypsin cleavable reagents (Broncel et al., 2020). Following the addition of the click mixture
957 the samples were vortexed (room temperature, 1 hr), and the reaction was stopped by addition
958 of EDTA (final concentration 10 mM). Subsequently, proteins were precipitated
959 (chloroform/methanol, 0.25:1, relative to the sample volume), the precipitates isolated by
960 centrifugation (17,000 x *g*, 10 min), washed with methanol (1 x 400 μL) and air dried (10 min). The
961 pellets were then resuspended (final concentration 1 mg/mL, PBS, 0.4 % SDS) and the
962 precipitation step was repeated to remove excess of the capture reagent. Next, samples were
963 added to 15 μL of pre-washed (0.2 % SDS in PBS (3 x 500 μL)) Dynabeads® MyOneTM
964 Streptavidin C1 (Invitrogen) and gently vortexed for 90 min. The supernatant was removed, and
965 the beads were washed with 0.2 % SDS in PBS (3 x 500 μL).
966
967 *SDS-PAGE and Western blotting*
968 Beads were supplemented with 2% SDS in PBS (20 μL) and 4x SLB (Invitrogen), boiled (95°C,
969 10 min), centrifuged (1,000 x *g*, 2 min) and loaded on 10% or 4–20% SDS-PAGE gel (Bio-Rad).
970 Following electrophoresis (60 min, 160V), gels were briefly washed with water and proteins were
971 transferred (25 V, 1.3 A, 7 min) onto nitrocellulose membranes (Bio-Rad) using Bio-Rad Trans
972 Blot Turbo Transfer system. After brief wash with PBS-T (PBS, 0.1% Tween-20) membranes
973 were blocked (5% milk, TBS-T, 1h) and incubated with primary antibodies (5% milk, TBS-T,

overnight, 4°C) at the following dilutions: rat anti-HA (1:1000; Roche Diagnostics), mouse anti-Myc (1:1000; Millipore), rabbit anti-Gra29 (1:1000; Moritz Treeck Lab), rabbit anti-SFP1 (1:1000; Moritz Treeck Lab), mouse anti-T. gondii [TP3] (1:1000; Abcam), mouse anti-CDPK1 (1:3000; John Boothroyd Lab), rabbit anti-SAG1 (1:10,000; John Boothroyd Lab), rabbit anti-GAP45 (1:1000; Peter Bradley Lab), mouse anti-GFP (1:1000, Roche Diagnostics) and rabbit anti-mCherry (1:1000, Abcam). Following washing (TBS-T, 3x) membranes were incubated with IR dye-conjugated secondary antibodies (1:10,000, 5% milk, TBS-T, 1 hr) and after a final washing step imaged on a LiCOR Odyssey imaging system (LI-COR Biosciences).

MS detection of myristoylated CDPK1

Mass spectrometry proteomics methods and data for myristoylated CDPK1 are available from the ProteomeXchange Consortium via the PRIDE partner repository (ID PXD019677) and the associated publication (Broncel et al., 2020).

Depletion of mAID tagged CDPK1 (iKD)

Parasites were treated with 500 µM auxin or equivalent volume of vehicle (ethanol) for at least 2 hrs prior to Western blot analysis.

Subcellular fractionation

RH Δ*ku80*Δ*hxgprt* YFP expressing parasites were metabolically tagged with 25 µM Myr or YnMyr for 16 hrs. Following a PBS wash, the parasites were syringe lysed in Endo buffer (44.7 mM K_2SO_4, 10 mM $MgSO_4$, 106 mM sucrose, 5 mM glucose, 20 mM Tris–H_2SO_4, 3.5 mg/mL BSA, pH 8.2) and collected by centrifugation (512 x *g*, 10 min). The parasites were then lysed in 300 µL of cold hypotonic buffer (10 mM HEPES, pH 7.5) supplemented with protease inhibitors (Roche), passed through 25G needle (5x) and left on ice for 40 min. Next, lysates were pelleted by centrifugation (16,000 x *g*, 20 min, 4 °C) and the resulting supernatant was subjected to an additional high speed (100,000 x *g*, 1 h, 4 °C) centrifugation step. To avoid the loss of the high-speed pellet, only half of the supernatant was removed at this point. Each fraction was then taken up in 0.4% (final) SDS HEPES, clicked to a capture reagent and pulled down as described above. Myristoylation-dependent partitioning was revealed by SDS-PAGE and Western blotting.

Myristoylation-dependent fractionation for CDPK1 complemented WT and Mut lines: parasites were seeded 24 hrs prior experiment. Following a PBS wash, the parasites were syringe lysed in Endo buffer (44.7 mM K_2SO_4, 10 mM $MgSO_4$, 106 mM sucrose, 5 mM glucose, 20 mM Tris–H_2SO_4, 3.5 mg/mL BSA, pH 8.2) and collected by centrifugation (512 x *g*, 10 min). The parasites were then lysed in 300 µL of cold hypotonic buffer (10 mM HEPES, pH 7.5) supplemented with protease inhibitors (Roche), passed through 25G needle (5x) and left on ice for 40 min. Next, lysates were pelleted by centrifugation (100,000 x *g*, 1 hr, 4 °C), the supernatant was removed, and cytosolic proteins precipitated with methanol/chloroform. Proteins from the pellet and supernatant fractions were dissolved in 2% (final) SDS PBS and myristoylation-dependent partitioning was revealed by SDS-PAGE and Western blotting.

1014 **Immunoprecipitation of cWT and cMUT CDPK1**

1015 *Parasite harvest*
1016 cWT, cMUT, and TIR1 (untagged) parasites were infected onto confluent HFFs in 15 cm dishes.
1017 At 1-day post-infection (dpi), 50 µM auxin or vehicle was added to deplete endogenous mAID-
1018 tagged CDPK1 and 1 µM compound 1 was added to block egress until parasites were ready to
1019 harvest. At 2 dpi, infected HFFs were washed twice with PBS to wash out drugs. Parasites were
1020 mechanically released in Endo buffer with a 27G needle, passed through a 5 µm filter, and spun
1021 at 1000 x *g* for 10 min. Parasite pellets were resuspended in a cold hypotonic buffer with 1X
1022 HALT protease inhibitors to parasite concentrations of 1.1 x 10^9 tg/mL, passed through a 27G
1023 needle five times, and incubated on ice for 1 hr to complete hypotonic lysis. The samples were
1024 spun at 1000 x *g* for 5 min to pellet unlysed parasites and the supernatant was saved. NaCl was
1025 added to a final concentration of 150 mM and this was used as the immunoprecipitation input.
1026
1027 *Immunoprecipitation*
1028 25 µL of anti-HA magnetic beads (Thermo) were used per condition. Beads were washed twice
1029 with a wash buffer (10 mM HEPES, 150 mM NaCl, pH 7.5). To begin pulldown, parasite lysate
1030 was used to resuspend washed beads and incubated for 1 hr rotating at room temperature.
1031 Beads were washed four times with a wash buffer. Proteins were eluted by resuspending beads
1032 in 20 µL of 1X S-trap sample buffer (5% SDS, 50 mM TEAB, pH 7.5) and incubated at 70°C for
1033 10 min. The eluate was collected for MS sample processing and analysis. Results are
1034 representative of two independent experiments.
1035
1036 *Protein cleanup and digestion*
1037 Proteins were prepared for mass spectrometry as described above in "Sub-minute
1038 phosphoproteomics - Protein cleanup and digestion". Eluted peptides were frozen in liquid
1039 nitrogen, lyophilized, and stored at -80°C until MS analysis.
1040
1041 *MS data acquisition*
1042 Lyophilized peptides were resuspended in 20 µL of 0.1% formic acid and were analyzed on an
1043 Exploris 480 Orbitrap mass spectrometer equipped with a FAIMS Pro source (Bekker-Jensen et
1044 al., 2020) connected to an EASY-nLC chromatography system using 0.1% formic acid as Buffer
1045 A and 80% acetonitrile/0.1% formic acid as Buffer B. Peptides were separated at 300 nL/min on
1046 a gradient of 1–6% B for 1 min, 6–21% B for 41 min and 30 sec, 21–36% B for 20 min and 45
1047 sec, 36–50% B for 10 min and 15 sec, 100% B for 14 min and 30 sec, 100–2% B for 3 min, 2%
1048 B for 3 min, 2–98% B for 3 min, and 98% B for 3 min. The orbitrap and FAIMS were operated in
1049 positive ion mode with a positive ion voltage of 1800V; with an ion transfer tube temperature of
1050 270°C; using a standard FAIMS resolution and an inner and outer electrode temperature of
1051 100°C with 4.5 mL/min carrier gas. Samples were analyzed twice in DIA mode with a
1052 compensation mode of -50 and -65V. Full scan spectra were acquired in profile mode at a
1053 resolution of 120,000, with a scan range of 400–1000 m/z, 300% AGC target, and auto mode for
1054 maximum injection time. MS2 spectra for the DIA scan were generated with a isolation window
1055 of 20 m/z with a 0 m/z window overlap, 30 scan events, a HCD collision energy of 30 at a

1056 resolution of 30,000, first mass at 200 m/z, precursor mass range of 400–1000 m/z, and a
1057 standard AGC target and automatically determined maximum injection time.
1058
1059 *Immunoprecipitation data analysis*
1060 DIA-MS samples were analyzed using Scaffold DIA (2.0.0). DIA-MS data files were converted to
1061 mzML format using ProteoWizard (3.0.19254) (Chambers et al., 2012). Analytic samples were
1062 aligned based on retention times and individually searched against
1063 dku80_FAIMS_DIA_90min_autoIT.blib with a peptide mass tolerance of 10 ppm and a fragment
1064 mass tolerance of 0.02 Da. The ToxoDB release 46 GT1 protein database was used for protein
1065 identification. The following modifications were included in the search: dynamic oxidation
1066 (+15.995 Da; M), dynamic phosphorylation (+79.966 Da; S,T,Y), and static methylthio (+45.988
1067 Da; C). The digestion enzyme was trypsin with a maximum of 2 missed cleavage sites allowed.
1068 Only peptides with charges in the range of 2 to 3 and length in the range 6 to 30 were considered.
1069 Peptides identified in each sample were filtered by Percolator to achieve a maximum FDR of
1070 0.01 (Käll et al., 2008a, 2008b, 2007). Individual search results were combined, and peptide
1071 identifications were assigned posterior error probabilities and filtered to an FDR threshold of 0.01
1072 by Percolator. Peptide quantification was performed by Encyclopedia (0.9.2). For each peptide,
1073 the 5 highest quality fragment ions were selected for quantification. Proteins that contained
1074 similar peptides and could not be differentiated based on MS/MS analysis were grouped to
1075 satisfy the principles of parsimony. Protein groups were thresholded to achieve a protein FDR
1076 less than 1%. Significance values were derived from *t*-tests across two replicates and adjusted
1077 with Benjamini-Hochberg correction with an FDR of 0.05. Exported protein abundance files from
1078 Scaffold DIA were loaded into R (version 4.1.1).
1079
1080 **Thiophosphorylation of CDPK1 substrates**
1081 *Parasite harvest and treatment*
1082 *T. gondii* tachyzoites from the RH strain ($CDPK1^G$ and $CDPK1^M$) were passaged twice across 4
1083 days in SILAC media in T12.5 flasks. $CDPK1^G$ parasites were grown in "heavy" SILAC media
1084 (DMEM 88364, 10% dialyzed FBS, 0.1 mg/mL $^{13}C^{15}N$ L-arginine, 0.1 mg/mL $^{13}C^{15}N$ L-lysine) and
1085 $CDPK1^M$ parasites were grown in "light" SILAC media (DMEM 88364, 10% dialyzed FBS, 0.1
1086 mg/mL L-Arginine, 0.1 mg/mL L-Lysine). On day 4, confluent HFFs in 15 cm dishes were infected
1087 with $CDPK1^G$ and $CDPK1^M$ parasites in SILAC media. On day 6, extracellular parasites were
1088 harvested by filtering through a 5 µm filter and pelleted at 1000 x *g* for 7 min at 4°C. Parasites
1089 were washed once in 1X intracellular buffer (ICB) (137 mM KCl, 5 mM NaCl, 20 mM HEPES, 10
1090 mM $MgCl_2$, pH 7.5 KOH) and then resuspended in 400 µL of 1X ICB. Parasites were semi-
1091 permeabilized after the addition of 400 µL of 6 µg/mL aerolysin diluted in 1X ICB and incubated
1092 at 37°C for 10 min. After semi-permeabilization, 400 µL of 4X Ca^{2+} solution (16 mM CaEGTA, 100
1093 ng/mL 1B7 nanobody in 1X ICB) followed by 400 µL of 4X ATP solution (4 mM GTP, 0.4 mM
1094 ATP, 0.2 mM KTPγS, 1X HALT protease and phosphatase inhibitor in 1X ICB). The kinase
1095 reaction was initiated by incubating parasites at 30°C for 5 min. Parasites were pelleted at 1000
1096 x *g* at 4°C for 10 min. Parasite pellets were resuspended in 250 µL of 1X lysis buffer (10% TritonX-
1097 100, 1X HALT protease and phosphatase inhibitor, 10 mM K_2EGTA in 1X ICB).

1098

1099 *Protein quantification and thiophosphorylation immunoblotting*

1100 Proteins in lysates were quantified using DC assay (BioRad) utilizing BSA as a protein standard
1101 and a diluent (150 mM NaCl, 20 mM Tris pH 7.6) to prepare standard curves and dilution series.
1102 Thiophosphorylation was verified using immunoblot by first incubating 3 µL of sample with p-
1103 nitrobenzyl mesylate diluted in 1X ICB at a final concentration at 2 mM for 2 hrs at room
1104 temperature. 5X Laemmli sample buffer was added (see "Immunoblotting" for recipe) and
1105 samples were boiled for 10 min. Samples were resolved on a home-made polyacrylamide gel
1106 (5% stacking, 15% resolving, 15-well, 0.75 mm) and transferred overnight at 4°C. Nitrocellulose
1107 membranes were blocked with 5% milk in TBS-T for 1 hr. Primary antibody incubations were
1108 performed with an anti-thiophosphate ester antibody (rabbit 51-8; 1:5000) and anti-tubulin
1109 (mouse 12G10; 1:2000) for 1 hr at room temperature. Secondary incubations were performed
1110 with LI-COR antibodies (rabbit 680, mouse 800; 1:10,000) for 1 hr at room temperature. Imaging
1111 was performed using a LI-COR Odyssey.

1112

1113 *Protein cleanup and digestion*

1114 Proteins were precipitated using methanol chloroform extraction. For 250 µL of lysate, 800 µL
1115 methanol and 200 µL of chloroform was added, followed by vortexing. After adding 600 µL of
1116 water, the sample was vortexed and centrifuged at max speed for 5 min at 4°C. After removing
1117 the supernatant without disrupting the precipitate, 375 µL of methanol was added and vortexed.
1118 Samples were centrifuged at max speed for 15 min at 4°C. The protein pellet was allowed to air
1119 dry after removing the supernatant. Dried protein pellets were resuspended in 200 µL of 8M urea.
1120 1 mg of protein (determined from protein quantification; see above) from $CDPK1^{G}$ and $CDPK1^{M}$
1121 parasites were pooled for a total of 2 mg of protein. To digest protein, 5X volume of 1X Trypsin
1122 Digest Buffer (100 mM ammonium acetate pH 8.9, 1mM $CaCl_2$, 2 mM TCEP) was added to the
1123 sample followed by 40 µg of sequencing grade trypsin (Promega). Proteins were digested
1124 overnight rotating at room temperature. To prepare samples for desalting, glacial acetic acid was
1125 added to 10% (v/v) and debris was briefly spun down. A C18 Sep-Pak Plus cartridge (Waters)
1126 was prepared using a syringe pump and 10 mL syringe with three 10 mL washes at a flow rate
1127 of 2 mL/min: 0.1% acetic acid, 90% acetonitrile/0.1% acetic acid, and 0.1% acetic acid. The
1128 sample was loaded in a 5 mL syringe at a flow rate of 0.5 mL/min. The syringe and cartridge
1129 were washed with 5 mL of 0.1% acetic acid at a flow rate of 0.5 mL/min. A final wash was
1130 performed using 10 mL of 0.1% acetic acid at a flow rate of 2 mL/min. Peptides were eluted with
1131 4.5mL of 40% acetonitrile/0.1% acetic acid at a flow rate of 0.5 mL/min. Samples were spun in
1132 a speed vac for 3 hrs until samples could be pooled into a single 2 mL tube. Samples were frozen
1133 in liquid nitrogen and lyophilized overnight. Lyophilized peptides were stored at -80°C.

1134

1135 *Thiophosphate enrichment*

1136 To enrich for thiophosphorylated peptides, 400 µL of SulfoLink Coupling Resin slurry was used
1137 (Thermo). Incubations were performed in the dark using aluminum foil due to the light sensitivity
1138 of the resin. The resin was washed twice with 1 mL of binding buffer (25 mM HEPES, 50%
1139 acetonitrile, pH 7.0 NaOH + HCl) rotating for 5 min followed by a 1000 rpm spin for 10 sec. The
1140 supernatant was removed without disturbing the pelleted resin. The beads were blocked with

1141 1mL of blocking buffer (binding buffer with 25 µg/mL β-casein and 2 mM TCEP) and rotated for
1142 5 min at room temperature. After pelleting the resin and removing the supernatant, the resin was
1143 resuspended with lyophilized peptides dissolved in 500 µL of the blocking buffer. Samples were
1144 incubated overnight at room temperature. Samples were spun at 1000 rpm for 10 sec and the
1145 supernatant was spun again, lyophilized, and stored at -80°C prior to MS analysis. The beads
1146 received the following series of 1 mL washes for 5 min rotating and spun at 1000 rpm for 10 sec:
1147 twice with binding buffer with 2 mM TCEP, once with quenching buffer (25 mM HEPES, 50%
1148 acetonitrile, 5 mM DTT, pH 8.5 NaOH), once with binding buffer with 2 mM TCEP, once with 5%
1149 formic acid (no rotation), once with binding buffer with 2 mM TCEP, and three times with 0.1%
1150 acetic acid. The resin was no longer light sensitive after incubation with the quenching buffer. To
1151 elute captured peptides, resin was resuspended in 500 µL OXONE (2 mg/mL potassium
1152 monopersulfate) and rotated for 5 min at room temperature. The supernatant containing eluted
1153 peptides was collected after spinning at 1000 rpm for 10 sec. OXONE was removed from the
1154 sample using C18 spin columns (Pierce) according to manufacturer instructions. A total of 4
1155 washes with the equilibrium/wash buffer was performed. Peptides were spun in a speed vac
1156 until dry and stored at -80°C until MS analysis.
1157
1158 *MS data acquisition*
1159 The samples were resuspended in 10–20 µL of 0.1% formic acid for MS analysis and were
1160 analyzed on a Q-Exactive HF-X Orbitrap mass spectrometer connected to an EASY-nLC 1200
1161 chromatography system using 0.1% formic acid as Buffer A and 80% acetonitrile/0.1% formic
1162 acid as Buffer B. Peptides were loaded onto a analytical column (column: PF360-75-15-N-5,
1163 New Objective, 360 µm OD, 75 µm ID, 15 µm Tip PicoFrit Emitter; resin: 04A-4506, Phenomenex
1164 Aeris Peptide, C18 1.7 µm) via trapping column (column: 360 um OD, 100 um ID; resin: AA12S11,
1165 YMC Gel ODS-A, C18 10 µm). Peptides were separated at 300 nL/min on a gradient of 2% B for
1166 5 min, 2–25% B for 100 min, 25–40% B for 20 min, 40–100% B for 1 min, and 100% B for 12
1167 min. The orbitrap was operated in positive ion mode with a positive ion voltage of 2700V with an
1168 ion transfer tube temperature of 300°C. Full scan spectra were acquired in profile mode at a
1169 resolution of 60,000, with a scan range of 375 to 1600 m/z, 1 x 10^6 AGC target, maximum
1170 injection time of 50 msec, intensity threshold of 4 x 10^5, dynamic exclusion of 13 sec, and 20
1171 data dependent scans (DDA Top 20). MS2 spectra were generated with a HCD collision energy
1172 of 27 at a resolution of 15,000, first mass at 100 m/z, isolation window of 1.5 m/z, an AGC target
1173 of 1 x 10^5 with a maximum injection time of 20 msec, and scan range of 200 to 2000 m/z.
1174
1175 *Thiophosphorylation analysis*
1176 Raw files were analyzed in Proteome Discoverer 2.2 (Thermo Fisher Scientific) to generate peak
1177 lists and protein and peptides identifications using Sequest HT (Thermo Fisher Scientific) and
1178 the ToxoDB release 34 GT1 protein database. The maximum missed cleavage sites for trypsin
1179 was limited to 2. The following modifications were included in the search: dynamic oxidation
1180 (+15.995 Da; M), dynamic phosphorylation (+79.966 Da; S,T,Y), dynamic $^{13}C_6{}^{15}N_4$ (+10.008 Da;
1181 R), dynamic $^{13}C_6{}^{15}N_2$ (+8.014 Da; K), and dynamic acetylation (+42.011 Da; N-terminus). Site
1182 localization scores were generated using ptmRS, with phosphoRS and use of diagnostic ions
1183 set to true. SILAC 2plex (Arg10, Lys8) method was used for relative quantification of protein and

1184 unique peptide abundances. For peptide level analysis, ratios of unique peptides comparing
1185 $CDPK1^G$ and $CDPK1^M$ were generated and low abundance resampling (5%) was used to impute
1186 missing values. For protein level analysis, ratios of proteins were determined from the summed
1187 abundance of unique peptides comparing $CDPK1^G$ and $CDPK1^M$ strains.
1188
1189 Peptide and protein level data were exported from Proteome Discoverer for analysis in R. For
1190 enriched peptides, abundance ratios were calculated within each replicate for high confidence
1191 peptides ($CDPK1^G/CDPK1^M$) and normalized to the median abundance ratio of the whole
1192 proteome peptides derived from the flow through samples. Normalized abundance ratios in the
1193 flow through proteome samples were calculated by dividing abundance ratios by the median
1194 abundance ratios within each replicate. For enriched peptides, an average $\log_2$ normalized
1195 abundance ratio was calculated from three replicates. Significantly enriched peptides were
1196 calculated using a one-tailed *t*-test using the normalized abundance ratios for three replicates.
1197 A non-linear significance threshold was calculated using the function ($y = |4/x|$), where
1198 significantly enriched peptides had product value of $-\log_{10}(p)$*(mean $\log_2$ abundance ratio) greater
1199 than 4.
1200
1201 **Immunoblotting**

1202 Samples were combined with 5X Laemmli sample buffer (10% SDS, 50% glycerol, 300mM Tris
1203 HCl pH 6.8, 0.05% bromophenol blue, 5% beta-mercaptoethanol) and were incubated at 95°C
1204 for 10 min. The samples were run on precast 4–15% or 7.5% SDS gels (Bio-Rad) and were
1205 transferred overnight onto a nitrocellulose membrane in transfer buffer (25mM TrisHCl, 192 mM
1206 glycine, 0.1% SDS, 20% methanol) at 4°C. Blocking was performed with 5% milk in PBS for 1
1207 hr rocking at room temperature. Antibody incubations were performed with 5% milk in TBS-T for
1208 1 hr rocking at room temperature. Three 5 min TBS-T washes were performed before and after
1209 secondary antibody incubations rocking at room temperature. After a final PBS wash, imaging
1210 was performed using a LI-COR Odyssey.
1211
1212 For immunoblot detection of the HA tag in AID-HOOK and FTS-AID after auxin-mediated
1213 depletion, secondary antibody incubations were performed with anti-rabbit HRP antibodies
1214 (Jackson ImmunoResearch) and detected with chemiluminescence (Azure) for increased
1215 sensitivity. Imaging was performed using a Bio-Rad Gel Doc XR.
1216
1217 **Immunofluorescence analysis**

1218 HFFs were seeded onto coverslips and grown until confluence. Confluent HFFs were infected
1219 with parasites. Approximately 2 hrs later, media was exchanged with media containing either 50
1220 μM auxin or vehicle solution of PBS. At 24 hrs post-infection, the media was aspirated, and the
1221 coverslips were washed with PBS three times before fixation with 4% formaldehyde in PBS for
1222 20 min. Following three washes in PBS, the fixed cells were permeabilized with 0.25% Triton X-
1223 100 for 15 min. After three washes in PBS, the coverslips were incubated in a blocking solution
1224 (5% IFS/ 5% NGS in PBS) for 10 min at room temperature. Coverslips were incubated for 1–2
1225 hrs with primary antibody diluted in blocking solution. Anti-GAP45 or anti-MIC2 was used as a

1226 parasite counterstain. After three washes in PBS, the coverslips were incubated in blocking
1227 solution for 5 min, followed by secondary antibody diluted in blocking solution containing
1228 Hoechst 33342 for 1 hr. The coverslips were washed three times in PBS, once in water, and
1229 finally mounted with Prolong Diamond overnight at room temperature. Microscope images were
1230 acquired with the Nikon Ti Eclipse and NIS Elements software package.
1231
1232 *Immunofluorescence analysis - Figure 2*
1233 Parasite-infected HFF monolayers grown on glass coverslips were fixed with 3% formaldehyde
1234 for 15 min prior to washing with PBS. Fixed cells were then permeabilized (PBS, 0.1% Triton X-
1235 100, 10 min), blocked (3% BSA in PBS, 1 hr), and labeled with anti-HA (1:1000, 1hr; Roche). HA-
1236 tagged CDPK1 in the cWT and cMut lines was visualized with secondary goat antibodies (1:2000,
1237 1 hr; Life Technologies) conjugated to Alexa Fluor 594 and 488, respectively. Cytosolic GFP
1238 (cWT) and mCherry (cMut) were used as parasite counterstains. Nuclei were visualized with the
1239 DNA stain (DAPI; Sigma) added at 5 µg/mL with the secondary antibody. Stained coverslips were
1240 mounted on glass slides with Slowfade (Life Technologies) and imaged on a Nikon Eclipse Ti-U
1241 inverted fluorescent microscope. Images were analyzed using Nikon NIS Elements imaging
1242 software.
1243
1244 **Plaque Assays**

1245 600 and 1200 parasites were used to infect 6-well plates of HFFs in 10% IFS media. At 1 dpi,
1246 media was exchanged with 10% IFS media containing either 50 µM auxin or vehicle solution of
1247 PBS. Parasites were allowed to grow undisturbed for 8 days total. Plates were washed with PBS
1248 and fixed for 10 min with 100% ethanol at room temperature. After removing ethanol, plates
1249 were allowed to dry prior to staining with crystal violet solution for 30 min to 1 hr. Plates were
1250 washed 3 times with PBS, once with water, and allowed to dry before scanning.
1251
1252 *Plaque assays - Figure 2*
1253 Parasites were harvested by syringe lysis, counted, and 200 parasites were seeded on confluent
1254 HFF monolayers grown in 24-well plates (Falcon). Wells were treated with 500 µM auxin or
1255 vehicle (ethanol) and plaques were allowed to form for 5 days. Plaque formation was assessed
1256 by inspecting the methanol fixed and 0.1% crystal violet stained HFF monolayers.
1257
1258 **Invasion assays**

1259 Confluent HFFs seeded in T12.5 flasks were infected with parasites. Approximately 2 hrs later,
1260 the media was exchanged for 10% IFS media containing either 50 µM auxin or vehicle solution
1261 of PBS. Parasites were harvested at 2 dpi and the media was exchanged for 1% IFS in invasion
1262 media (DMEM Sigma D2902, 20 mM HEPES, pH 7.4) with auxin or vehicle PBS added. Confluent
1263 HFFs seeded in clear-bottomed 96-well plates were infected with 2 x 10^5 extracellular parasites.
1264 After centrifuging the plate at 290 x *g* for 5 min to synchronize invasion, the infected 96-well plate
1265 was incubated by floating on a water bath at 37°C/5% CO_2 for 90 min. Wells were washed once
1266 with PBS before fixing infected HFFs with 4% formaldehyde in PBS for 20 min at room
1267 temperature. Wells were washed three times with a wash buffer (1% NGS in PBS) and then

1268 incubated in a blocking buffer (5% IFS and 1% NGS in PBS) overnight at 4°C. To stain
1269 extracellular parasites, wells were incubated with anti-SAG1 antibody for 30 min at room
1270 temperature. After washing wells three times with a wash buffer, fixed HFFs were permeabilized
1271 in 0.25% TritonX-100 in blocking buffer for 8 min room temperature. After washing the wells
1272 three times with a wash buffer, the wells were incubated in a blocking buffer for 10 min at room
1273 temperature, followed by anti-GAP45 antibody for 30 min at room temperature to label all
1274 parasites. After three washes in a wash buffer, wells were incubated with a secondary antibody
1275 solution containing Hoechst for 30 min. After three washes in PBS, wells were imaged using a
1276 Biotek Cytation 3.
1277
1278 **Egress assays**

1279 Confluent HFFs seeded in glass bottomed 35 mm dishes (Ibidi or Mattek) were infected with
1280 approximately 2 x 10^5 parasites. Approximately 2 hrs later, the media was exchanged for 10%
1281 IFS media containing either 50 µM auxin or vehicle solution of PBS. At 24 hrs post-infection, the
1282 media was replaced with 1% IFS in Ringer's (155 mM NaCl, 2 mM $CaCl_2$, 3 mM KCl, 1 mM
1283 $MgCl_2$, 3 mM NaH_2PO_4, 10 mM HEPES, 10 mM glucose, pH 7.4). Zaprinast (final concentration
1284 500 µM) was added into the dishes after 15 sec of imaging and imaging of infected HFFs
1285 continued for a total of 10 min. Images were acquired using a Nikon Ti Eclipse with an enclosure
1286 maintained at 37°C. The number of intracellular vacuoles was quantified at 0 min and 10 min.
1287 Results are the sum of four fields of view per condition and are representative of three
1288 independent experiments.
1289
1290 *Egress assays - Figure 2*
1291 Parasites were added to HFF monolayer and grown for 24 hrs in a 96 well plate. The wells were
1292 then treated with 500 µM auxin or an equivalent volume of vehicle (ethanol) for 2 hrs and then
1293 washed with PBS (2x). The media was exchanged for 100 µl Ringer's solution (155 mM NaCl, 3
1294 mM KCl, 2 mM $CaCl_2$, 1 mM $MgCl_2$, 3 mM NaH_2PO_4, 10 mM HEPES, 10 mM glucose) and the
1295 plate was placed on a heating block to maintain the temperature at 37°C. To artificially induce
1296 egress, 50 µL of Ringer's solution containing 24 µM ionophore (8 µM final, Thermo) was added
1297 to each well. At specified time points the cells were fixed by adding 33 µL 16% formaldehyde
1298 (3% final) for 15 min. Cells were washed in PBS (3x) and stained with rabbit anti-TgCAP 1:2000
1299 (Hunt et al., 2019) followed by goat anti-rabbit Alexa Fluor 488 (1:2000) and DAPI (5 µg/mL).
1300 Automated image acquisition of 25 fields per well was performed on a Cellomics Array Scan VTI
1301 HCS reader (Thermo Scientific) using a 20x objective. Image analysis was performed using the
1302 Compartmental Analysis BioApplication on HCS Studio (Thermo Scientific). Egress levels were
1303 determined in triplicate for three independent assays. Vacuole counts were normalized to $t = 0$
1304 to determine how many intact vacuoles had remained after egress. The results were statistically
1305 tested using one-way ANOVA with Tukey's multiple comparison test in GraphPad Prism 7. The
1306 data are presented as mean ± s.d.
1307

1308 **Replication assays**

1309 Confluent HFFs seeded on coverslips were infected with parasites. Parasites were centrifuged
1310 at 290 x *g* for 5 min to synchronize invasion of host cells. Approximately 2 hrs later, the media
1311 was exchanged for 10% IFS media containing either 50 μM auxin or vehicle solution of PBS. At
1312 24 hrs post-infection, the media was aspirated and fixed as described in "Immunofluorescence
1313 Analysis". Coverslips were incubated in primary and secondary antibodies for 30 min. Anti-
1314 GAP45 antibody was used to visualize parasites. Microscope images were acquired with the
1315 Nikon Ti Eclipse and NIS Elements software package. Tiled images were acquired in a four-by-
1316 four manner using a 40x objective. Parasites per vacuole were quantified for at least 100
1317 vacuoles for three biological replicates.
1318

1319 **Immunoprecipitation of HOOK and FTS complex**

1320 *Parasite harvest*
1321 HOOK-3xHA, CDPK1-AID (parental), FTS-3xHA and TIR1 (parental) parasites were infected onto
1322 confluent HFFs in 15 cm dishes. After the parasites lysed the HFF monolayer (approximately 40
1323 hrs post-infection), extracellular parasites were passed through 5 μm filters and washed twice
1324 with DMEM by pelleting at 1000 x *g* for 10 min. Parasite pellets were resuspended in 1X Dynein
1325 Lysis Buffer (DLB) (30 mM HEPES, 50 mM KOAc1, 2 mM MgOAc, 10% glycerol, 1 mM EGTA pH
1326 8.0, 1 mM DTT, 0.5 mM ATP, 125 units/mL benzonase, 1X HALT protease and phosphatase
1327 inhibitor, and 1% NP-40 IGEPAL CA 630) to achieve a concentration of 6.67 x 10^8 parasites/mL
1328 (Redwine et al., 2017). Parasites were lysed on ice for 10 min and vortexed periodically to
1329 facilitate lysis. Lysates were centrifuged at 1000 x *g* for 5 min at room temperature to pellet
1330 unlysed parasites and the lysate supernatant was collected and used as the immunoprecipitation
1331 input.
1332

1333 *Immunoprecipitation*
1334 25 μL of anti-HA magnetic beads (Thermo Scientific 88836) was used for 200 μL of parasite
1335 lysate. Beads were aliquoted and washed three times with a wash buffer (30 mM HEPES, 50 mM
1336 KOAc1, 2 mM MgOAc, 10% glycerol, 1 mM EGTA pH 8.0, 1 mM DTT, 0.5 mM ATP, and 0.01%
1337 NP-40 IGEPAL CA 630) using a magnetic rack. To begin the pulldown, 200 μL of parasite lysate
1338 was used to resuspend washed beads. Tubes were rotated at 4°C for 1 hr (FTS-AID and TIR1)
1339 and 3 hrs (HOOK-3xHA and CDPK1-AID). Beads were resuspended in 250 μL of wash buffer,
1340 transferred to a new tube, and received two additional washes with the same volume. Proteins
1341 were eluted by resuspending beads in 22 μL of 1X S-trap sample buffer (5% SDS, 50 mM TEAB,
1342 pH 7.5) and incubated at 70°C for 10 min. The eluate was collected for MS sample processing
1343 and analysis. Results are representative of three independent experiments.
1344

1345 *Protein cleanup and digestion*
1346 Proteins were prepared for mass spectrometry as described above in "Sub-minute
1347 phosphoproteomics - Protein cleanup and digestion". Eluted peptides were frozen in liquid
1348 nitrogen, lyophilized, and stored at -80°C until MS analysis.
1349

1350 *MS data acquisition*
1351 Lyophilized peptides were resuspended in 25 µL of 0.1% formic acid and were analyzed on an
1352 Exploris 480 Orbitrap mass spectrometer equipped with a FAIMS Pro source (Bekker-Jensen et
1353 al., 2020) connected to an EASY-nLC chromatography system using 0.1% formic acid as Buffer
1354 A and 80% acetonitrile/0.1% formic acid as Buffer B. Peptides were separated at 300 nL/min on
1355 a gradient of 1–6% B for 1 min, 6–21% B for 41 min and 30 sec, 21–36% B for 20 min and 45
1356 sec, 36–50% B for 10 min and 15 sec, 100% B for 14 min and 30 sec, 100–2% B for 3 min, 2%
1357 B for 3 min, 2–98% B for 3 min, and 98% B for 3 min. The orbitrap and FAIMS were operated in
1358 positive ion mode with a positive ion voltage of 1800V; with an ion transfer tube temperature of
1359 270°C; using a standard FAIMS resolution and compensation voltage of -50 and -65V, an inner
1360 and outer electrode temperature of 100°C with 4.5 mL/min carrier gas. Full scan spectra were
1361 acquired in profile mode at a resolution of 60,000, with a scan range of 350-1400 m/z, 300%
1362 AGC target, 25 msec maximum injection time, intensity threshold of 5 x 10^3, 2–6 charge state,
1363 dynamic exclusion of 20 sec, 15 data dependent scans (DDA Top 15), and mass tolerance of 10
1364 ppm. MS2 spectra were generated an HCD collision energy of 30 at a resolution of 15,000, first
1365 mass at 110 m/z, with an isolation window of 1.3 m/z, and an automatically determined AGC
1366 target and maximum injection time in standard and auto mode.
1367
1368 *Immunoprecipitation MS analysis*
1369 Raw files were analyzed in Proteome Discoverer 2.4 (Thermo Fisher Scientific) to generate peak
1370 lists and protein and peptides identifications using Sequest HT (Thermo Fisher Scientific) and
1371 the ToxoDB release 49 GT1 protein database. The maximum missed cleavage sites for trypsin
1372 was limited to 2. The following modifications were included in the search: dynamic oxidation
1373 (+15.995 Da; M), dynamic phosphorylation (+79.966 Da; S,T,Y), dynamic acetylation (+42.011
1374 Da; N-terminus), and static methylthio (+45.988 Da; C). Label free quantification of proteins was
1375 performed using summed abundances from unique peptides. Abundances were normalized on
1376 the total peptide amount. Pairwise ratios were calculated for protein abundances comparing
1377 strains and conditions. Significance values were derived from *t*-tests across three replicates and
1378 adjusted with Benjamini-Hochberg correction. Exported protein abundance files from Proteome
1379 Discoverer 2.4 were loaded into R (version 4.1.1).
1380
1381 **Proximity labeling FTS-TurboID**

1382 *Parasite harvest and treatment*
1383 FTS-TurboID and mNG-TurboID (cytosolic control) parasites were infected onto confluent HFFs
1384 in 15 cm dishes. After the parasites lysed the HFF monolayer (approximately 40 hrs post-
1385 infection), extracellular parasites were passed through 5 µm filters and washed twice with DMEM
1386 by pelleting at 1000 x *g* for 10 min. At least 1 x 10^8 Parasites were resuspended in 200 µL of
1387 DMEM. 200 µL of biotin (final concentration 500 µM) or vehicle DMSO in DMEM was mixed with
1388 parasites. Tubes were incubated in a water bath at 37°C for 5 min. Parasites were pelleted at
1389 12,000 x *g* for 1 min at 4°C for a total of three 1 mL PBS washes. Parasites were resuspended
1390 in a RIPA NP-40 lysis buffer (10 mM Tris-HCl pH 7.5, 140 mM NaCl, 1% NP-40 IGEPAL CA 630,
1391 0.1% sodium deoxycholate, 0.1% SDS, 1x HALT protease inhibitor, and 125 units/mL

1392 benzonase) at a parasite concentration of 5 x 10^8 parasites/mL. Parasites were lysed at room
1393 temperature for 15 min and stored at -20°C. Results are representative of three independent
1394 experiments.
1395
1396 *Biotinylated protein enrichment*
1397 Streptavidin magnetic beads were washed three times with a RIPA NP-40 lysis buffer. Thawed
1398 lysates were spun at 16,000 x *g* for 5 min at 4°C and the supernatant was used as the pulldown
1399 input. 20 µL of streptavidin magnetic beads was used for 200 µL of lysates (1 x 10^8 parasites).
1400 Beads were incubated with lysate rotating for 1 hr. Beads received a series of 1 mL washes:
1401 twice with the RIPA NP-40 lysis buffer, once with 1 M KCl, once with 0.1M Na_2CO_3 (pH 11), once
1402 with 2 M urea in 10 mM Tris pH 8.0), and twice with RIPA NP-40 lysis buffer. Proteins were eluted
1403 by incubating beads with 2.5 mM biotin in S-trap sample buffer (5% SDS, 50 mM TEAB, pH 7.5)
1404 for 10 min at 95°C.
1405
1406 *Protein cleanup and digestion*
1407 Proteins were prepared for mass spectrometry as described above in "Sub-minute
1408 phosphoproteomics - Protein cleanup and digestion". Eluted peptides were frozen in liquid
1409 nitrogen, lyophilized, and stored at -80°C until MS analysis.
1410
1411 *MS data acquisition*
1412 Lyophilized peptides were resuspended in 25 µL of 0.1% formic acid and were analyzed on an
1413 Exploris 480 Orbitrap mass spectrometer equipped with a FAIMS Pro source (Bekker-Jensen et
1414 al., 2020) connected to an EASY-nLC chromatography system using 0.1% formic acid as Buffer
1415 A and 80% acetonitrile/0.1% formic acid as Buffer B. Peptides were separated at 300 nL/min on
1416 a gradient of 2% B for 1 min, 2–25% B for 41 min, 25–40% B for 6 min, 40–100% B for 12 min,
1417 100–2% B for 3 min, 2% B for 3 min, 2–98% B for 3 min, and 98% B for 3 min. The orbitrap and
1418 FAIMS were operated in positive ion mode with a positive ion voltage of 1800V; with an ion
1419 transfer tube temperature of 270°C; using a standard FAIMS resolution and compensation
1420 voltage of -50 and -65V, an inner and outer electrode temperature of 100°C with 4.5 mL/min
1421 carrier gas. Full scan spectra were acquired in profile mode at a resolution of 60,000, with a scan
1422 range of 350–1400 m/z, 300% AGC target, 25 msec maximum injection time, intensity threshold
1423 of 5 x 10^3, 2–6 charge state, dynamic exclusion of 20 sec, 15 data dependent scans (DDA Top
1424 15), and mass tolerance of 10 ppm. MS2 spectra were generated with a HCD collision energy of
1425 30 at a resolution of 15,000, first mass at 110 m/z, with an isolation window of 1.3 m/z, and a
1426 normalized AGC target of 200% with an automatically determined maximum injection time.
1427
1428 *Proximity labeling MS analysis*
1429 Raw files were analyzed in Proteome Discoverer 2.4 (Thermo Fisher Scientific) to generate peak
1430 lists and protein and peptides identifications using Sequest HT (Thermo Fisher Scientific) and
1431 the ToxoDB release 49 GT1 protein database. The maximum missed cleavage sites for trypsin
1432 was limited to 2. The following modifications were included in the search: dynamic oxidation
1433 (+15.995 Da; M), dynamic phosphorylation (+79.966 Da; S,T,Y), dynamic biotinylation (+226.078
1434 Da; K, N-terminus), dynamic acetylation (+42.011 Da; N-terminus), and static methylthio

1435 (+45.988 Da; C). Label free quantification of proteins was performed using summed abundances
1436 from unique peptides. Abundances were normalized on the total peptide amount. Pairwise ratios
1437 were calculated for protein abundances comparing strains and conditions. Significance values
1438 were derived from *t*-tests across three replicates and adjusted with Benjamini-Hochberg
1439 correction. Exported protein abundance files from Proteome Discoverer 2.4 were loaded into R
1440 (version 4.1.1).
1441
1442 **MIC2 secretion assays**

1443 *Parasite harvest and treatment*
1444 Extracellular parasites were harvested in chilled DMEM and washed twice in DMEM after
1445 centrifugation at 1000 x *g* for 10 min at 4°C. Parasites were resuspended at a concentration of
1446 6 x 10^8 parasites/mL in cold DMEM. 3 x 10^7 parasites were aliquoted into round-bottom 96-well
1447 plates. An additional aliquot of parasites was lysed in 5X Laemmli sample buffer (see
1448 "Immunoblotting" for recipe) to obtain the total parasite lysate used to determine total MIC2
1449 levels. Secretion was stimulated in plates with IFS and ethanol in DMEM (final concentration 3%
1450 IFS and 1% ethanol) or a vehicle solution of DMEM. Plates were incubated by floating on a water
1451 bath at 37°C/5% CO_2 for 90 min. Plates were spun at 1000 x *g* for 5 min at 4°C to separate
1452 parasites from secreted proteins. Supernatants were transferred to a new well and spun again.
1453 The final supernatant was mixed with a 5X Laemmli sample buffer, boiled at 95°C for 10 min,
1454 and stored at -20°C along with total lysates until immunoblot analysis.
1455
1456 *Immunoblot analysis and quantification*
1457 To quantify MIC2 protein levels, a standard curve derived from the total parasite lysate was
1458 generated alongside supernatants containing secreted microneme proteins. The standard curve
1459 was derived from 3-fold serial dilutions of the total parasite lysate (undiluted, 1:3, 1:9, and 1:27)
1460 in a 1X Laemmli sample buffer. The serial dilutions and supernatants of auxin- and vehicle-
1461 treated parasites of a single strain were loaded onto the same precast 4–15% gel (Bio-Rad).
1462 Subsequent immunoblotting steps were performed as described in "Immunoblotting". Anti-MIC2
1463 was used to detect total and secreted MIC2 proteins. Secreted MIC2 proteins have a lower
1464 molecular weight due to parasite-mediated proteolytic cleavage. Anti-CDPK1 was used as a
1465 loading control for total parasite lysate and to reveal any parasite lysis or carry over in the
1466 supernatant. Immunoblots confirming the depletion of tagged proteins were also collected.
1467 Imaging was performed on a LI-COR Odyssey at high resolution for quantification.
1468
1469 Immunoblot quantification was performed in Fiji on unadjusted inverted images. For a single
1470 immunoblot, lane profiles of uniform dimensions were generated for MIC2 signal. Background-
1471 subtracted signal intensity was measured as an area using the line and wand tool. A standard
1472 curve was derived from the quantified MIC2 signal of the dilution series. Standard curves across
1473 all conditions and replicates had R^2 values greater than 0.90. Secreted MIC2 signals were within
1474 the linear range of the standard curve and were used to calculate the percent of total MIC2
1475 secreted. Results are representative of three independent experiments for each parasite strain.
1476

1477 **Microneme relocalization**

1478 Parasites expressing the CLAMP-mNG reporter were grown in HFFs in glass-bottomed 35mm
1479 dishes (Ibidi and Mattek) for approximately 20 hrs. For 3-MB-PP1 treatment, media was
1480 exchanged 30 min prior to live microscopy for 3% IFS in Ringer's buffer (155 mM NaCl, 2mM
1481 $CaCl_2$, 3mM KCl, 1mM $MgCl_2$, 3mM NaH_2PO_4, 10mM HEPES, 10 mM glucose, pH 7.4) containing
1482 either 3 μM 3-MB-PP1 or vehicle solution of DMSO. At approximately 1 min after beginning live
1483 microscopy, parasites were stimulated with zaprinast (500 μM final concentration) or a vehicle
1484 solution of DMSO in corresponding Ringer's buffer. For TIR1/CLAMP-mNG and AID-
1485 HOOK/CLAMP-mNG parasite, media was exchanged 2 hrs after infection for 10% IFS media
1486 containing either 50 μM auxin or vehicle solution of PBS. Media was exchanged for 3% IFS in
1487 Ringer's buffer just prior to live microscopy. At approximately 30 sec after beginning live
1488 microscopy, parasites were stimulated with zaprinast (500 μM final concentration) or a vehicle
1489 solution of DMSO in corresponding Ringer's buffer. Images were recorded every 5–7 sec until
1490 egress or approximately 5 min using a Nikon Ti Eclipse with an enclosure maintained at 37°C.
1491
1492 Microneme relocalization was quantified using built-in commands from ImageJ (v. 1.53e). To
1493 determine the distribution of fluorescent micronemes at a specific time frame, a line was drawn
1494 from the parasite's apical end to its basal end. The "plot profile" command was applied to this
1495 line to calculate fluorescence intensity at regularly spaced intervals (0.13 microns) across the
1496 parasite on unadjusted images. This process was repeated for each time frame of interest and
1497 for each parasite in the analyzed vacuole. Regression analysis was performed on relocalization
1498 data from each time frame, resulting in logarithmic regression plots that display how
1499 fluorescence intensity correlates with distance from the parasite's apical end. Microneme
1500 relocalization is shown as SuperPlots to simultaneously visualize the median relocalization of an
1501 entire vacuole and the relocalization of individual parasites within each vacuole (Lord et al., 2020).
1502

1503 **Microneme localization in extracellular parasites**

1504 Microneme localization in extracellular parasites was quantified using a custom-built, image
1505 analysis pipeline. ImageJ's built-in commands were used to measure the length of the parasite's
1506 major axis. Based on the patterns of vehicle-treated TIR1/CLAMP-mNG data, 1/8th of the
1507 parasite closest to the apical end was deemed the apical region. The remaining region was
1508 deemed the body. Using the Interactive Learning and Segmentation Toolkit (ilastik v. 1.3.3) (Berg
1509 et al., 2019), the apical region and body of parasites were isolated from each other and from the
1510 surrounding media. Ilastik's pixel and object quantification tools were then used to determine
1511 the total intensity of fluorescence in each of these regions. Comparing these values to each other
1512 yielded the percentage of fluorescent micronemes present in each of these sections in relation
1513 to the total fluorescence present in the parasite. This process was repeated for several
1514 extracellular parasites in each of the conditions tested.
1515

ACKNOWLEDGEMENTS

We thank all the members of the Lourido laboratory for helpful discussions and support, especially Tyler Smith for aiding with the tagging vector design and Christopher Giuliano for insights during data analysis. We thank Forest M. White for generous support in developing the mass spectrometry methodologies used in this study and for helpful discussions. For data in Figure 2, we thank Matthew Child and Matt Bogyo for the CDPK1 antibody, Peter Bradley for the GAP45 antibody, John Boothroyd for the SAG1 antibody. We thank Marc-Jan Gubbels for the alpha-tubulin antibody, L. David Sibley for the MIC2, SAG1, and ALD antibody, Peter Bradley for the ROP1 antibody, Drew Etheridge for the GAP45 antibody, and Dominique Soldati-Favre for the GAP45 antibody. This work relied on VEuPathDB.org and we thank all contributors to this resource. This research was supported by funds from National Institutes of Health grants to SL (R01AI144369) and MB and MT (R01AI123457), a National Science Foundation Graduate Research Fellowship to AWC and ALH (174530). MT received funding from the Francis Crick Institute which receives its core funding from Cancer Research UK (CC2132), the UK Medical Research Council (CC2132), and the Wellcome Trust (CC2132). The Science Technology Proteomics Platform at the Francis Crick Institute received funding from Cancer Research UK (CC0199), the UK Medical Research Council (CC0199), and the Wellcome Trust (CC0199). For the purpose of Open Access, the authors have applied a CC BY public copyright license to any Author Accepted Manuscript version arising from this submission.

COMPETING INTERESTS

The authors declare no competing interests.

FIGURE AND FIGURE LEGENDS

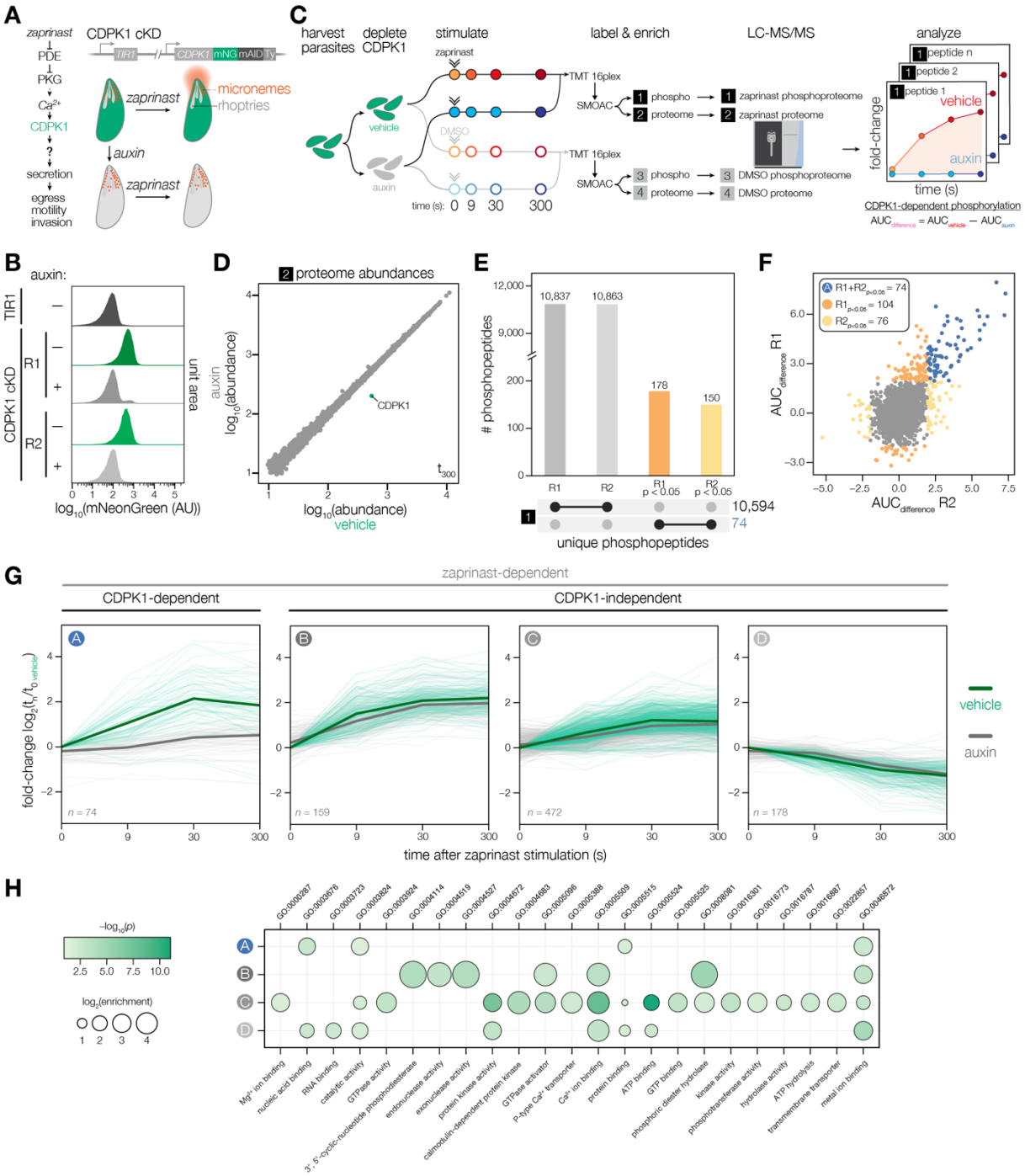

Figure 1. Identifying CDPK1-dependent phosphorylation with sub-minute resolution. (A) Stimulating parasites with zaprinast triggers Ca^{2+}-mediated activation of CDPK1, resulting in the secretion of microneme proteins (red) required for motile stages of the parasite. Conditional knockdown (cKD) of CDPK1 endogenously tagged with mNeonGreen-mAID-Ty (green) after

1546 auxin treatment. **(B)** Flow cytometry of mNeonGreen (mNG) fluorescence in extracellular CDPK1
1547 cKD or parental TIR1 parasites treated with vehicle or auxin for 3.5 hrs. **(C)** Schematic of
1548 phosphoproteomic time course. Parasites were harvested prior to CDPK1 depletion with auxin
1549 for 3.5 hrs, followed by stimulation with zaprinast or vehicle (DMSO). Samples were collected at
1550 0, 9, 30, and 300 sec. The experiment was performed in biological replicates. Samples were
1551 labeled with TMTpro, pooled for analysis, and phosphopeptides were enriched using SMOAC
1552 prior to LC-MS/MS. Four sets of samples were generated: enriched phosphoproteomes for
1553 zaprinast [1] and DMSO [3], and proteomes for zaprinast [2] and DMSO [4]. Mock reporter ion
1554 intensities enabling relative quantification for a given peptide are shown to illustrate fold-change
1555 of unique phosphopeptide abundances during zaprinast stimulation. CDPK1-dependent
1556 phosphorylation is determined by calculating the area under the curve (AUC) difference between
1557 vehicle and auxin treatment conditions. **(D)** Protein abundances in the zaprinast proteome set
1558 [2] at 300 sec comparing vehicle- and auxin-treated CDPK1 cKD parasites. **(E)** UpSet plot for
1559 the number of phosphopeptides identified in the enriched zaprinast phosphoproteome [1] across
1560 individual replicates. Phosphopeptides exhibiting CDPK1-dependent phosphorylation with $p <$
1561 0.05 are indicated. **(F)** Scatter plot of $AUC_{difference}$ values of enriched zaprinast phosphopeptides
1562 [1] across biological replicates. Significance was determined by comparing the distribution of
1563 $AUC_{difference}$ values from zaprinast phosphopeptides [1] to a null distribution of DMSO
1564 phosphopeptides [3] for individual replicates. **(G)** CDPK1-dependent and zaprinast-dependent
1565 phosphopeptide abundances over time. Ratios of zaprinast-treated samples relative to the
1566 vehicle-treated (no auxin) $t = 0$ samples. Median ratios of a group (solid lines). Individual
1567 phosphopeptides (opaque lines). CDPK1-dependent phosphopeptides (Group A) determined as
1568 described in F. Zaprinast-dependent phosphopeptides (Groups B, C, and D) were determined
1569 by comparing the distribution of $AUC_{vehicle}$ values from zaprinast phosphopeptides [1] to a null
1570 distribution of DMSO phosphopeptides [3]. Groups were determined by projection-based
1571 clustering. **(H)** GO terms enriched among phosphopeptides undergoing a significant change
1572 after zaprinast stimulation. Significance was determined using a hypergeometric test.

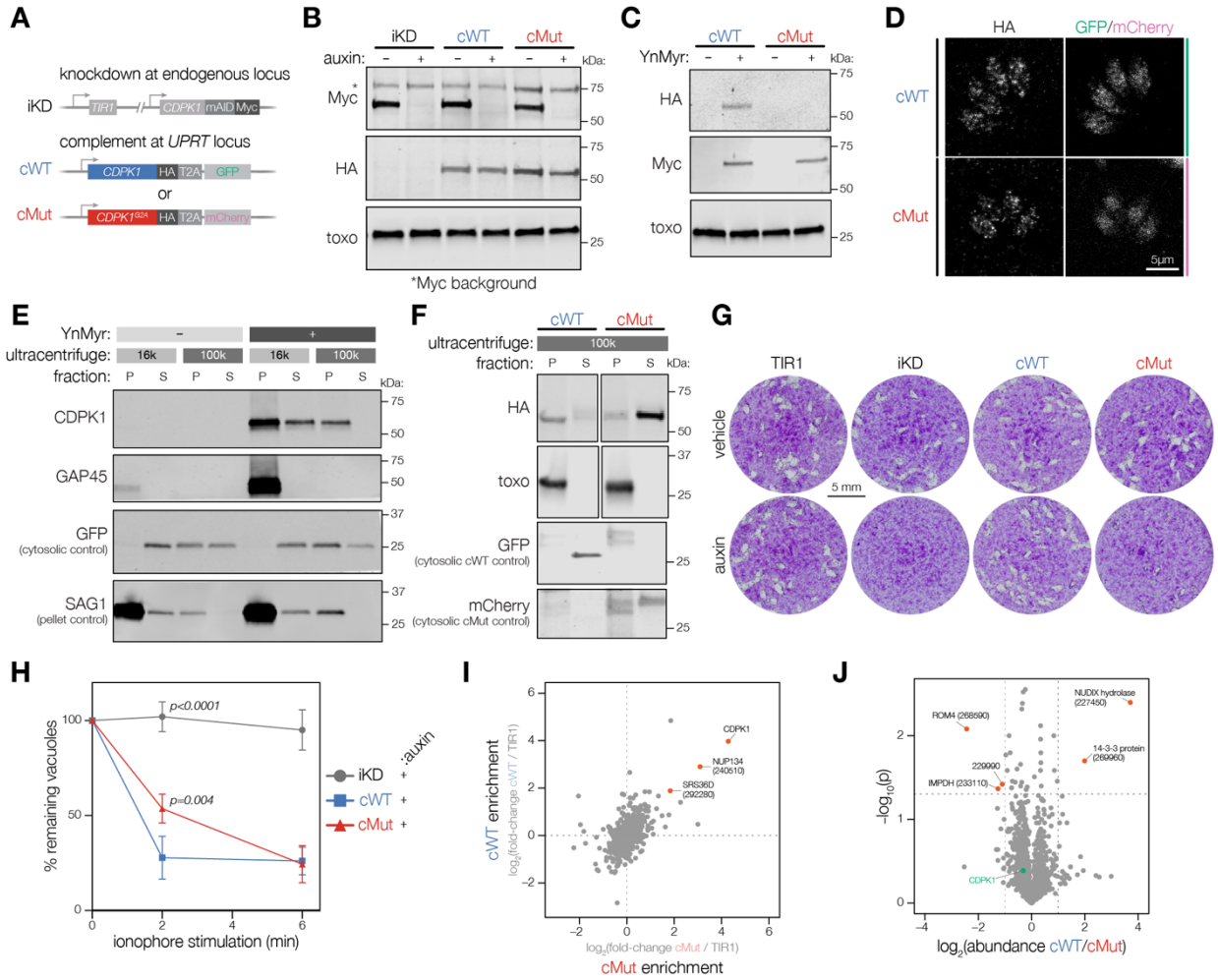

Figure 2. Myristoylation modulates CDPK1 activity and alters its interacting partners. (A) Complementation strategy used to evaluate the functional importance of CDPK1 myristoylation. See Figure 2—figure supplement 1 for the construction of the iKD line. **(B)** Immunoblot demonstrating the auxin-dependent depletion of endogenous CDPK1 in the iKD, cWT, and cMut parasites (Myc) as well as equivalent expression of the complements (HA). *T. gondii* (toxo) antibody was used as a loading control. **(C)** Biochemical validation of complemented lines by YnMyr-dependent pull down. Enrichment of WT and Mut complements (HA). The inducible endogenous CDPK1 (Myc) and *T. gondii* (toxo) antibody was used as enrichment and loading controls, respectively. **(D)** Localization of the complemented versions of CDPK1 and corresponding cytosolic reporters within cWT (GFP) and cMut (mCherry) by immunofluorescence. **(E)** Myristoylation-dependent subcellular partitioning of CDPK1. Localization of YnMyr-enriched CDPK1 was evaluated using differential centrifugation. The partitioning into pellet [P] and supernatant [S] fractions was detected by immunoblot (CDPK1) and compared to doubly acylated GAP45. GFP and SAG1 were used as S and P controls, respectively. As only half of the supernatant fraction was removed from the high-speed pellet (100,000 x *g*), the GFP signal is present in the latter. **(F)** Partitioning of complemented WT and mutant CDPK1 after high speed centrifugation (HA). *T. gondii* (toxo) antibody was used as a P

1591 control whereas GFP and mCherry were used as S controls for cWT and cMut, respectively. **(G)**
1592 Plaque assays demonstrating that myristoylation of CDPK1 is important for the lytic cycle of
1593 *T. gondii*. **(H)** Lack of CDPK1 myristoylation delays ionophore-induced egress from host cells.
1594 Each data point is an average of $n = 3$ biological replicates, error bars represent standard
1595 deviation. Significance calculated using 1-way ANOVA with Tukey's multiple comparison test.
1596 See Figure 2—figure supplement 1 for vehicle controls. **(I)** Immunoprecipitation-MS (IP-MS) of
1597 CDPK1-HA in cWT, cMut, and untagged TIR1 parasites across $n = 2$ biological replicates.
1598 Significantly enriched proteins (red) for proteins with more than three unique peptides, $p_{cWT} <$
1599 0.05, and $p_{cMut} < 0.05$, and $\log_2$ fold-change > 1 across both pull-downs; *t*-tests and Benjamini-
1600 Hochberg corrected. **(J)** IP-MS fold-enrichment comparing cWT and cMut pull-downs.
1601 Significantly enriched proteins (red) for proteins with more than 3 unique peptides, $p < 0.05$, and
1602 $\log_2$ fold-change > 1 or < -1; *t*-test and Benjamini-Hochberg corrected.

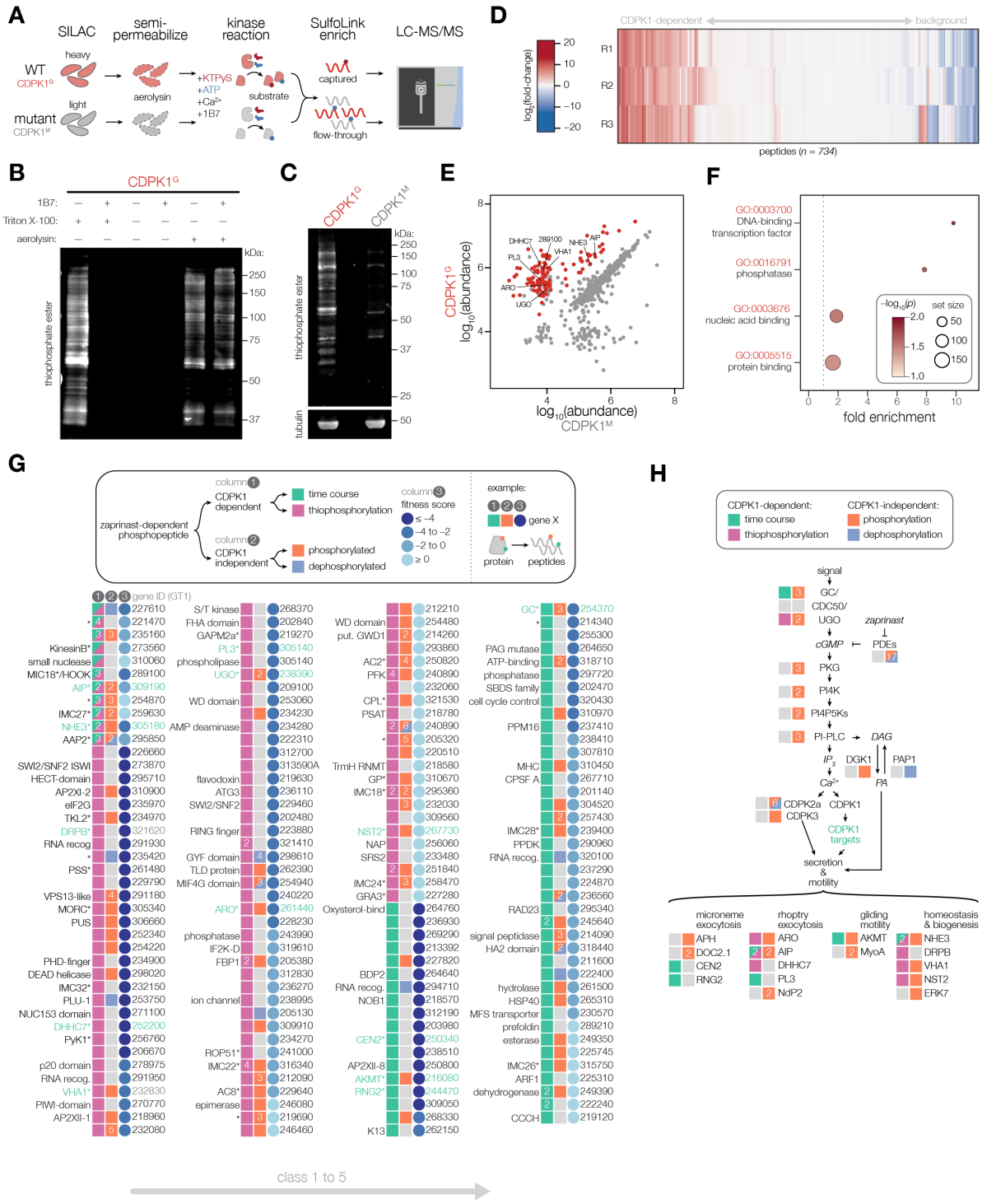

Figure 3. Identifying the direct substrates of CDPK1. (A) Schematic describing a strategy to identify direct substrates of CDPK1. WT (CDPK1^{G}) and mutant (G128M; CDPK1^{M}) parasites were grown in SILAC media for multiplexed quantitation. Extracellular parasites were semi-permeabilized with aerolysin, enabling diffusion of small molecules but not proteins. CDPK1 substrate labeling was initiated by treating semi-permeabilized parasites with Ca^{2+}, KTPγS, ATP, and 1B7. While CDPK1 in both WT and mutant parasites can utilize ATP to phosphorylate

substrates, only WT parasites can use KTPγS to thiophosphorylate substrates. Thiophosphorylated peptides were specifically enriched and the remaining flow-through was saved for whole proteome analysis. Enriched and whole proteome samples were analyzed by LC-MS/MS. **(B)** 1B7 nanobody treatment inhibits non-specific extracellular kinase activity of CDPK1. Thiophosphorylated substrates were detected in lysates using an anti-thiophosphate ester antibody immunoblot. Extracellular CDPK1 activity (lane 1) was blocked by 1B7 (lane 2). Aerolysin treatment resulted in intracellular labeling (lane 5) that was unaffected by 1B7 (lane 6). **(C)** Thiophosphorylation performed in aerolysin-treated parasites comparing WT ($CDPK1^{G}$) and mutant ($CDPK1^{M}$) strains. Detection was performed as in B. Tubulin was used as a loading control. **(D)** Heatmap quantification of peptides using LC-MS/MS. Fold-change of peptide abundance shown as a ratio of WT ($CDPK1^{G}$) to mutant ($CDPK1^{M}$) abundances. Experiment was performed in n = 3 biological replicates. **(E)** Abundances of unique peptides after thiophosphorylation in $CDPK1^{G}$ and $CDPK1^{M}$ parasites across n = 3 biological replicates. Significantly enriched phosphorylated peptides are colored in red ($-\log_{10}(p)$*fold-change > 4), one-tailed t-test. **(F)** GO terms enriched among significant phosphopeptides from E. Significance was determined using a hypergeometric test. **(G)** Putative targets of CDPK1 determined by sub-minute phosphoproteomics and thiophosphorylation of direct substrates. For a given CDPK1 target gene, the presence of a unique peptide phosphorylated in a CDPK1-dependent manner (column 1) is indicated if identified in the time course (green) and/or thiophosphorylation (magenta). The presence of additional unique phosphorylated peptides exhibiting zaprinast-dependent effects (column 2) is indicated if the peptide was phosphorylated (orange) or dephosphorylated (blue). Numbered boxes indicate multiple unique peptides. Fitness scores (column 3) obtained from genome-wide KO screen data (blues). Lower scores indicate gene is required for lytic stages of the parasite. Gene names (left), TGGT1 gene IDs (right). Gene names with asterisks (*) are associated with published data. **(H)** Signaling diagram describing parasite motility. Proteins exhibiting CDPK1-dependent phosphorylation by either sub-minute phosphoproteomics or thiophosphorylation are indicated (green). Proteins exhibiting CDPK1-independent phosphorylation (red) or dephosphorylation (blue) are indicated.

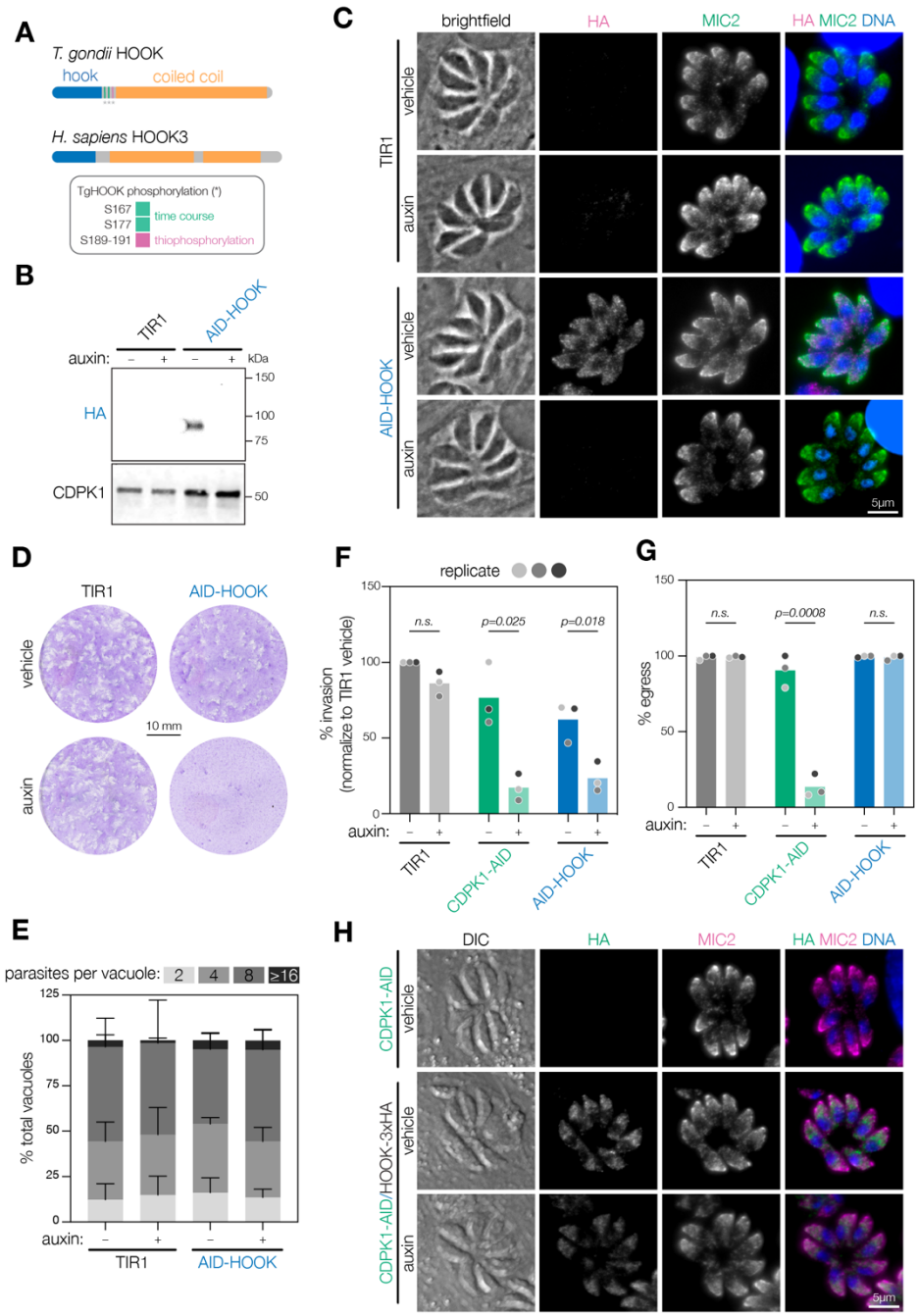

Figure 4. HOOK is required for host cell invasion, but dispensable for egress. (A) Schematic of *T. gondii* and *H. sapiens* HOOK protein domains. HOOK domain (blue), coiled-coil domain (yellow), sites phosphorylated by CDPK1 (red). **(B)** Immunoblot of HOOK conditional knockdown parasites (AID-HOOK) after auxin treatment for 40 hrs compared to untagged TIR1 parasites. CDPK1 was used as a loading control. **(C)** AID-HOOK is visualized in fixed intracellular parasites by immunofluorescence after auxin treatment for 24 hrs. Hoechst and MIC2 are used as counterstains. **(D)** Plaque assays of host cells infected with TIR1 or AID-HOOK parasites for 8 days in auxin. Host cells are stained with crystal violet. (**E**) Replication assays of host cells infected with TIR1 or AID-HOOK parasites in auxin for 24 hrs. Parasites per vacuole were

1649 quantified from immunofluorescence on fixed intracellular parasites. $p > 0.9$. Two-way ANOVA.
1650 **(F)** Invasion assays of untagged TIR1, CDPK1-AID, and AID-HOOK parasites treated auxin for
1651 40 hrs. Medians are plotted for $n = 3$ biological replicates (different shades of gray); n.s., $p >$
1652 0.05, Welch's *t*-test. **(G)** Parasite egress stimulated with zaprinast following treatment with auxin
1653 for 24 hrs. Egress was monitored by live microscopy. Percent egress plotted for $n = 3$ biological
1654 replicates, n.s., $p > 0.05$, Welch's *t*-test. **(H)** HOOK tagged with a C-terminal 3xHA in CDPK1
1655 cKD parasites (CDPK1-AID) visualized in fixed intracellular parasites by immunofluorescence as
1656 in D.
1657

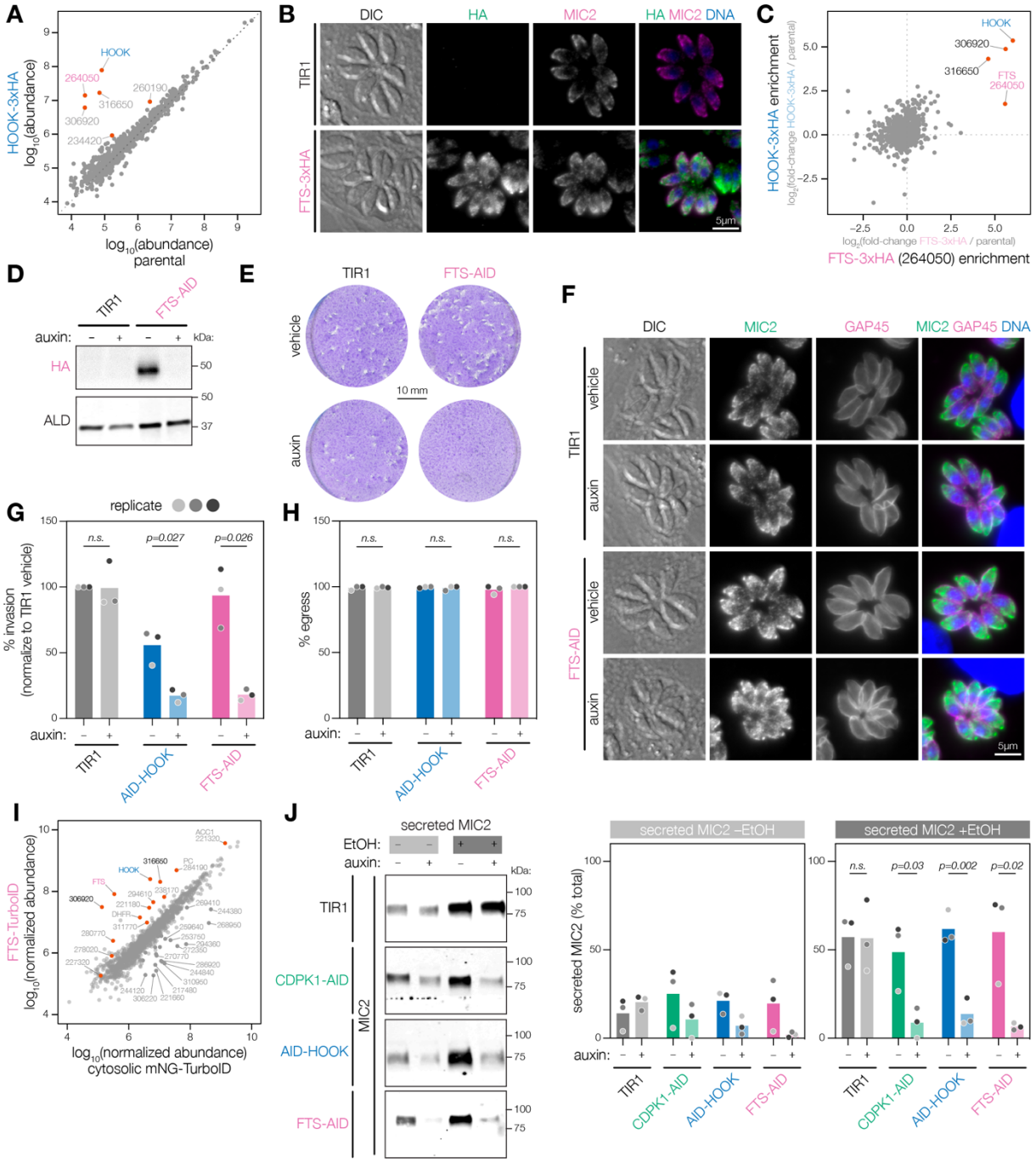

Figure 5. The HOOK complex is required for microneme exocytosis. (A) IP-MS of HOOK-3xHA or untagged parasites. Protein abundances determined by LC-MS/MS are shown for n = 3 biological replicates. Significantly enriched proteins (red) based on more than 3 unique peptides and $p < 0.05$; ANOVA and Benjamini-Hochberg corrected. **(B)** FTS-3xHA visualized in fixed intracellular parasites by immunofluorescence after treatment with auxin for 24 hrs. Hoechst and MIC2 are used as counterstains. **(C)** Reciprocal IP-MS of HOOK-3xHA and FTS-3xHA. FTS is tagged with a C-terminal 3xHA epitope at the endogenous locus (FTS-3xHA). IP enrichment is shown as the fold-change of protein abundances in tagged versus untagged

1667 strains determined by LC-MS/MS across n = 3 biological replicates. Significantly enriched
1668 proteins (red), for proteins with more than 3 unique peptides, $p_{HOOK} < 0.05$, and $p_{FTS} < 0.05$;
1669 ANOVA and Benjamini-Hochberg corrected. **(D)** Immunoblot of FTS cKD parasites. FTS is
1670 tagged with an C-terminal mAID-HA at its endogenous locus (FTS-AID) and treated with auxin
1671 for 40 hrs. ALD is used as a loading control. **(E)** Plaque assays of host cells infected with TIR1
1672 or FTS-AID parasites for 8 days in auxin. Host cells are stained with crystal violet. **(F)** Micronemes
1673 are visualized in fixed intracellular FTS-AID and TIR1 parasites by immunofluorescence after
1674 treatment auxin for 24 hrs. Hoechst and GAP45 are used as counterstains. **(G)** Invasion assays
1675 of untagged TIR1, AID-HOOK, and FTS-AID parasites treated auxin for 40 hrs. Medians are
1676 plotted for n = 3 biological replicates (different shades of gray), n.s., $p > 0.05$, Welch's t-test. **(H)**
1677 Parasite egress stimulated zaprinast following auxin treatment for 24 hrs. Egress was monitored
1678 by live microscopy. Percent egress plotted for n = 3 biological replicates, n.s., $p > 0.05$, Welch's
1679 t-test. **(I)** Proximity labeling MS of FTS using TurboID (FTS-TurboID) compared to a cytosolic
1680 TurboID control (cytosolic mNeonGreen-TurboID). Protein abundances determined by LC-
1681 MS/MS are shown for n = 3 biological replicates. Significantly enriched proteins in FTS-TurboID
1682 are colored in red (red and blue), unique peptides > 3, ratio > 1, $p < 0.05$, ANOVA and Benjamini-
1683 Hochberg corrected. **(J)** Microneme protein secretion assays of parasites treated with auxin for
1684 40 hrs. Extracellular parasites are stimulated with 1% ethanol (EtOH) and 3% IFS for 1.5 hrs.
1685 Percent MIC2 secreted is plotted for n = 3 biological replicates, n.s., $p > 0.05$, Welch's t-test.
1686

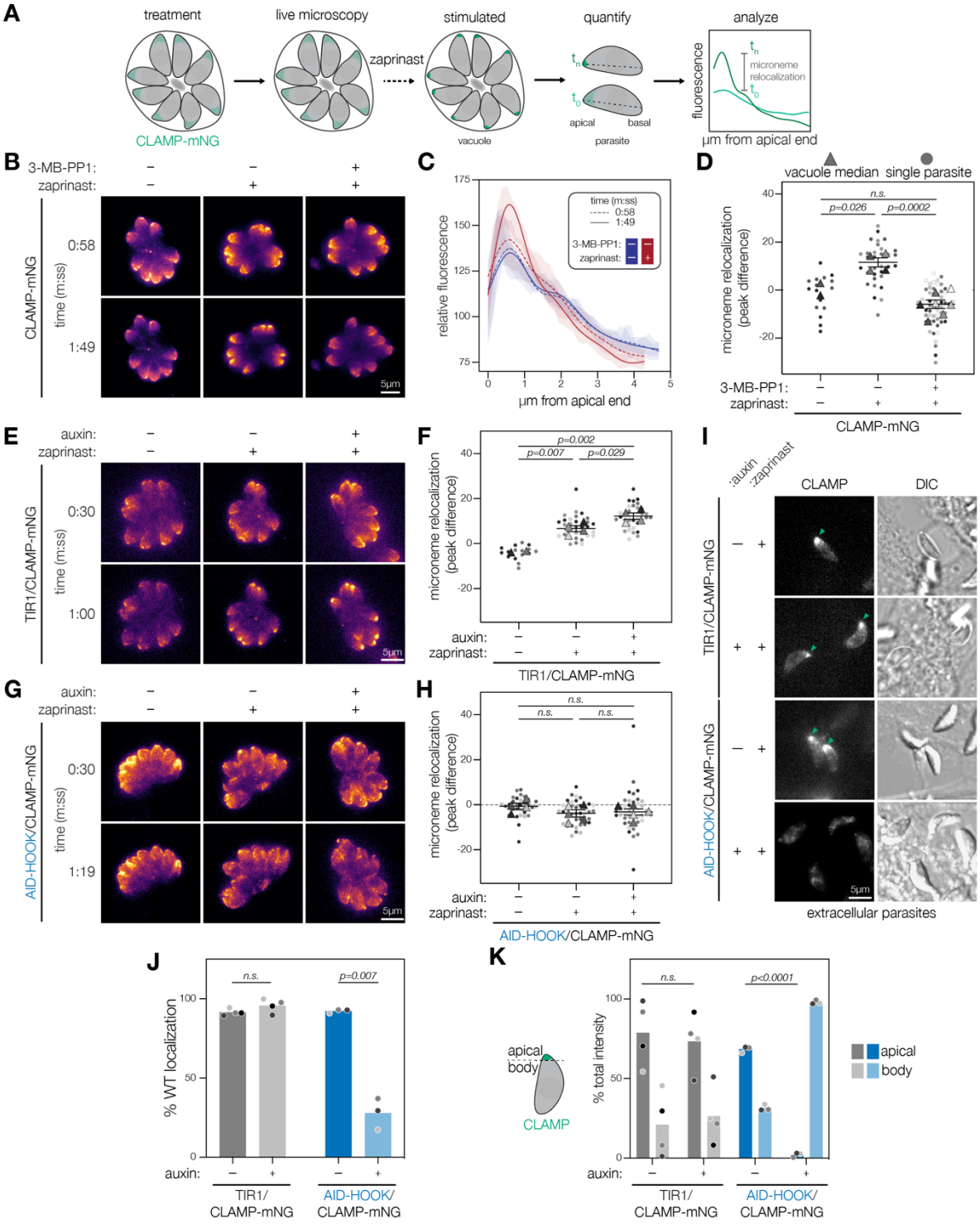

Figure 6. CDPK1 activity and HOOK are required for microneme trafficking during parasite motility stages. (A) Schematic to analyze microneme trafficking during parasite motile stages. Intracellular parasites expressing microneme protein CLAMP endogenously tagged with mNeonGreen (CLAMP-mNG). Parasites are treated either with 3-MB-PP1 (inhibit CDPK1) or auxin (for conditional knockdown). Live microscopy was performed to detect CLAMP-mNG signal over time. Zaprinast was added at 1 min or 30 sec to stimulate microneme relocalization

1694 to the apical end of the parasite. Fluorescence intensities across the apical-basal axis of each
1695 individual parasite within a vacuole was measured across time. Microneme relocalization was
1696 quantified by calculating the difference of maximum CLAMP intensity between time points
1697 preceding drug addition and egress. **(B)** Maximum intensity projections at single time points of
1698 CLAMP-mNG parasites treated with 3 μM 3-MB-PP1 or vehicle and zaprinast. **(C)** Relative
1699 fluorescence intensity of CLAMP-mNG signal across the apical-basal axis of parasites in B.
1700 Zaprinast (red) or vehicle (blue). Splines mean intensity for all parasites in each vacuole are shown
1701 with SD shaded. **(D)** Microneme relocalization. SuperPlots showing vacuole median peak
1702 differences are displayed as triangles. Individual parasites are displayed as circles. Replicates
1703 are differentially shaded, n.s., $p > 0.05$, unpaired *t*-test. **(E)** Maximum intensity projections at
1704 single time points of TIR1/CLAMP-mNG parasites treated with auxin and stimulated with
1705 zaprinast. **(F)** Microneme relocalization was quantified for TIR1/CLAMP-mNG parasites as in D.
1706 **(G)** Maximum intensity projections at single time points of AID-HOOK/CLAMP-mNG parasites
1707 treated auxin and stimulated with zaprinast. **(H)** Microneme relocalization was quantified for AID-
1708 HOOK/CLAMP-mNG parasites as in D. **(I)** Maximum intensity projections of extracellular
1709 TIR1/CLAMP-mNG and AID-HOOK/CLAMP-mNG parasites. **(J)** Percent of extracellular
1710 parasites in I with WT CLAMP-mNG localization, n.s., $p > 0.05$, Welch's *t*-test. **(K)** Percent total
1711 CLAMP-mNG signal intensity in the apical versus body of extracellular parasites, n.s., $p > 0.05$,
1712 Welch's *t*-test.
1713

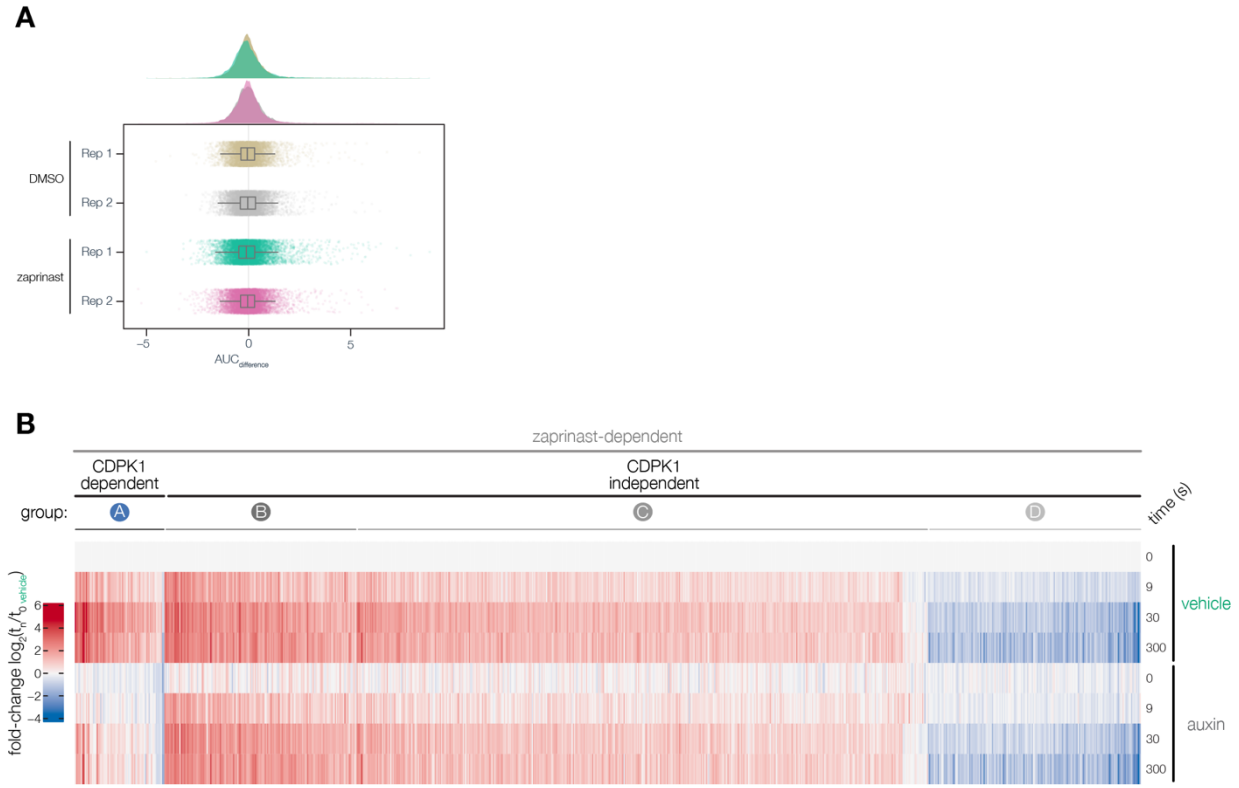

Figure 1—figure supplement 1. Zaprinast-dependent phosphoproteome. (A) Distribution of $AUC_{difference}$ values for individual peptides in the enriched DMSO phosphoproteome and enriched zaprinast phosphoproteome across two biological replicates. **(B)** Heatmap of zaprinast-dependent phosphopeptide abundance ratios across time relative to the vehicle t_0 interval during auxin or vehicle treatment. Peptides are organized by CDPK1-dependent phosphopeptides (Group A) and CDPK1-independent phosphopeptides (Group B, C, D).

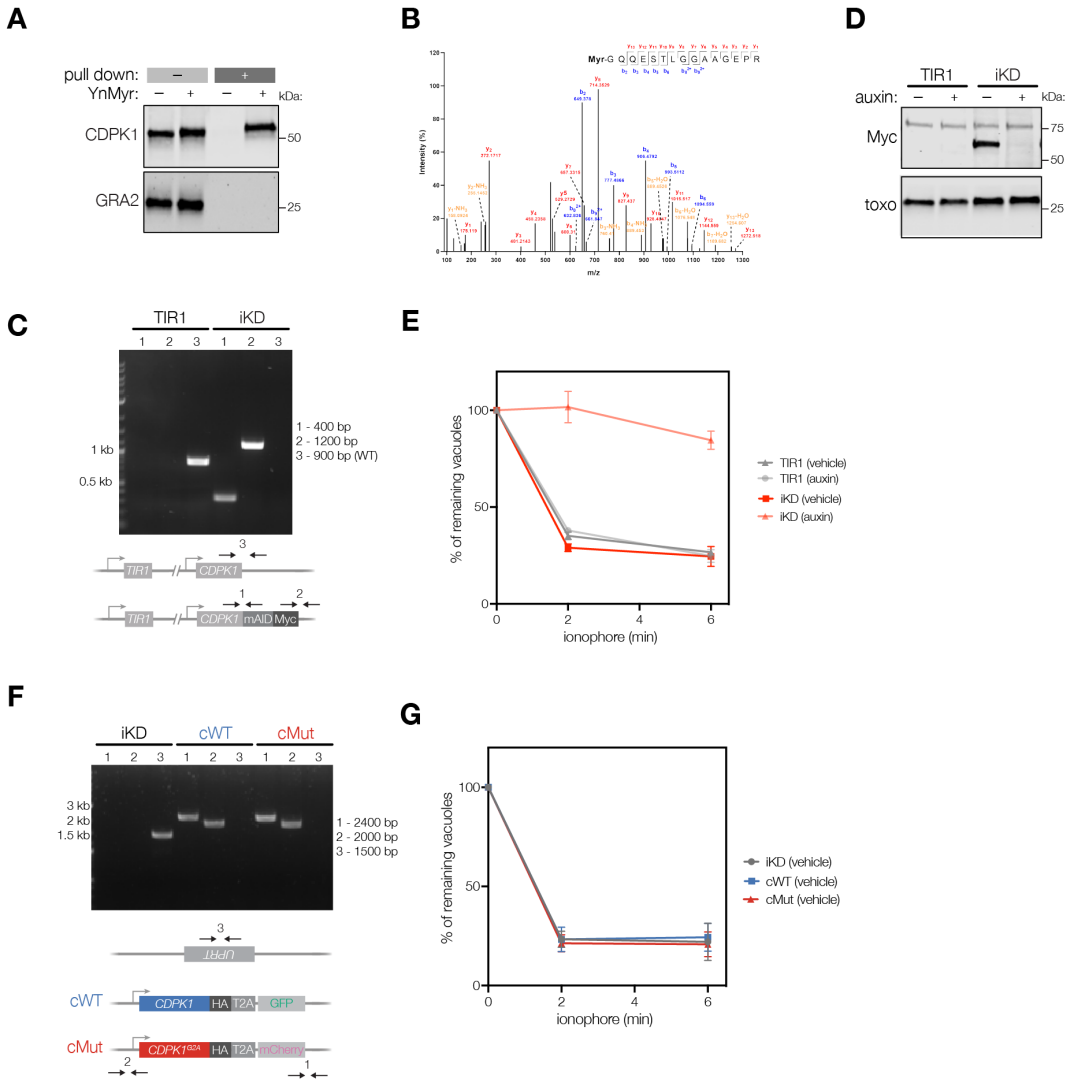

Figure 2—figure supplement 1. CDPK1 myristoylation, inducible knockdown, and complementation. (A) YnMyr-dependent pull down confirming myristoylation of CDPK1. GRA2 antibody was used as a loading control. **(B)** MS2 fragmentation spectra indicating myristoylation of Gly2 of CDPK1 after YnMyr-dependent pull down. **(C)** PCR analysis confirming correct integration of the mAID cassette at the C terminus of endogenous *CDPK1* in the TIR1 line. **(D)** Immunoblot validation of auxin-dependent depletion of CDPK1 in the iKD line using the anti-Myc antibody and the anti-toxo antibody as a loading control. The band at 75 kDa represents anti-Myc-related background. **(E)** Conditional depletion of CDPK1 abolishes ionophore-induced egress from host cells. Intracellular parasites were treated with auxin or vehicle (EtOH) for 2 hrs and egress was initiated by addition of 8 µM A23187. The number of intact vacuoles was monitored over the course of 6 min. Each data point is an average of two biological replicates, each in technical triplicate, error bars represent standard deviation. **(F)** PCR analysis confirming correct integration of the complementation constructs encoding the WT (cWT) and myristoylation mutant (cMut) copies of *CDPK1* at the *UPRT* locus of the iKD line. Primers are indicated by arrows. Base pairs (bp). **(G)** In the absence of auxin, both cWT and cMut parasites egress from host cells within 2 min post-ionophore treatment.

A

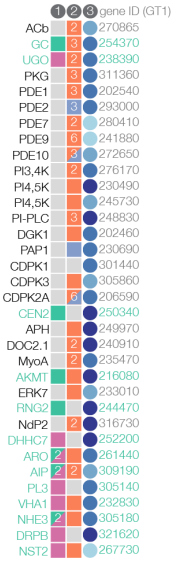

Figure 3—figure supplement 1. Factors controlling parasite motility. (A) Expanded list of factors involved in parasite motile stages from Fig. 3H.

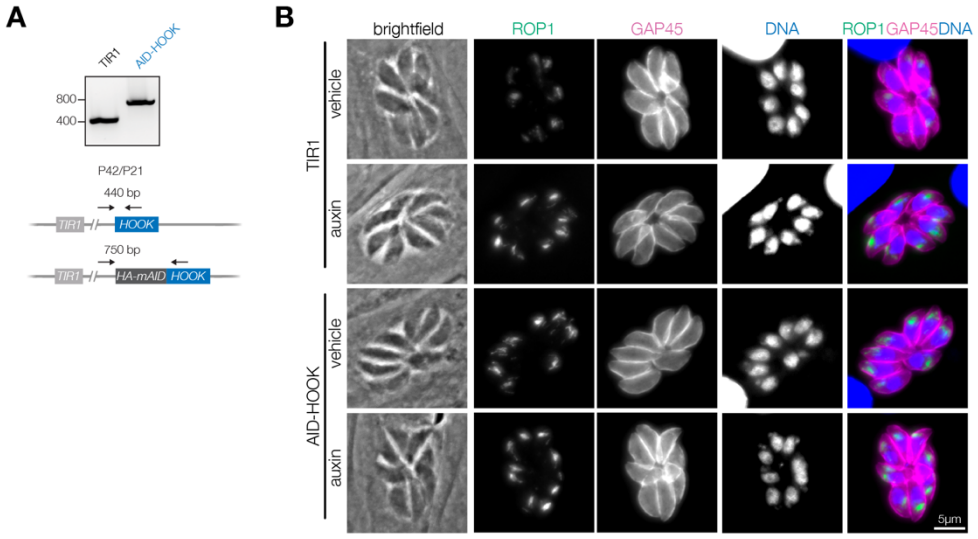

Figure 4—figure supplement 1. Extended analysis of HOOK knockdown. (A) PCR analysis confirming correct integration of the HA-mAID cassette at the N terminus of endogenous *HOOK* (*TGGT1_289100*) in the TIR1 line. **(B)** Rhoptries (ROP1) are visualized in fixed intracellular parasites by immunofluorescence after treatment with auxin for 24 hrs. Hoechst and GAP45 are used as counterstains.

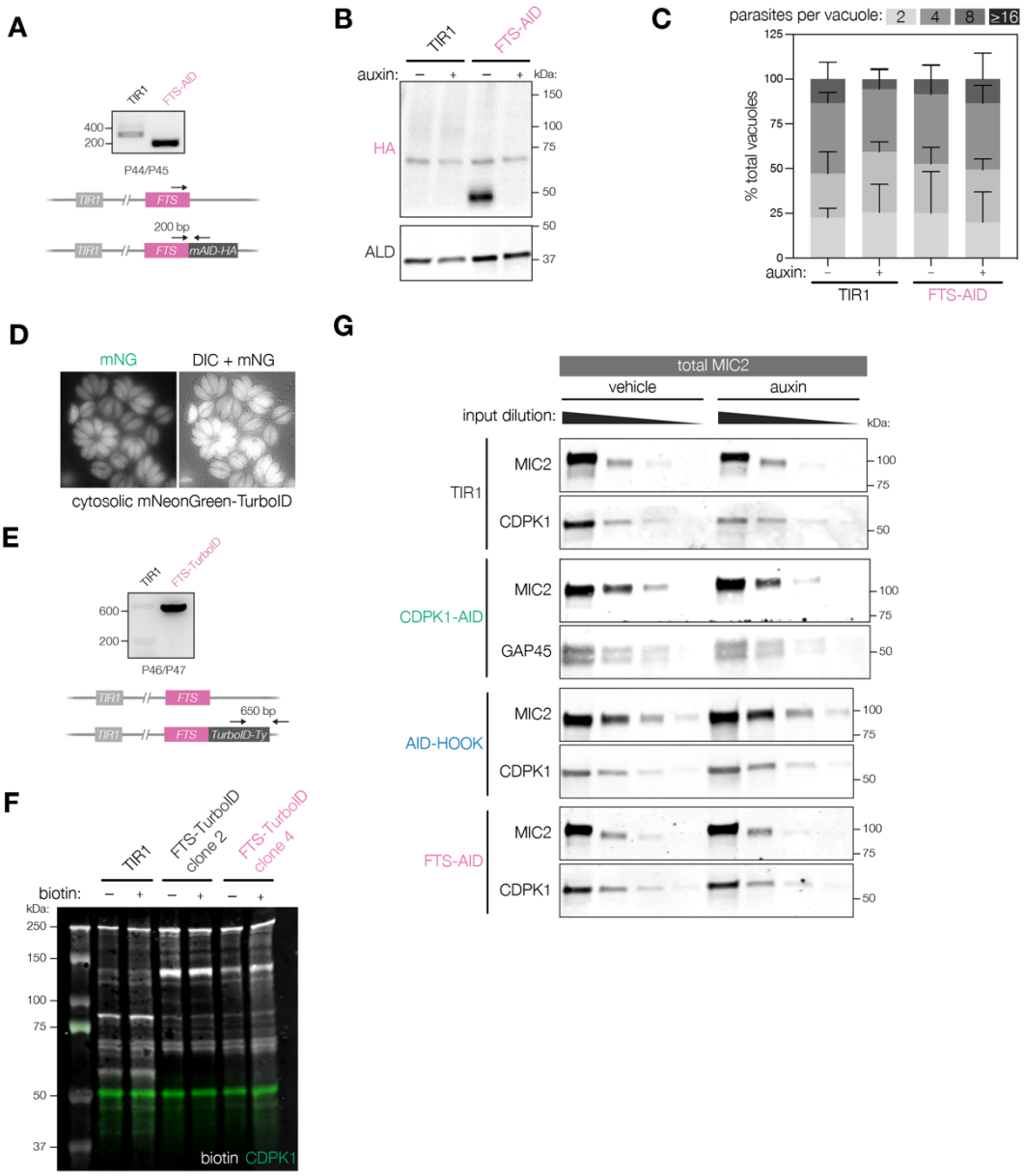

Figure 5—figure supplement 1. Extended analysis of FTS knockdown, proximity labeling, and microneme protein secretion. (A) PCR analysis confirming correct integration of the mAID-HA cassette at the C terminus of endogenous *FTS* (*TGGT1_264050*) in the TIR1 line. **(B)** Uncropped immunoblot shown in Figure 5D confirming C-terminal tagging of FTS. The band at ~70 kDa represents anti-HA/anti-ALD-related background present in all conditions. © Replication assays of host cells infected with TIR1 or FTS-AID parasites in auxin for 24 hrs. Parasites per vacuole were quantified from immunofluorescence on fixed intracellular parasites. $p > 0.9$. Two-way ANOVA. **(D)** Live microscopy of HFFs infected with parasites expressing cytosolic mNeonGreen-TurboID as the cytosolic control for proximity labeling. **(E)** PCR analysis confirming presence of TurboID-Ty cassette in the TIR1 line. **(F)** Immunoblot detection of biotinylated proteins in FTS-TurboID and cytosolic mNG-TurboID parasites treated with 500 µM of biotin or a vehicle of DMSO. Biotinylated proteins detected with a labeled streptavidin. anti-CDPK1 antibody was used as a loading control. **(G)** Serial dilution of total parasite lysate for cKD

1764 strains for TIR1, CDPK1, HOOK, and FTS used in microneme protein secretion assays in Figure
1765 5J to generate standard curves.
1766

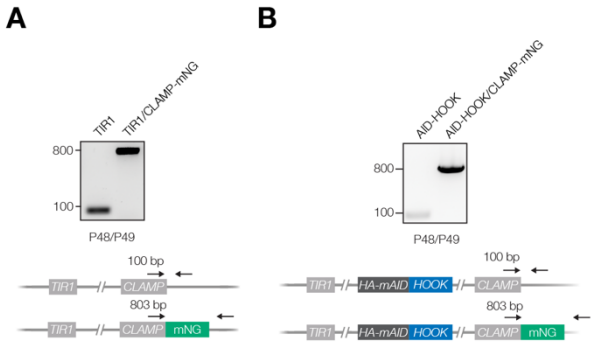

Figure 6—figure supplement 1. Extended analysis of FTS knockdown, proximity labeling, and microneme protein secretion. (A) PCR analysis confirming correct integration of the mNeonGreen reporter at the C terminus of endogenous *CLAMP* (*TGGT1_265790*) in the TIR1 line. **(B)** PCR analysis confirming correct integration of the mNeonGreen reporter at the C terminus of endogenous *CLAMP* in the AID-HOOK line.

1774 ## SUPPLEMENTARY FILES

1775 **Video 1.** Representative image series of parasites expressing endogenously tagged CLAMP-
1776 mNG following pre-treatment with DMSO and stimulation with DMSO.
1777 **Video 2.** Representative image series of parasites expressing endogenously tagged CLAMP-
1778 mNG following pre-treatment with DMSO and stimulation with 500 μM zaprinast.
1779 **Video 3.** Representative image series of parasites expressing endogenously tagged CLAMP-
1780 mNG following pre-treatment with 3 μM 3-MB-PP1 and stimulation with 500 μM zaprinast.
1781 **Video 4.** Representative image series of parasites expressing endogenously tagged
1782 TIR1/CLAMP-mNG following pre-treatment with vehicle and stimulation with DMSO.
1783 **Video 5.** Representative image series of parasites expressing endogenously tagged
1784 TIR1/CLAMP-mNG following pretreatment with vehicle and stimulation with 500 μM zaprinast.
1785 **Video 6.** Representative image series of parasites expressing endogenously tagged
1786 TIR1/CLAMP-mNG following pre-treatment with auxin and stimulation with 500 μM zaprinast.
1787 **Video 7.** Representative image series of parasites expressing endogenously tagged AID-
1788 HOOK/CLAMP-mNG following pre-treatment with vehicle and stimulation with DMSO.
1789 **Video 8.** Representative image series of parasites expressing endogenously tagged AID-
1790 HOOK/CLAMP-mNG following pretreatment with vehicle and stimulation with 500 μM
1791 zaprinast.
1792 **Video 9.** Representative image series of parasites expressing endogenously tagged AID-
1793 HOOK/CLAMP-mNG following pre-treatment with auxin and stimulation with 500 μM zaprinast.
1794 **Supplementary file 1.** Sub-minute phosphoproteomics time course peptide and abundance
1795 assignments from Proteome Discoverer 2.4 and analysis for the zaprinast enriched samples.
1796 Supplementary file 1.1. RAW peptide and abundance assignments.
1797 Supplementary file 1.2. Replicate 1 analysis with $AUC_{difference}$ and p values.
1798 Supplementary file 1.3. Replicate 2 analysis with $AUC_{difference}$ and p values.
1799 Supplementary file 1.4. Replicate 1 and 2 analysis with $AUC_{vehicle}$ values for CDPK1-
1800 independent phosphorylation.
1801 Supplementary file 1.5. Group assignments for zaprinast-dependent phosphopeptides.
1802 **Supplementary file 2.** Sub-minute phosphoproteomics time course protein and abundance
1803 assignments from Proteome Discoverer 2.4 for the zaprinast proteome.
1804 **Supplementary file 3.** Sub-minute phosphoproteomics time course peptide and abundance
1805 assignments from Proteome Discoverer 2.4 and analysis for the DMSO enriched samples.
1806 Supplementary file 3.1. RAW peptide and abundance assignments.
1807 Supplementary file 3.2. Replicate 1 analysis with $AUC_{difference}$ values.
1808 Supplementary file 3.3. Replicate 2 analysis with $AUC_{difference}$ values.
1809 Supplementary file 3.4. Replicate 1 and 2 analysis with $AUC_{vehicle}$ values for CDPK1-
1810 independent phosphorylation.
1811 **Supplementary file 4.** Sub-minute phosphoproteomics time course protein and abundance
1812 assignments from Proteome Discoverer 2.4 for the DMSO proteome.
1813 **Supplementary file 5.** CDPK1 immunoprecipitation protein and abundance assignments from
1814 Scaffold DIA.
1815 **Supplementary file 6.** Thiophosphorylation of CDPK1 substrates. Peptide and abundance
1816 assignments from Proteome Discoverer 2.4 and analysis.
1817 Supplementary file 6.1. RAW peptide and abundance assignments.

Supplementary file 6.2. Analyzed peptides with enrichment significance values.
Supplementary file 6.3. Analyzed flowthrough peptides used for normalization.

Supplementary file 7. Thiophosphorylation of CDPK1 substrates. Protein and abundance assignments from Proteome Discoverer 2.4 and analysis.

Supplementary file 8. HOOK and FTS immunoprecipitation protein and abundance assignments from Proteome Discoverer 2.4.

Supplementary file 9. FTS proximity labeling protein and abundance assignments from Proteome Discoverer 2.4.

Supplementary file 10. Sequences and accessions of oligonucleotides and plasmids used in this study.

SOURCE DATA

Figure 2—source data 1. This file contains source data that was used to generate the blot in Figure 2. Myc, LICOR. Figure 2B.

Figure 2—source data 2. This file contains source data that was used to generate the blot in Figure 2. HA, LICOR. Figure 2B.

Figure 2—source data 3. This file contains source data that was used to generate the blot in Figure 2. toxo, LICOR. Figure 2B.

Figure 2—source data 4. This file contains source data that was used to generate the blot in Figure 2. HA, LICOR. Figure 2C.

Figure 2—source data 5. This file contains source data that was used to generate the blot in Figure 2. Myc, LICOR. Figure 2C.

Figure 2—source data 6. This file contains source data that was used to generate the blot in Figure 2. toxo, LICOR. Figure 2C.

Figure 2—source data 7. This file contains source data that was used to generate the blot in Figure 2. CDPK1, GFP, LICOR. Figure 2E.

Figure 2—source data 8. This file contains source data that was used to generate the blot in Figure 2. GAP45, SAG1, LICOR. Figure 2E.

Figure 2—source data 9. This file contains source data that was used to generate the blot in Figure 2. HA, LICOR. Figure 2F.

Figure 2—source data 10. This file contains source data that was used to generate the blot in Figure 2. toxo, LICOR. Figure 2F.

Figure 2—source data 11. This file contains source data that was used to generate the blot in Figure 2. GFP, LICOR. Figure 2F.

Figure 2—source data 12. This file contains source data that was used to generate the blot in Figure 2. mCherry, LICOR. Figure 2F.

Figure 2—source data 13. This file contains the annotated source data that were used to generate blots in Figure 2.

Figure 2—source data 14. This file contains source data that was used to make the graph presented in Figure 2. GraphPad Prism data for Figure 2H.

Figure 3—source data 1. This file contains source data that was used to generate the blot in Figure 3. Thiophosphate ester, LICOR 700 channel.

Figure 3—source data 2. This file contains source data that was used to generate the blot in Figure 3. Thiophosphate ester, LICOR 700 channel.

Figure 3—source data 3. This file contains source data that was used to generate the blot in Figure 3. TUB1, LICOR 800 channel.

Figure 3—source data 4. This file contains the annotated source data that were used to generate blots in Figure 3.
Figure 4—source data 1. This file contains source data that was used to generate the blot in Figure 4. HA-AID-HOOK, chemiluminescence.
Figure 4—source data 2. This file contains source data that was used to generate the blot in Figure 4. HA-AID-HOOK, colorimetric, ladder.
Figure 4—source data 3. This file contains source data that was used to generate the blot in Figure 4. CDPK1, LICOR 700 channel.
Figure 4—source data 4. This file contains the annotated source data that were used to generate blots in Figure 4.
Figure 4—source data 5. This file contains source data that was used to make the graph presented in Figure 4. GraphPad Prism data for Figure 4E.
Figure 4—source data 6. This file contains source data that was used to make the graph presented in Figure 4. GraphPad Prism data for Figure 4F.
Figure 4—source data 7. This file contains source data that was used to make the graph presented in Figure 4 and Figure 5. GraphPad Prism data for Figure 4G and 5H.
Figure 5—source data 1. This file contains source data that was used to generate the blot in Figure 5. FTS-AID-HA, chemiluminescence.
Figure 5—source data 2. This file contains source data that was used to generate the blot in Figure 5. FTS-AID-HA, colorimetric, ladder.
Figure 5—source data 3. This file contains source data that was used to generate the blot in Figure 5. ALD, LICOR 700 channel.
Figure 5—source data 4. This file contains source data that was used to generate the blot in Figure 5 and Figure 5—figure supplement 1. MIC2, LICOR 800 channel. (TIR1).
Figure 5—source data 5. This file contains source data that was used to generate the blot in Figure 5 and Figure 5—figure supplement 1. MIC2, LICOR 800 channel. (CDPK1-AID).
Figure 5—source data 6. This file contains source data that was used to generate the blot in Figure 5 and Figure 5—figure supplement 1. MIC2, LICOR 800 channel. (AID-HOOK).
Figure 5—source data 7. This file contains source data that was used to generate the blot in Figure 5 and Figure 5—figure supplement 1. MIC2, LICOR 800 channel. (FTS-AID).
Figure 5—source data 8. This file contains the annotated source data that were used to generate blots in Figure 5.
Figure 5—source data 9. This file contains source data that was used to make the graph presented in Figure 5. GraphPad Prism data for Figure 5G.
Figure 5—source data 10. This file contains source data that was used to make the graphs presented in Figure 5. GraphPad Prism data for Figure 5J.
Figure 6—source data 1. This file contains source data that was used to make the graph presented in Figure 6. GraphPad Prism data for Figure 5C.
Figure 6—source data 2. This file contains source data that was used to make the graph presented in Figure 6. GraphPad Prism data for Figure 5D.
Figure 6—source data 3. This file contains source data that was used to make the graph presented in Figure 6. GraphPad Prism data for Figure 5F.
Figure 6—source data 4. This file contains source data that was used to make the graph presented in Figure 6. GraphPad Prism data for Figure 5H.
Figure 6—source data 5. This file contains source data that was used to make the graph presented in Figure 6. GraphPad Prism data for Figure 5J.
Figure 6—source data 6. This file contains source data that was used to make the graph presented in Figure 6. GraphPad Prism data for Figure 5K.

Figure 2—figure supplement 1—source data 1. This file contains source data that was used to generate the blot in Figure 2—figure supplement 1. CDPK1, LICOR.
Figure 2—figure supplement 1—source data 2. This file contains source data that was used to generate the blot in Figure 2—figure supplement 1. GRA2, LICOR.
Figure 2—figure supplement 1—source data 3. This file contains source data that was used to generate the blot in Figure 2—figure supplement 1. Myc, LICOR.
Figure 2—figure supplement 1—source data 4. This file contains source data that was used to generate the blot in Figure 2—figure supplement 1. toxo, LICOR.
Figure 2—figure supplement 1—source data 5. This file contains source data that was used to generate the DNA gel in Figure 2—figure supplement 1. iKD integration.
Figure 2—figure supplement 1—source data 6. This file contains source data that was used to generate the DNA gel in Figure 2—figure supplement 1. cWT, cMut integration.
Figure 2—figure supplement 1—source data 7. This file contains the annotated source data that were used to generate blots in Figure 2—figure supplement 1.
Figure 2—figure supplement 1—source data 8. This file contains source data that was used to make the graph presented in Figure 2. GraphPad Prism data for Figure 2—figure supplement 1E.
Figure 2—figure supplement 1—source data 9. This file contains source data that was used to make the graph presented in Figure 2. GraphPad Prism data for Figure 2—figure supplement 1G.
Figure 4—figure supplement 1—source data 1. This file contains source data that was used to generate the DNA gel in Figure 4—figure supplement 1. AID-HOOK integration.
Figure 4—figure supplement 1—source data 2. This file contains the annotated source data that were used to generate blots in Figure 4—figure supplement 1.
Figure 5—figure supplement 1—source data 1. This file contains source data that was used to generate the DNA gel in Figure 5—figure supplement 1. FTS-AID integration.
Figure 5—figure supplement 1—source data 2. This file contains source data that was used to generate the DNA gel in Figure 5—figure supplement 1. FTS-TurboID tag.
Figure 5—figure supplement 1—source data 3. This file contains source data that was used to generate the blot in Figure 5—figure supplement 1. Biotin, LICOR 700 channel.
Figure 5—figure supplement 1—source data 4. This file contains source data that was used to generate the blot in Figure 5—figure supplement 1. CDPK1, LICOR 800 channel.
Figure 5—figure supplement 1—source data 5. This file contains source data that was used to generate the blot in Figure 5—figure supplement 1. CDPK1, LICOR 700 channel. (TIR1 standard).
Figure 5—figure supplement 1—source data 6. This file contains source data that was used to generate the blot in Figure 5—figure supplement 1. GAP45, LICOR 700 channel. (CDPK1-AID standard).
Figure 5—figure supplement 1—source data 7. This file contains source data that was used to generate the blot in Figure 5—figure supplement 1. CDPK1, LICOR 700 channel. (AID-HOOK standard).
Figure 5—figure supplement 1—source data 8. This file contains source data that was used to generate the blot in Figure 5—figure supplement 1. CDPK1, LICOR 700 channel. (FTS-AID standard).
Figure 5—figure supplement 1—source data 9. This file contains the annotated source data that were used to generate blots in Figure 5—figure supplement 1. CDPK1, LICOR 700 channel. (FTS-AID standard).

Figure 5—figure supplement 1—source data 10. This file contains source data that was used to make the graph presented in Figure 5—figure supplement 1. GraphPad Prism data for Figure 5—figure supplement 1C.

Figure 6—figure supplement 1—source data 1. This file contains source data that was used to generate the DNA gel in Figure 6—figure supplement 1. CLAMP-mNeonGreen integration. (TIR1/CLAMP-mNG).

Figure 6—figure supplement 1—source data 2. This file contains source data that was used to generate the DNA gel in Figure 6—figure supplement 1. CLAMP-mNeonGreen integration. (AID-HOOK/CLAMP-mNG).

Figure 6—figure supplement 1—source data 3. This file contains the annotated source data that were used to generate blots in Figure 6—figure supplement 1.

MATERIALS AVAILABILITY STATEMENT

Proteomics data will be deposited in ProteomeXchange Consortium via the PRIDE partner repository. Accession numbers will be listed in the appropriate Methods section. The sequences of cloning vectors generated for this study have been or will be deposited in GenBank, as listed in **Supplementary File 10**. Custom analysis scripts in the R computing language are available upon request. Strains generated for this study are available upon request.

REFERENCES

Alam MM, Solyakov L, Bottrill AR, Flueck C, Siddiqui FA, Singh S, Mistry S, Viskaduraki M, Lee K, Hopp CS, Chitnis CE, Doerig C, Moon RW, Green JL, Holder AA, Baker DA, Tobin AB. 2015. Phosphoproteomics reveals malaria parasite Protein Kinase G as a signalling hub regulating egress and invasion. *Nat Commun* **6**:7285.

Aquilini E, Cova MM, Mageswaran SK, Dos Santos Pacheco N, Sparvoli D, Penarete-Vargas DM, Najm R, Graindorge A, Suarez C, Maynadier M, Berry-Sterkers L, Urbach S, Fahy PR, Guérin AN, Striepen B, Dubremetz J-F, Chang Y-W, Turkewitz AP, Lebrun M. 2021. An Alveolata secretory machinery adapted to parasite host cell invasion. *Nat Microbiol* **6**:425–434.

Bandini G, Leon DR, Hoppe CM, Zhang Y, Agop-Nersesian C, Shears MJ, Mahal LK, Routier FH, Costello CE, Samuelson J. 2019. O-Fucosylation of thrombospondin-like repeats is required for processing of microneme protein 2 and for efficient host cell invasion by Toxoplasma gondii tachyzoites. *J Biol Chem* **294**:1967–1983.

Barylyuk K, Koreny L, Ke H, Butterworth S, Crook OM, Lassadi I, Gupta V, Tromer E, Mourier T, Stevens TJ, Breckels LM, Pain A, Lilley KS, Waller RF. 2020. A Comprehensive Subcellular Atlas of the Toxoplasma Proteome via hyperLOPIT Provides Spatial Context for Protein Functions. *Cell Host Microbe* **28**:752–766.e9.

Beck JR, Fung C, Straub KW, Coppens I, Vashisht AA, Wohlschlegel JA, Bradley PJ. 2013. A Toxoplasma palmitoyl acyl transferase and the palmitoylated armadillo repeat protein TgARO govern apical rhoptry tethering and reveal a critical role for the rhoptries in host cell invasion but not egress. *PLoS Pathog* **9**:e1003162.

Bekker-Jensen DB, Martínez-Val A, Steigerwald S, Rüther P, Fort KL, Arrey TN, Harder A, Makarov A, Olsen JV. 2020. A Compact Quadrupole-Orbitrap Mass Spectrometer with FAIMS Interface Improves Proteome Coverage in Short LC Gradients. *Mol Cell Proteomics* **19**:716–729.

2004 Ben Chaabene R, Lentini G, Soldati-Favre D. 2021. Biogenesis and discharge of the rhoptries:
2005 Key organelles for entry and hijack of host cells by the Apicomplexa. *Mol Microbiol*
2006 **115**:453–465.
2007 Berg S, Kutra D, Kroeger T, Straehle CN, Kausler BX, Haubold C, Schiegg M, Ales J, Beier T,
2008 Rudy M, Eren K, Cervantes JI, Xu B, Beuttenmueller F, Wolny A, Zhang C, Koethe U,
2009 Hamprecht FA, Kreshuk A. 2019. ilastik: interactive machine learning for (bio)image
2010 analysis. *Nat Methods* **16**:1226–1232.
2011 Bielska E, Schuster M, Roger Y, Berepiki A, Soanes DM, Talbot NJ, Steinberg G. 2014. Hook is
2012 an adapter that coordinates kinesin-3 and dynein cargo attachment on early endosomes. *J*
2013 *Cell Biol* **204**:989–1007.
2014 Billker O, Lourido S, Sibley LD. 2009. Calcium-dependent signaling and kinases in
2015 apicomplexan parasites. *Cell Host Microbe* **5**:612–622.
2016 Bisio H, Lunghi M, Brochet M, Soldati-Favre D. 2019. Phosphatidic acid governs natural egress
2017 in Toxoplasma gondii via a guanylate cyclase receptor platform. *Nat Microbiol* **4**:420–428.
2018 Bisio H, Soldati-Favre D. 2019. Signaling Cascades Governing Entry into and Exit from Host
2019 Cells by Toxoplasma gondii. *Annu Rev Microbiol* **73**:579–599.
2020 Blader I, Coleman B, Chen C, Gubbels M, Hill C. 2016. The lytic cycle of Toxoplasma gondii:
2021 15 years later, 463-485.
2022 Blader IJ, Coleman BI, Chen C-T, Gubbels M-J. 2015. Lytic Cycle of Toxoplasma gondii: 15
2023 Years Later. *Annu Rev Microbiol* **69**:463–485.
2024 Blethrow JD, Glavy JS, Morgan DO, Shokat KM. 2008. Covalent capture of kinase-specific
2025 phosphopeptides reveals Cdk1-cyclin B substrates. *Proc Natl Acad Sci U S A* **105**:1442–
2026 1447.
2027 Blomqvist K, Helmel M, Wang C, Absalon S, Labunska T, Rudlaff RM, Adapa S, Jiang R, Steen
2028 H, Dvorin JD. 2020. Influence of Plasmodium falciparum Calcium-Dependent Protein
2029 Kinase 5 (PfCDPK5) on the Late Schizont Stage Phosphoproteome. *mSphere*.
2030 doi:10.1128/msphere.00921-19
2031 Bradley PJ, Sibley LD. 2007. Rhoptries: an arsenal of secreted virulence factors. *Curr Opin*
2032 *Microbiol* **10**:582–587.
2033 Branon TC, Bosch JA, Sanchez AD, Udeshi ND, Svinkina T, Carr SA, Feldman JL, Perrimon N,
2034 Ting AY. 2018. Efficient proximity labeling in living cells and organisms with TurboID. *Nat*
2035 *Biotechnol* **36**:880–887.
2036 Breinich MS, Ferguson DJP, Foth BJ, van Dooren GG, Lebrun M, Quon DV, Striepen B,
2037 Bradley PJ, Frischknecht F, Carruthers VB, Meissner M. 2009. A dynamin is required for
2038 the biogenesis of secretory organelles in Toxoplasma gondii. *Curr Biol* **19**:277–286.
2039 Brenes A, Hukelmann J, Bensaddek D, Lamond AI. 2019. Multibatch TMT Reveals False
2040 Positives, Batch Effects and Missing Values. *Mol Cell Proteomics* **18**:1967–1980.
2041 Brochet M, Collins MO, Smith TK, Thompson E, Sebastian S, Volkmann K, Schwach F,
2042 Chappell L, Gomes AR, Berriman M, Rayner JC, Baker DA, Choudhary J, Billker O. 2014.
2043 Phosphoinositide Metabolism Links cGMP-Dependent Protein Kinase G to Essential Ca2+
2044 Signals at Key Decision Points in the Life Cycle of Malaria Parasites. *PLoS Biol*
2045 **12**:e1001806.
2046 Broncel M, Dominicus C, Vigetti L, Nofal SD, Bartlett EJ, Touquet B, Hunt A, Wallbank BA,
2047 Federico S, Matthews S, Young JC, Tate EW, Tardieux I, Treeck M. 2020. Profiling of
2048 myristoylation in Toxoplasma gondii reveals an N-myristoylated protein important for host
2049 cell penetration. *Elife* **9**. doi:10.7554/eLife.57861
2050 Brown KM, Long S, Sibley LD. 2018. Conditional Knockdown of Proteins Using Auxin-inducible
2051 Degron (AID) Fusions in Toxoplasma gondii. *Bio Protoc* **8**. doi:10.21769/BioProtoc.2728
2052 Brown KM, Long S, Sibley LD. 2017. Plasma Membrane Association by N-Acylation Governs

2053 PKG Function in Toxoplasma gondii. *MBio* **8**. doi:10.1128/mBio.00375-17
2054 Brown KM, Sibley LD. 2018. Essential cGMP Signaling in Toxoplasma Is Initiated by a Hybrid
2055 P-Type ATPase-Guanylate Cyclase. *Cell Host Microbe* **24**:804–816.e6.
2056 Buguliskis JS, Brossier F, Shuman J, Sibley LD. 2010. Rhomboid 4 (ROM4) affects the
2057 processing of surface adhesins and facilitates host cell invasion by Toxoplasma gondii.
2058 *PLoS Pathog* **6**:e1000858.
2059 Butler CL, Lucas O, Wuchty S, Xue B, Uversky VN, White M. 2014. Identifying novel cell cycle
2060 proteins in Apicomplexa parasites through co-expression decision analysis. *PLoS One*
2061 **9**:e97625.
2062 Carruthers VB, Giddings OK, Sibley LD. 1999a. Secretion of micronemal proteins is associated
2063 with toxoplasma invasion of host cells. *Cell Microbiol* **1**:225–235.
2064 Carruthers VB, Moreno SN, Sibley LD. 1999b. Ethanol and acetaldehyde elevate intracellular
2065 [Ca2+] and stimulate microneme discharge in Toxoplasma gondii. *Biochem J* **342 (Pt**
2066 **2)**:379–386.
2067 Carruthers VB, Sherman GD, Sibley LD. 2000. The Toxoplasma adhesive protein MIC2 is
2068 proteolytically processed at multiple sites by two parasite-derived proteases. *J Biol Chem*
2069 **275**:14346–14353.
2070 Carruthers VB, Sibley LD. 1997. Sequential protein secretion from three distinct organelles of
2071 Toxoplasma gondii accompanies invasion of human fibroblasts. *Eur J Cell Biol* **73**:114–
2072 123.
2073 Carruthers VB, Tomley FM. 2008. Microneme proteins in apicomplexans. *Subcell Biochem*
2074 **47**:33–45.
2075 Chambers MC, Maclean B, Burke R, Amodei D, Ruderman DL, Neumann S, Gatto L, Fischer B,
2076 Pratt B, Egertson J, Hoff K, Kessner D, Tasman N, Shulman N, Frewen B, Baker TA,
2077 Brusniak M-Y, Paulse C, Creasy D, Flashner L, Kani K, Moulding C, Seymour SL, Nuwaysir
2078 LM, Lefebvre B, Kuhlmann F, Roark J, Rainer P, Detlev S, Hemenway T, Huhmer A,
2079 Langridge J, Connolly B, Chadick T, Holly K, Eckels J, Deutsch EW, Moritz RL, Katz JE,
2080 Agus DB, MacCoss M, Tabb DL, Mallick P. 2012. A cross-platform toolkit for mass
2081 spectrometry and proteomics. *Nat Biotechnol* **30**:918–920.
2082 Chen C-T, Kelly M, Leon J de, Nwagbara B, Ebbert P, Ferguson DJP, Lowery LA, Morrissette
2083 N, Gubbels M-J. 2015. Compartmentalized Toxoplasma EB1 bundles spindle microtubules
2084 to secure accurate chromosome segregation. *Mol Biol Cell* **26**:4562–4576.
2085 Christensen JR, Kendrick AA, Truong JB, Aguilar-Maldonado A, Adani V, Dzieciatkowska M,
2086 Reck-Peterson SL. 2021. Cytoplasmic dynein-1 cargo diversity is mediated by the
2087 combinatorial assembly of FTS-Hook-FHIP complexes. *Elife* **10**. doi:10.7554/eLife.74538
2088 Coleman BI, Saha S, Sato S, Engelberg K, Ferguson DJP, Coppens I, Lodoen MB, Gubbels M-
2089 J. 2018. A Member of the Ferlin Calcium Sensor Family Is Essential for Toxoplasma gondii
2090 Rhoptry Secretion. *MBio* **9**. doi:10.1128/mBio.01510-18
2091 Courjol F, Mouveaux T, Lesage K, Saliou J-M, Werkmeister E, Bonabaud M, Rohmer M,
2092 Slomianny C, Lafont F, Gissot M. 2017. Characterization of a nuclear pore protein sheds
2093 light on the roles and composition of the Toxoplasma gondii nuclear pore complex. *Cell*
2094 *Mol Life Sci* **74**:2107–2125.
2095 Doggett JS, Ojo KK, Fan E, Maly DJ, Van Voorhis WC. 2014. Bumped kinase inhibitor 1294
2096 treats established Toxoplasma gondii infection. *Antimicrob Agents Chemother* **58**:3547–
2097 3549.
2098 Donald RGK, Zhong T, Wiersma H, Nare B, Yao D, Lee A, Allocco J, Liberator PA. 2006.
2099 Anticoccidial kinase inhibitors: identification of protein kinase targets secondary to cGMP-
2100 dependent protein kinase. *Mol Biochem Parasitol* **149**:86–98.

2101 Endo T, Sethi KK, Piekarski G. 1982. Toxoplasma gondii: Calcium Ionophore A23187-mediated
2102 exit of trophozoites from infected murine macrophages. *Exp Parasitol* **53**:179–188.
2103 Fang H, Klages N, Baechler B, Hillner E, Yu L, Pardo M, Choudhary J, Brochet M. 2017.
2104 Multiple short windows of calcium-dependent protein kinase 4 activity coordinate distinct
2105 cell cycle events during Plasmodium gametogenesis. *Elife* **6**. doi:10.7554/eLife.26524
2106 Farrell A, Thirugnanam S, Lorestani A, Dvorin JD, Eidell KP, Ferguson DJP, Anderson-White
2107 BR, Duraisingh MT, Marth GT, Gubbels M-J. 2012. A DOC2 protein identified by
2108 mutational profiling is essential for apicomplexan parasite exocytosis. *Science* **335**:218–
2109 221.
2110 Francia ME, Wicher S, Pace DA, Sullivan J, Moreno SNJ, Arrizabalaga G. 2011. A Toxoplasma
2111 gondii protein with homology to intracellular type Na^+/H^+ exchangers is important for
2112 osmoregulation and invasion. *Exp Cell Res* **317**:1382–1396.
2113 Gaji RY, Johnson DE, Treeck M, Wang M, Hudmon A, Arrizabalaga G. 2015. Phosphorylation
2114 of a Myosin Motor by TgCDPK3 Facilitates Rapid Initiation of Motility during Toxoplasma
2115 gondii egress. *PLoS Pathog* **11**:e1005268.
2116 Garrison E, Treeck M, Ehret E, Butz H, Garbuz T, Oswald BP, Settles M, Boothroyd J,
2117 Arrizabalaga G. 2012. A forward genetic screen reveals that calcium-dependent protein
2118 kinase 3 regulates egress in Toxoplasma. *PLoS Pathog* **8**:e1003049.
2119 Gillingham AK, Sinka R, Torres IL, Lilley KS, Munro S. 2014. Toward a comprehensive map of
2120 the effectors of rab GTPases. *Dev Cell* **31**:358–373.
2121 Guo X, Farías GG, Mattera R, Bonifacino JS. 2016. Rab5 and its effector FHF contribute to
2122 neuronal polarity through dynein-dependent retrieval of somatodendritic proteins from the
2123 axon. *Proc Natl Acad Sci U S A* **113**:E5318–27.
2124 Havelaar AH, Kirk MD, Torgerson PR, Gibb HJ, Hald T, Lake RJ, Praet N, Bellinger DC, de Silva
2125 NR, Gargouri N, Speybroeck N, Cawthorne A, Mathers C, Stein C, Angulo FJ,
2126 Devleesschauwer B, World Health Organization Foodborne Disease Burden Epidemiology
2127 Reference Group. 2015. World Health Organization Global Estimates and Regional
2128 Comparisons of the Burden of Foodborne Disease in 2010. *PLoS Med* **12**:e1001923.
2129 Heal WP, Wright MH, Thinon E, Tate EW. 2011. Multifunctional protein labeling via enzymatic
2130 N-terminal tagging and elaboration by click chemistry. *Nat Protoc* **7**:105–117.
2131 Heaslip AT, Nishi M, Stein B, Hu K. 2011. The motility of a human parasite, Toxoplasma gondii,
2132 is regulated by a novel lysine methyltransferase. *PLoS Pathog* **7**:e1002201.
2133 Herneisen AL, Li Z-H, Chan AW, Moreno SNJ, Lourido S. 2022. Temporal and thermal profiling
2134 of the Toxoplasma proteome implicates parasite Protein Phosphatase 1 in the regulation
2135 of Ca2+-responsive pathways. *Elife* **11**. doi:10.7554/eLife.80336
2136 Hopp CS, Bowyer PW, Baker DA. 2012. The role of cGMP signalling in regulating life cycle
2137 progression of Plasmodium. *Microbes Infect* **14**:831–837.
2138 Hunt A, Russell MRG, Wagener J, Kent R, Carmeille R, Peddie CJ, Collinson L, Heaslip A,
2139 Ward GE, Treeck M. 2019. Differential requirements for cyclase-associated protein (CAP)
2140 in actin-dependent processes of Toxoplasma gondii. *Elife* **8**. doi:10.7554/eLife.50598
2141 Huynh M-H, Carruthers VB. 2009. Tagging of endogenous genes in a Toxoplasma gondii strain
2142 lacking Ku80. *Eukaryot Cell* **8**:530–539.
2143 Iacovache I, Paumard P, Scheib H, Lesieur C, Sakai N, Matile S, Parker MW, van der Goot FG.
2144 2006. A rivet model for channel formation by aerolysin-like pore-forming toxins. *EMBO J*
2145 **25**:457–466.
2146 Ingram JR, Knockenhauer KE, Markus BM, Mandelbaum J, Ramek A, Shan Y, Shaw DE,
2147 Schwartz TU, Ploegh HL, Lourido S. 2015. Allosteric activation of apicomplexan calcium-
2148 dependent protein kinases. *Proc Natl Acad Sci U S A* **112**:E4975–84.

2149 Invergo BM, Brochet M, Yu L, Choudhary J, Beltrao P, Billker O. 2017. Sub-minute
2150 Phosphoregulation of Cell Cycle Systems during Plasmodium Gamete Formation. *Cell Rep*
2151 **21**:2017–2029.
2152 Johnson SM, Murphy RC, Geiger JA, DeRocher AE, Zhang Z, Ojo KK, Larson ET, Perera BGK,
2153 Dale EJ, He P, Reid MC, Fox AMW, Mueller NR, Merritt EA, Fan E, Parsons M, Van Voorhis
2154 WC, Maly DJ. 2012. Development of Toxoplasma gondii calcium-dependent protein kinase
2155 1 (TgCDPK1) inhibitors with potent anti-toxoplasma activity. *J Med Chem* **55**:2416–2426.
2156 Kafsack BFC, Pena JDO, Coppens I, Ravindran S, Boothroyd JC, Carruthers VB. 2009. Rapid
2157 membrane disruption by a perforin-like protein facilitates parasite exit from host cells.
2158 *Science* **323**:530–533.
2159 Käll L, Canterbury JD, Weston J, Noble WS, MacCoss MJ. 2007. Semi-supervised learning for
2160 peptide identification from shotgun proteomics datasets. *Nat Methods* **4**:923–925.
2161 Käll L, Storey JD, MacCoss MJ, Noble WS. 2008a. Assigning significance to peptides identified
2162 by tandem mass spectrometry using decoy databases. *J Proteome Res* **7**:29–34.
2163 Käll L, Storey JD, Noble WS. 2008b. Non-parametric estimation of posterior error probabilities
2164 associated with peptides identified by tandem mass spectrometry. *Bioinformatics* **24**:i42–
2165 8.
2166 Katris NJ, van Dooren GG, McMillan PJ, Hanssen E, Tilley L, Waller RF. 2014. The apical
2167 complex provides a regulated gateway for secretion of invasion factors in Toxoplasma.
2168 *PLoS Pathog* **10**:e1004074.
2169 Kessler H, Herm-Götz A, Hegge S, Rauch M, Soldati-Favre D, Frischknecht F, Meissner M.
2170 2008. Microneme protein 8--a new essential invasion factor in Toxoplasma gondii. *J Cell*
2171 *Sci* **121**:947–956.
2172 Krämer H, Phistry M. 1996. Mutations in the Drosophila hook gene inhibit endocytosis of the
2173 boss transmembrane ligand into multivesicular bodies. *J Cell Biol* **133**:1205–1215.
2174 Kremer K, Kamin D, Rittweger E, Wilkes J, Flammer H, Mahler S, Heng J, Tonkin CJ, Langsley
2175 G, Hell SW, Carruthers VB, Ferguson DJP, Meissner M. 2013. An overexpression screen of
2176 Toxoplasma gondii Rab-GTPases reveals distinct transport routes to the micronemes.
2177 *PLoS Pathog* **9**:e1003213.
2178 Kumar S, Kumar M, Ekka R, Dvorin JD, Paul AS, Madugundu AK, Gilberger T, Gowda H,
2179 Duraisingh MT, Keshava Prasad TS, Sharma P. 2017. PfCDPK1 mediated signaling in
2180 erythrocytic stages of Plasmodium falciparum. *Nat Commun* **8**:63.
2181 Lamarque M, Besteiro S, Papoin J, Roques M, Vulliez-Le Normand B, Morlon-Guyot J,
2182 Dubremetz J-F, Fauquenoy S, Tomavo S, Faber BW, Kocken CH, Thomas AW, Boulanger
2183 MJ, Bentley GA, Lebrun M. 2011. The RON2-AMA1 interaction is a critical step in moving
2184 junction-dependent invasion by apicomplexan parasites. *PLoS Pathog* **7**:e1001276.
2185 Lamarque MH, Roques M, Kong-Hap M, Tonkin ML, Rugarabamu G, Marq J-B, Penarete-
2186 Vargas DM, Boulanger MJ, Soldati-Favre D, Lebrun M. 2014. Plasticity and redundancy
2187 among AMA-RON pairs ensure host cell entry of Toxoplasma parasites. *Nat Commun*
2188 **5**:4098.
2189 Lasonder E, Green JL, Camarda G, Talabani H, Holder AA, Langsley G, Alano P. 2012. The
2190 Plasmodium falciparum schizont phosphoproteome reveals extensive phosphatidylinositol
2191 and cAMP-protein kinase A signaling. *J Proteome Res* **11**:5323–5337.
2192 Lee I-G, Olenick MA, Boczkowska M, Franzini-Armstrong C, Holzbaur ELF, Dominguez R.
2193 2018. A conserved interaction of the dynein light intermediate chain with dynein-dynactin
2194 effectors necessary for processivity. *Nat Commun* **9**:986.
2195 Lentini G, Dubois DJ, Maco B, Soldati-Favre D, Frénal K. 2019. The roles of Centrin 2 and
2196 Dynein Light Chain 8a in apical secretory organelles discharge of Toxoplasma gondii.

Traffic **20**:583–600.
Leung JM, He Y, Zhang F, Hwang Y-C, Nagayasu E, Liu J, Murray JM, Hu K. 2017. Stability and function of a putative microtubule-organizing center in the human parasite Toxoplasma gondii. *Mol Biol Cell* **28**:1361–1378.
Leung JM, Liu J, Wetzel LA, Hu K. 2019. Centrin2 from the human parasite Toxoplasma gondii is required for its invasion and intracellular replication. *J Cell Sci* **132**. doi:10.1242/jcs.228791
Li J, Van Vranken JG, Pontano Vaites L, Schweppe DK, Huttlin EL, Etienne C, Nandhikonda P, Viner R, Robitaille AM, Thompson AH, Kuhn K, Pike I, Bomgarden RD, Rogers JC, Gygi SP, Paulo JA. 2020. TMTpro reagents: a set of isobaric labeling mass tags enables simultaneous proteome-wide measurements across 16 samples. *Nat Methods* **17**:399–404.
Long S, Anthony B, Drewry LL, David Sibley L. 2017. A conserved ankyrin repeat-containing protein regulates conoid stability, motility and cell invasion in Toxoplasma gondii. *Nature Communications*. doi:10.1038/s41467-017-02341-2
Lord SJ, Velle KB, Mullins RD, Fritz-Laylin LK. 2020. SuperPlots: Communicating reproducibility and variability in cell biology. *J Cell Biol* **219**. doi:10.1083/jcb.202001064
Lourido S, Jeschke GR, Turk BE, David Sibley L. 2013a. Exploiting the Unique ATP-Binding Pocket of *Toxoplasma* Calcium-Dependent Protein Kinase 1 To Identify Its Substrates. *ACS Chemical Biology*. doi:10.1021/cb400115y
Lourido S, Moreno SNJ. 2015. The calcium signaling toolkit of the Apicomplexan parasites Toxoplasma gondii and Plasmodium spp. *Cell Calcium* **57**:186–193.
Lourido S, Shuman J, Zhang C, Shokat KM, Hui R, Sibley LD. 2010. Calcium-dependent protein kinase 1 is an essential regulator of exocytosis in Toxoplasma. *Nature* **465**:359–362.
Lourido S, Tang K, Sibley LD. 2012. Distinct signalling pathways control Toxoplasma egress and host-cell invasion. *EMBO J* **31**:4524–4534.
Lourido S, Zhang C, Lopez MS, Tang K, Barks J, Wang Q, Wildman SA, Shokat KM, Sibley LD. 2013b. Optimizing small molecule inhibitors of calcium-dependent protein kinase 1 to prevent infection by Toxoplasma gondii. *J Med Chem* **56**:3068–3077.
Luo S, Ruiz FA, Moreno SNJ. 2005. The acidocalcisome Ca2+-ATPase (TgA1) of Toxoplasma gondii is required for polyphosphate storage, intracellular calcium homeostasis and virulence. *Mol Microbiol* **55**:1034–1045.
Mageswaran SK, Guérin A, Theveny LM, Chen WD, Martinez M, Lebrun M, Striepen B, Chang Y-W. 2021. In situ ultrastructures of two evolutionarily distant apicomplexan rhoptry secretion systems. *Nat Commun* **12**:4983.
Markus BM, Bell GW, Lorenzi HA, Lourido S. 2019. Optimizing Systems for Cas9 Expression in Toxoplasma gondii. *mSphere* **4**. doi:10.1128/mSphere.00386-19
Márquez-Nogueras KM, Hortua Triana MA, Chasen NM, Kuo IY, Moreno SN. 2021. Calcium signaling through a transient receptor channel is important for Toxoplasma gondii growth. *Elife* **10**. doi:10.7554/eLife.63417
Martin DDO, Beauchamp E, Berthiaume LG. 2011. Post-translational myristoylation: Fat matters in cellular life and death. *Biochimie* **93**:18–31.
McCoy JM, Stewart RJ, Uboldi AD, Li D, Schröder J, Scott NE, Papenfuss AT, Lehane AM, Foster LJ, Tonkin CJ. 2017. A forward genetic screen identifies a negative regulator of rapid Ca2+-dependent cell egress (MS1) in the intracellular parasite Toxoplasma gondii. *J Biol Chem* **292**:7662–7674.
McCoy JM, Whitehead L, van Dooren GG, Tonkin CJ. 2012. TgCDPK3 regulates calcium-

dependent egress of Toxoplasma gondii from host cells. *PLoS Pathog* **8**:e1003066.
Mueller C, Klages N, Jacot D, Santos JM, Cabrera A, Gilberger TW, Dubremetz J-F, Soldati-Favre D. 2013. The Toxoplasma protein ARO mediates the apical positioning of rhoptry organelles, a prerequisite for host cell invasion. *Cell Host Microbe* **13**:289–301.
Mueller C, Samoo A, Hammoudi P-M, Klages N, Kallio JP, Kursula I, Soldati-Favre D. 2016. Structural and functional dissection of Toxoplasma gondii armadillo repeats only protein. *J Cell Sci* **129**:1031–1045.
Nofal SD, Dominicus C, Broncel M, Katris NJ, Flynn HR, Arrizabalaga G, Botté CY, Invergo BM, Treeck M. 2022. A positive feedback loop mediates crosstalk between calcium, cyclic nucleotide and lipid signalling in calcium-induced Toxoplasma gondii egress. *PLoS Pathog* **18**:e1010901.
Ojo KK, Larson ET, Keyloun KR, Castaneda LJ, Derocher AE, Inampudi KK, Kim JE, Arakaki TL, Murphy RC, Zhang L, Napuli AJ, Maly DJ, Verlinde CLMJ, Buckner FS, Parsons M, Hol WGJ, Merritt EA, Van Voorhis WC. 2010. Toxoplasma gondii calcium-dependent protein kinase 1 is a target for selective kinase inhibitors. *Nat Struct Mol Biol* **17**:602–607.
Ong Y-C, Reese ML, Boothroyd JC. 2010. Toxoplasma Rhoptry Protein 16 (ROP16) Subverts Host Function by Direct Tyrosine Phosphorylation of STAT6*. *J Biol Chem* **285**:28731–28740.
Pang ZP, Südhof TC. 2010. Cell biology of Ca2+-triggered exocytosis. *Curr Opin Cell Biol* **22**:496–505.
Pease BN, Huttlin EL, Jedrychowski MP, Dorin-Semblat D, Sebastiani D, Segarra DT, Roberts BF, Chakrabarti R, Doerig C, Gygi SP, Chakrabarti D. 2018. Characterization of Plasmodium falciparum Atypical Kinase PfPK7- Dependent Phosphoproteome. *J Proteome Res* **17**:2112–2123.
Pease BN, Huttlin EL, Jedrychowski MP, Talevich E, Harmon J, Dillman T, Kannan N, Doerig C, Chakrabarti R, Gygi SP, Chakrabarti D. 2013. Global Analysis of Protein Expression and Phosphorylation of Three Stages of *Plasmodium falciparum* Intraerythrocytic Development. *Journal of Proteome Research*. doi:10.1021/pr400394g
Pomel S, Luk FCY, Beckers CJM. 2008. Host cell egress and invasion induce marked relocations of glycolytic enzymes in Toxoplasma gondii tachyzoites. *PLoS Pathog* **4**:e1000188.
Redwine WB, DeSantis ME, Hollyer I, Htet ZM, Tran PT, Swanson SK, Florens L, Washburn MP, Reck-Peterson SL. 2017. The human cytoplasmic dynein interactome reveals novel activators of motility. *Elife* **6**. doi:10.7554/eLife.28257
Reese ML, Zeiner GM, Saeij JPJ, Boothroyd JC, Boyle JP. 2011. Polymorphic family of injected pseudokinases is paramount in Toxoplasma virulence. *Proc Natl Acad Sci U S A* **108**:9625–9630.
Rothenberg DA, Gordon EA, White FM, Lourido S. 2016. Identification of Direct Kinase Substrates Using Analogue-Sensitive Alleles. *Methods Mol Biol* **1355**:71–84.
Sebastian S, Brochet M, Collins MO, Schwach F, Jones ML, Goulding D, Rayner JC, Choudhary JS, Billker O. 2012. A Plasmodium calcium-dependent protein kinase controls zygote development and transmission by translationally activating repressed mRNAs. *Cell Host Microbe* **12**:9–19.
Segev-Zarko L-A, Dahlberg PD, Sun SY, Pelt DM, Kim CY, Egan ES, Sethian JA, Chiu W, Boothroyd JC. 2022. Cryo-electron tomography with mixed-scale dense neural networks reveals key steps in deployment of Toxoplasma invasion machinery. *PNAS Nexus* **1**:gac183.
Shen B, Brown KM, Lee TD, David Sibley L. 2014. Efficient Gene Disruption in Diverse Strains of Toxoplasma gondii Using CRISPR/CAS9. *mBio*. doi:10.1128/mbio.01114-14

2294 Shortt E, Hackett CG, Stadler RV, Ward GE, Lourido S. 2022. CDPK2A and CDPK1 form a
2295 signaling module upstream of Toxoplasma motility. *bioRxiv*.
2296 doi:10.1101/2022.07.19.500742
2297 Sidik SM, Hortua Triana MA, Paul AS, El Bakkouri M, Hackett CG, Tran F, Westwood NJ, Hui
2298 R, Zuercher WJ, Duraisingh MT, Moreno SNJ, Lourido S. 2016a. Using a Genetically
2299 Encoded Sensor to Identify Inhibitors of Toxoplasma gondii Ca2+ Signaling. *J Biol Chem*
2300 **291**:9566–9580.
2301 Sidik SM, Huet D, Ganesan SM, Huynh M-H, Wang T, Nasamu AS, Thiru P, Saeij JPJ,
2302 Carruthers VB, Niles JC, Lourido S. 2016b. A Genome-wide CRISPR Screen in
2303 Toxoplasma Identifies Essential Apicomplexan Genes. *Cell* **166**:1423–1435.e12.
2304 Sidik SM, Valleau D, Acevedo-Sánchez Y, Godoy LC, Pasaje CFA, Huynh M-H, Carruthers VB,
2305 Niles JC, Lourido S. n.d. A conserved complex of microneme proteins mediates rhoptry
2306 discharge in*Toxoplasma*. doi:10.1101/2022.11.28.518173
2307 Simm D, Hatje K, Kollmar M. 2015. Waggawagga: comparative visualization of coiled-coil
2308 predictions and detection of stable single α-helices (SAH domains). *Bioinformatics* **31**:767–
2309 769.
2310 Singer M, Simon K, Forné I, Meissner M. 2022. A central protein complex essential for Invasion
2311 in Toxoplasma gondii. *bioRxiv*. doi:10.1101/2022.02.24.481622
2312 Smith TA, Lopez-Perez GS, Herneisen AL, Shortt E, Lourido S. 2022. Screening the
2313 Toxoplasma kinome with high-throughput tagging identifies a regulator of invasion and
2314 egress. *Nat Microbiol* **7**:868–881.
2315 Söding J, Biegert A, Lupas AN. 2005. The HHpred interactive server for protein homology
2316 detection and structure prediction. *Nucleic Acids Res* **33**:W244–8.
2317 Solyakov L, Halbert J, Alam MM, Semblat J-P, Dorin-Semblat D, Reininger L, Bottrill AR, Mistry
2318 S, Abdi A, Fennell C, Holland Z, Demarta C, Bouza Y, Sicard A, Nivez M-P, Eschenlauer S,
2319 Lama T, Thomas DC, Sharma P, Agarwal S, Kern S, Pradel G, Graciotti M, Tobin AB,
2320 Doerig C. 2011. Global kinomic and phospho-proteomic analyses of the human malaria
2321 parasite Plasmodium falciparum. *Nature Communications*. doi:10.1038/ncomms1558
2322 Sparvoli D, Delabre J, Penarete-Vargas DM, Kumar Mageswaran S, Tsypin LM, Heckendorn J,
2323 Theveny L, Maynadier M, Mendonça Cova M, Berry-Sterkers L, Guérin A, Dubremetz J-F,
2324 Urbach S, Striepen B, Turkewitz AP, Chang Y-W, Lebrun M. 2022. An apical membrane
2325 complex for triggering rhoptry exocytosis and invasion in Toxoplasma. *EMBO J*
2326 **41**:e111158.
2327 Stasic AJ, Chasen NM, Dykes EJ, Vella SA, Asady B, Starai VJ, Moreno SNJ. 2019. The
2328 Toxoplasma Vacuolar H+-ATPase Regulates Intracellular pH and Impacts the Maturation
2329 of Essential Secretory Proteins. *Cell Rep* **27**:2132–2146.e7.
2330 Sun SY, Segev-Zarko L-A, Chen M, Pintilie GD, Schmid MF, Ludtke SJ, Boothroyd JC, Chiu W.
2331 2022. Cryo-ET of *Toxoplasma* parasites gives subnanometer insight into tubulin-based
2332 structures. *Proc Natl Acad Sci U S A* **119**. doi:10.1073/pnas.2111661119
2333 Tang Q, Andenmatten N, Hortua Triana MA, Deng B, Meissner M, Moreno SNJ, Ballif BA, Ward
2334 GE. 2014. Calcium-dependent phosphorylation alters class XIVa myosin function in the
2335 protozoan parasite Toxoplasma gondii. *MBoC* **25**:2579–2591.
2336 Taus T, Köcher T, Pichler P, Paschke C, Schmidt A, Henrich C, Mechtler K. 2011. Universal
2337 and confident phosphorylation site localization using phosphoRS. *J Proteome Res*
2338 **10**:5354–5362.
2339 Taylor HM, McRobert L, Grainger M, Sicard A, Dluzewski AR, Hopp CS, Holder AA, Baker DA.
2340 2010. The malaria parasite cyclic GMP-dependent protein kinase plays a central role in
2341 blood-stage schizogony. *Eukaryot Cell* **9**:37–45.
2342 Thrun MC, Ultsch A. 2021. Using Projection-Based Clustering to Find Distance- and Density-

Based Clusters in High-Dimensional Data. *J Classification* **38**:280–312.
Tosetti N, Dos Santos Pacheco N, Soldati-Favre D, Jacot D. 2019. Three F-actin assembly centers regulate organelle inheritance, cell-cell communication and motility in Toxoplasma gondii. *Elife* **8**. doi:10.7554/eLife.42669
Treeck M, Sanders JL, Elias JE, Boothroyd JC. 2011. The phosphoproteomes of Plasmodium falciparum and Toxoplasma gondii reveal unusual adaptations within and beyond the parasites' boundaries. *Cell Host Microbe* **10**:410–419.
Treeck M, Sanders JL, Gaji RY, LaFavers KA, Child MA, Arrizabalaga G, Elias JE, Boothroyd JC. 2014. The calcium-dependent protein kinase 3 of toxoplasma influences basal calcium levels and functions beyond egress as revealed by quantitative phosphoproteome analysis. *PLoS Pathog* **10**:e1004197.
Tsai C-F, Hsu C-C, Hung J-N, Wang Y-T, Choong W-K, Zeng M-Y, Lin P-Y, Hong R-W, Sung T-Y, Chen Y-J. 2014. Sequential phosphoproteomic enrichment through complementary metal-directed immobilized metal ion affinity chromatography. *Anal Chem* **86**:685–693.
Tyler JS, Boothroyd JC. 2011. The C-terminus of Toxoplasma RON2 provides the crucial link between AMA1 and the host-associated invasion complex. *PLoS Pathog* **7**:e1001282.
Van Vranken, Pontano Vaites, Schweppe. n.d. TMTpro reagents: a set of isobaric labeling mass tags enables simultaneous proteome-wide measurements across 16 samples. *Nature*.
Wang X, Fu Y, Beatty WL, Ma M, Brown A, Sibley LD, Zhang R. 2021. Cryo-EM structure of cortical microtubules from human parasite Toxoplasma gondii identifies their microtubule inner proteins. *Nat Commun* **12**:3065.
Wernimont AK, Artz JD, Finerty P Jr, Lin Y-H, Amani M, Allali-Hassani A, Senisterra G, Vedadi M, Tempel W, Mackenzie F, Chau I, Lourido S, Sibley LD, Hui R. 2010. Structures of apicomplexan calcium-dependent protein kinases reveal mechanism of activation by calcium. *Nat Struct Mol Biol* **17**:596–601.
Wichroski MJ, Melton JA, Donahue CG, Tweten RK, Ward GE. 2002. Clostridium septicum alpha-toxin is active against the parasitic protozoan Toxoplasma gondii and targets members of the SAG family of glycosylphosphatidylinositol-anchored surface proteins. *Infect Immun* **70**:4353–4361.
Wilson SK, Heckendorn J, Martorelli Di Genova B, Koch LL, Rooney PJ, Morrissette N, Lebrun M, Knoll LJ. 2020. A Toxoplasma gondii patatin-like phospholipase contributes to host cell invasion. *PLoS Pathog* **16**:e1008650.
Winzer P, Müller J, Aguado-Martínez A, Rahman M, Balmer V, Manser V, Ortega-Mora LM, Ojo KK, Fan E, Maly DJ, Van Voorhis WC, Hemphill A. 2015. In Vitro and In Vivo Effects of the Bumped Kinase Inhibitor 1294 in the Related Cyst-Forming Apicomplexans Toxoplasma gondii and Neospora caninum. *Antimicrob Agents Chemother* **59**:6361–6374.
Wright MH, Clough B, Rackham MD, Rangachari K, Brannigan JA, Grainger M, Moss DK, Bottrill AR, Heal WP, Broncel M, Serwa RA, Brady D, Mann DJ, Leatherbarrow RJ, Tewari R, Wilkinson AJ, Holder AA, Tate EW. 2014. Validation of N-myristoyltransferase as an antimalarial drug target using an integrated chemical biology approach. *Nature Chemistry*. doi:10.1038/nchem.1830
Xu L, Sowa ME, Chen J, Li X, Gygi SP, Harper JW. 2008. An FTS/Hook/p107FHIP Complex Interacts with and Promotes Endosomal Clustering by the Homotypic Vacuolar Protein Sorting Complex. *MBoC* **19**:5059–5071.
Yang L, Uboldi AD, Seizova S, Wilde M-L, Coffey MJ, Katris NJ, Yamaryo-Botté Y, Kocan M, Bathgate RAD, Stewart RJ, McConville MJ, Thompson PE, Botté CY, Tonkin CJ. 2019. An apically located hybrid guanylate cyclase–ATPase is critical for the initiation of Ca2+ signaling and motility in Toxoplasma gondii. *J Biol Chem* **294**:8959–8972.

2392 Yao X, Wang X, Xiang X. 2014. FHIP and FTS proteins are critical for dynein-mediated
2393 transport of early endosomes in Aspergillus. *Mol Biol Cell* **25**:2181–2189.
2394 Yuasa K, Mi-Ichi F, Kobayashi T, Yamanouchi M, Kotera J, Kita K, Omori K. 2005. PfPDE1, a
2395 novel cGMP-specific phosphodiesterase from the human malaria parasite Plasmodium
2396 falciparum. *Biochem J* **392**:221–229.
2397 Zecha J, Satpathy S, Kanashova T, Avanessian SC, Kane MH, Clauser KR, Mertins P, Carr SA,
2398 Kuster B. 2019. TMT Labeling for the Masses: A Robust and Cost-efficient, In-solution
2399 Labeling Approach. *Mol Cell Proteomics* **18**:1468–1478.
2400 Zhang J, Qiu R, Arst HN, Peñalva MA, Xiang X. 2014. HookA is a novel dynein–early endosome
2401 linker critical for cargo movement in vivo. *J Cell Biol* **204**:1009–1026.

2402